The Dissertation Committee for Kemal Peter Sobotkiewich
certifies that this is the approved version of the following dissertation:

Probing Magnons in Metallic Magnetic Bilayers for Spintronic Applications

Committee:

Xiaoqin Li, Supervisor

Maxim Tsoi

John Markert

Gregory Fiete

Jean Anne Incorvia

Probing Magnons in Metallic Magnetic Bilayers for Spintronic Applications

by

Kemal Peter Sobotkiewich

Dissertation

Presented to the Faculty of the Graduate School of

The University of Texas at Austin

in Partial Fulfillment

of the Requirements

for the Degree of

Doctor of Philosophy

The University of Texas at Austin

August 2019

Acknowledgments

This dissertation would not have been possible without the help and support of multiple people.

The first and foremost is my wonderful wife who has continued to love and support me through 5 incredibly difficult years of my life. Not only that but together we have built a family and at time of writing have one beautiful baby boy who brings joy to my days.

Of course none of this would have been possible without my advisor professor Elaine Li. She has been able to guide me and shape me into a better scientist and a more thoughtful, proactive and careful worker. The skills I have developed will continue to serve me throughout all future endeavors.

I would like to acknowledge the many talented people I have collaborated with through the years. In particular: prof. Krivorotov and his students Andrew Smith and Chris Safranski who provided me the samples for all my Nanowire STO projects, prof. Yang and his postdoc dr. Adam Ahmed as well as his student Aidan Lee who provided me the CoFe samples for my DMI project, and finally dr. Lijun Zhu with who invited me to work on the PdPt project which was able to combine my knowledge of STT and DMI.

I would not have successfully completed my p.h.d if not for my mentors within the Li group. In particular dr. Kyongmo An who first taught me the BLS system and welcomed me into the magnetism group and dr.Kevin Olsson with whom I started

working later in my career and without whose help I would have likely abandoned my work before completion.

I would like to thank David Lujan and Nate Nunley who are two very promising students who will both go one to do great things in the field of magnetism. I leave my unfinished work with David who has already mastered the experimental setup and will no doubt be able to complete my remaining projects.

I also need to thank all of the friends I have made in the physics department during my time in Austin. Graduate school is a grind and without being able to talk to people going through the same thing I would not have retained my sanity. In addition I need to thank Matt Ervin , the graduate coordinator not only for his wonderful company, but for his invaluable aid in navigating paperwork and bureaucracy.

Finally, I want to thank all of my committee members for giving me the opportunity to present my work to them and for the insightful questions they asked.

Probing Magnons in Metallic Magnetic Bilayers for Spintronic Applications

Publication No. _____

Kemal Peter Sobotkiewich, Ph.D.
The University of Texas at Austin, 2019

Supervisor: Xiaoqin Li

The field of spintronics, which concerns itself with the manipulation of the spin degree of freedom for information storage and processing purposes, has made enormous progress in the last decades going from a theory to commercial products. The field is continuously driven by the demand of storing information with high density and reduced energy consumption. Progress often occurs by exploring material combinations and new device geometries. In recent years, magnetic bilayers consisting of a ferromagnet and a heavy metal thin films have emerged as a promising material platform for new generations of spintronic devices. Many interesting fundamental questions remain to be addressed in these seemingly simple

bilayers. This thesis focuses on studying different bilayers in order to realize new spin torque oscillators and to search for optimal materials for information storage in novel spin textures such as skyrmions. The materials and devices described below are characterized using Brillouin Light Scattering (BLS).

Spin torque oscillators show enormous promise as components in spintronic circuits due to their high energy efficiency and tunable frequencies. Additionally their nonlinear properties make them promising candidates for neuromorphic computing applications. We study nanowire spin torque oscillators using both insulating(YIG) and metallic(Ni20Fe80) magnetic layers on top of a Heavy Metal layer (Pt). For the insulating case, we show the feasibility of making devices with the insulating layer as well as the impact of the Spin Seebeck effect in increasing energy efficiency. For the metallic wires, we study new phenomena that emerge from extending the dimensionality of the STOs to one dimension. In particular, we show the existence of two distinct modes whose different properties might be exploitable for more exotic microwave sources. We study these wires with a micrometer focus BLS setup to ensure the spatial resolution needed to gain information from the nanowires.

We also explore the possibility of chiral spintronics by studying bilayers showing significant interfacial Dzyaloshinskii-Moriya Interaction (DMI) while also possessing other characteristics which may be useful for spintronics. First we study Pd25Pt75 which combines high spin Hall efficiency as well as a strong tunable DMI when combined with a Co based magnetic layer. Second we study epitaxially grown Co25Fe75 which combines a strong DMI with a record low magnetic damping for a metallic film. The results of these sections provide guidance for future device engineering by suggesting promising materials. We study these systems with a BLS setup which uses a large spot size to maintain momentum resolution. We measure the asymmetric shift between the Stokes and anti-Stokes peak. This shift changes

linearly with respect to wavevectors, allowing one to extract interfacial DMI.

Contents

List of Tables

List of Figures

Chapter 1

Introduction

The field of spintronics began with the discovery of the Giant Magnetoresistance effect and it counterpart the Spin Transfer Torque effect[1, 2, 3, 4]. In the years since, GMR has become standard in read heads of magnetic memories and all spin devices have gone into production. However, these spintronic devices have not yet become more efficient or more powerful than their traditional counterparts. What is required is new materials and new device designs that can allow spintronics to take the next step.

A device design which has already seen much work is the Spin Torque Oscillator which can provide a tunable, energy efficient frequency generator for spintronic circuits [5, 6, 7]. By exploring new geometries we can not only improve the performance of these oscillators but exploit more complex properties of these devices for more exotic applications such as neuromorphic computing[8]. By exploring new materials to form the basis of these oscillators we can not only improve efficiency by finding optimized alloyed compositions, but enable new effects to improve the performance such as the Spin Seebeck effect [9, 10] when utilizing an insulating ferromagnet.

Another new direction is the advent of chiral spintronics arising from the

Dzyaloshinskii-Moriya effect. DMI favors the formation of chiral structures in materials which can have advantageous properties. One such structure is the chiral domain wall which can potentially be driven at lower current densities or faster speeds.[11, 12, 13, 14, 15]. Another is the magnetic skyrmion.

A magnetic Skyrmion is a spiral spin structure that can form in magnetic materials. The structure can be described as follows: The spins rotate progressively with fixed chirality from one orientation at the edge to a flipped orientation at the center and then back to the original orientation at the other edge[16].

Skyrmions are topologically nontrivial and are defined by their topological number S (also known as their Skyrmion number) given in the two dimensional limit by:

$$S = \frac{1}{4\pi} \int m \cdot (\partial_x m \times \partial_y m) dx dy \tag{1.1}$$

This non trivial topology means that Skyrmions cannot be continuously deformed into a different spin configuration with a different topological number. For typical Skyrmions $S = \pm 1$ whereas continuous magnetization has $S = 0$. As such there is a topological barrier which stabilizes the Skyrmion allowing them to be long lived.

Skyrmions consist of a chiral rotation of spins and so for them to form there must be something present which allows for this rotation. The rotation comes from the Dzyaloshinskii-Moriya interaction and crystals without DMI cannot form Skyrmions. Skyrmions have so far been observed in crystals lacking inversion symmetry and in magnetic bilayers.

Another key feature of Skyrmions is their finite extent which enables them to behave like particles. As we will see in a later section, Skyrmions can be moved by the application of current.

In summary, Skyrmions are compact, controllable magnetic structures which are topologically stabilized and are thus potentially very useful for memory appli-

cations.

Proper characterization of magnetic materials is crucial to developing working devices as Skyrmions rely on a delicate balance of magnetic parameters to determine their stability and size [17]

This thesis will focus on the characterization of new device geometries and new materials in familiar device geometries with an eye towards finding suitable candidates for future device applications. In particular, we restrict ourselves to systems exploiting the physics that occur at the interface between a Heavy Metal and a Ferromagnet.

In **Chapter 2** the necessary knowledge of magnetism and magnetic dynamics is presented. We start by describing the different forms of magnetism that arise in nature before describing the dynamics of magnetism. Then we present a more detailed picture of magnetism in materials by describing the magnetic anisotropy. Magnetic effects that will be studied in more detail during the rest of the thesis. In focus will be Spin Transfer Torque and the Dzyaloshinskii-Moriya interaction as well as relevant applications of those effects.

In **Chapter 3** the experimental tools are presented. We start by describing the working principles of Brillouin Light Scattering in detail and describing how they may be used to characterize the strength of DMI in materials. We describe our experimental setup as well as the details of magnon scattering from materials. Next we present alternate methods of characterizing DMI and their advantages and flaws relative to BLS. Finally we present the methods of characterizing the saturation magnetization of materials since it is a frequent, key supporting measurent for our experiments.

In **Chapter 4** Nanowire Spin Torque Oscillators are characterized using BLS. First we present a nanowire based on insulating Yttrium Iron Garnett (YIG). We show that by growing the YIG directly on Pt a high efficiency device can be

made which will be aided by the Spin Seebeck effect. Next the detailed properties of a nanowire based on metallic Permalloy ($Ni_{20}Fe_{80}$) are studied. In particular we discuss the difference between the two types of oscillatory modes that can arise.

In **Chapter 5** we present the Heavy Metal $Pd_{25}Pt_{75}$ which is shown to have advantageous properties for applications. This material combines efficient spin hall effect based spin current generation, low resistivity and large and tunable DMI to be a promising, versatile material for spintronic devices.

In **Chapter 6** we characterize low damping CoFe alloys of varying compositions. The samples studied are epitaxially grown allowing for lower damping and cleaner interfaces which might be possible to simulate. We whow the presence of DMI with an unusual thickness dependence based on the strength of Heisenberg exchange being thickness dependent. We explore several compositions but run into some roadblocks.

Chapter 7 summarizes the work done and lists the published or presented works by the author.

Chapter 2

Magnetism Background

2.1 Types of Magnetism

[18]Materials react to the presence of an externally applied magnetic field in different ways. To describe these different reactions we introduce the magnetic susceptibility χ defined by:

$$M = M_0 + \chi H \tag{2.1}$$

Where M is the net magnetic moment of the material, M_0 is the magnetic moment at zero applied field and H is the strength of the applied magnetic field. In general χ is a matrix quantity describing the effects in all 3 spatial dimensions. However when considering isotropic materials, as we will initially do for simplicity, we can assume that M is either modified parallel or anti-parallel to the applied field direction. These would manifest as a positive or negative value of χ respectively.

If a material does not contain atoms or ions with permanent magnetic moments then the magnetization of the material will be changed to oppose the direction of the applied field. Such materials are called diamagnetic. The cause of this effect is a microscopic application of Lenz's law which states that in the presence of a magnetic field currents will be formed to oppose the direction of the applied field.

In the case of a diamagnetic materials the "currents" are modifications to electronic orbitals. The angular momentum of the conduction electrons will be modified in a way that opposes the field direction. As such χ is negative in diamagnetic materials. All materials have diamagnetic response, but in materials with permanent magnetic moments the effects of diamagnetism are overcome by the effect of those magnetic moments.

Materials with permanent magnetic moments in their atoms or ions that are lacking long range order show paramagnetic response. In the absence of an external field these materials will have no net magnetization in thermal equilibrium. The presence of a field will cause the magnetic moments to align with the field direction in order to reduce energy leading to a net magnetic moment in the material. Since the moments align with the external field paramagnetism is characterized by the presence of a positive value of χ.

Materials where the atomic or ionic magnetic moments do spontaneously align and persist even in the absence of magnetic fields are known as ferromagnets. Neighbouring spins interact with each other via what is known as the exchange interaction. The usual way to describe the effects of the exchange interaction is via the following Hamiltonian:

$$H = -J \sum_{<ij>} \hat{S}_i \cdot \hat{S}_j \tag{2.2}$$

where the sum is over all pairs of nearest neighbours, $\hat{S}_i, j$ is the magnetic moment at the ith or jth atomic site and can be positive or negative depending on the spin orientation and J is the strength of the exchange interaction. If J is positive, then energy is minimized when neighbouring spins are aligned and the dot product is positive and the system is ferromagnetic. If J is negative then the system will favor opposite alignment of neighbouring spins meaning that the system is either Ferrimagnetic or Antiferromagnetic. Both cases will be discussed in a later section.

The origin of the exchange interaction is quantum mechanical and a con-

sequence of the coulomb interaction between neighbouring atomic sites. Energy is reduced if the electrons are further away from each other. Quantum mechanically this corresponds to minimizing and overlap integral between the wavefunctions of the neigbouring electrons. The nature of the allowed states is correlated to the spin state of the electron. In particular for the case of ferromagnetism, Pauli exclusion causes electrons with identical spins to overlap less reducing the energy associated with their coulomb interaction.

While the exchange interaction causes ordered states to be energetically favored thermal fluctuations can disrupt the magnetic ordering. In fact, materials are ferromagnetic only up to a critical temperature known as the Curie temperature. Above this temperature the material becomes paramagnetic with the local spins aligning with an external field and no remnant magnetization at zero field. Above the transition temperature susceptibility follows Curie's law:

$$\chi = \frac{C}{T - T_c} \tag{2.3}$$

Where C is a material specific constant, T is the absolute temperature measured in Kelvin's and T_c is the critical Curie temperature.

Below the Curie temperature where magnetic order is possible without the presence of an external field the behaviour of the magnetization as a function of applied field shows hysteresis. That is the state of the system depends on its history. A typical hysteresis loop can be seen in figure 2.1. The key points on the hysteresis loop are labeled.

a and d represent the saturation magnetization. The magnetization in a material will eventually saturate since at high enough field all of the magnetic moments will be pointing in the same direction and the magnetization will be maximized. The field at which this starts to happen is the saturation field.

b and e are the retentivity which is the amount of magnetization remaining

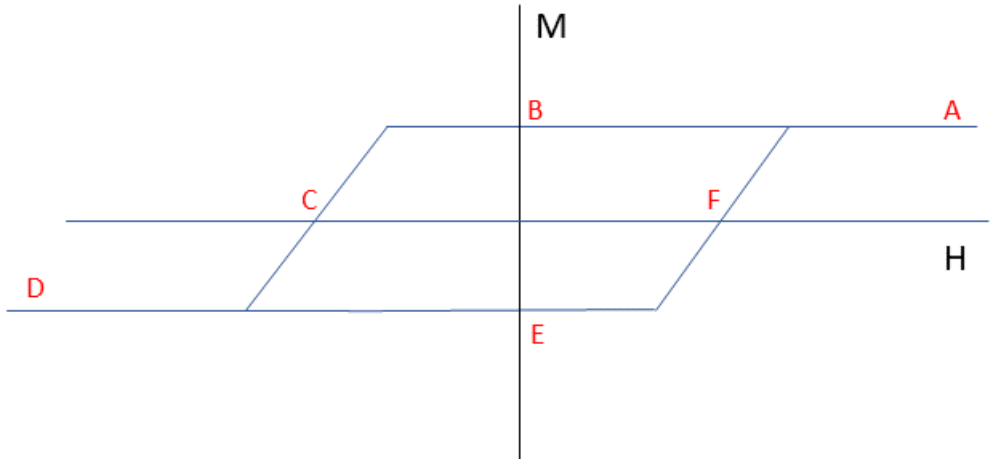

Figure 2.1: Hysteresis loop for a magnetic material. Key points are labeled for each field direction. A,D are the saturation magnetizations, B,E are retentivities and C,F are coercivities

in the material when the field goes to zero. Whether the magnetization is positive or negative depends on whether you approach from a positive or a negative field. This exemplifies hysteresis since the current state of the material depends on a past state.

c and f are the coercivity or the coercive field which corresponds to the field required for the magnetization to return to zero. The strength of this field can characterize whether a magnet is hard or soft.

AntiFerromagnetic materials are materials where long range order through exchange is present, but the exchange interaction is negative causing neighbouring spins to align antiparallel. These materials will have no net magnetic moment in the absence of an external field.

Their dependence on external field is highly anisotropic. If the field is aligned in the direction of the spins then the susceptibility will be next to zero. The spins will not reorient unless the field strength overcomes the exchange field. It can take a magnetic field of several Tesla to flip the spins of an antiferromagnet.

If the field is perpendicular to the spins then the spins can rotate without

needing to overcome the exchange interaction and the material will behave like a paramagnet.

AFM materials are attractive because they are stable to stray magnetic fields and do not create stray fields themselves due to their lack of a net magnetization. However these same features make them difficult to work with. Recent advances however have enabled both control and detection of magnetic order in AFM materials making them a promising material for future spintronic applications.

Much like FM materials AFM materials become paramagnetic above a critical temperature due to thermal fluctuations. In the AFM case the temperature is known as the Nel temperature and the temperature dependence for AFM materials is given by:

$$\chi = \frac{C}{T + T_N} \tag{2.4}$$

where C is a constant as in the previous case and T_N is the Nel temperature.

A ferrimagnet is a material with negative exchange constant much like an AFM but where the neighnouring spins are not equal in magnitude. This causes the system to have a net magnetic moment and still behave very much like a ferromagnet.

AFMs and Ferrimagnets are often treated as having two spin sublattices with opposing spins. Interactions between the two sublattices can determine much of the magnetic behaviour. Yittrium Iron Garnett (YIG) which has chemical composition $Y_3Fe_5O_{12}$ is a very common material for device applications thanks to its low magnetic damping and it is a ferrimagnet.

Ferrimagnets exhibit the same temperature dependence of susceptibility as AFM materials

2.2 Magnetostatics

2.2.1 Magnetic Anisotropy

[19]Real magnetic materials do no behave isotropically. The direction of the applied field will have dramatic effects on the physics present. The origins of the anisotropy come both from the crystal structure of the material and from the shape of the material. Anisotropy will also affect magnetization dynamics and even allows for zero field oscillations.

Demagnetization Field

When a material is in a magnetic field it will respond and there will be magnetic poles created within the material which tend to oppose the applied field. This happens independently of the magnetic moments which can exist at atomic sites. Therefore the magnetization does not respond to the applied field but rather to some internal field H_i given by

$$H_i = H_{ext} + H_d \tag{2.5}$$

where H_{ext} is the external applied field and H_d is known as the demagnetization field. H_d opposes the external field and is given by

$$H_d = -NH_{ext} \tag{2.6}$$

where N is the demagnetization factor. This factor is anisotropic and depends on the shape of the material. It is convenient to consider the demagnetization factors of the three spatial directions individually and normalize them such that:

$$N_x + N_y + N_z = 4\pi \tag{2.7}$$

The demagnetization factors for some common shapes are:

a) a sphere

$$N_x = N_y = N_z = \frac{4\pi}{3} \tag{2.8}$$

b) an infinite plane

$$N_x = N_y = 0, N_z = 4\pi \tag{2.9}$$

c) finite sheet(in plane components)

$$N_h = \frac{2t}{\pi\omega}, n_w = \frac{2t}{\pi h} \tag{2.10}$$

The energy density associated with this shape anisotropy is given by:

$$f = \frac{\mu_0}{2} M_s^2 (N_x - N_y) \tag{2.11}$$

The above arguments depend on the shape of the material only and are independent of crystal structure. These anisotropies are always present but are often overcome by the intrinsic crystalline anisotropy outlined in the following section.

MagnetoCrystalline anisotropy

When the orbitals of the electrons which are carrying the magnetic moment are not symmetric, then there can be an asymmetry in the exchange interaction. Recall that the exchange interaction depends on the overlap integral between neighbouring spins and as such some crystal directions will be more favorable to magnetic ordering than others. Another source of the anisotropy is the spin orbit coupling where the spin and orbital angular moment interact meaning that the net direction of the magnetic moment will depend on the orbital energy which is itself anisotropic.

Many useful materials show uniaxial anisotropy. Such materials are charac-

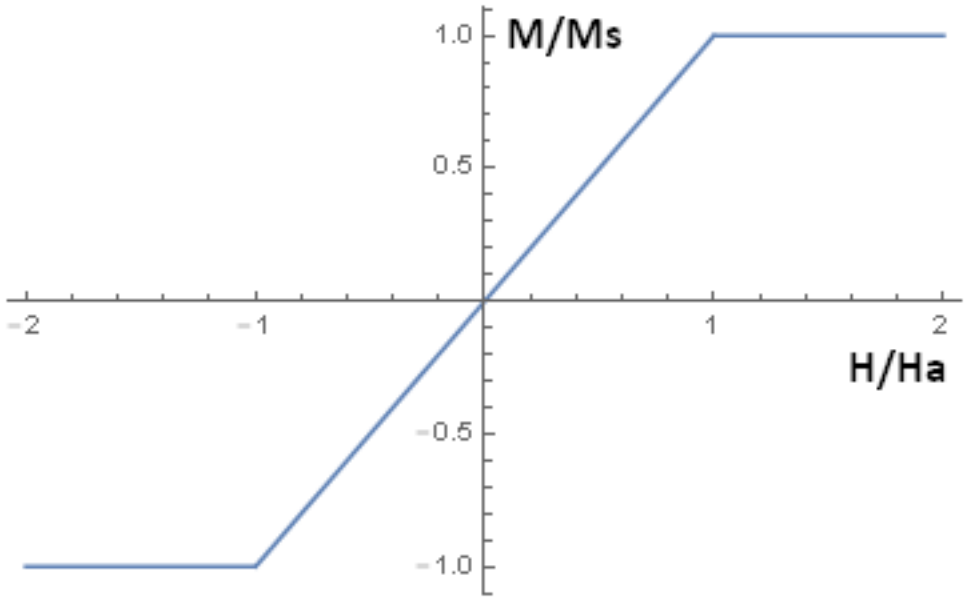

Figure 2.2: Hard axis magnetization loop

terized by a distinctive axis which can be easy or hard meaning the magnetization will preferentially choose or avoid its characteristic axis respectively. Uniaxial materials with a hard axis are sometimes called easy plane. The hysterisis loop is modified in the presence of anisotropy and depends on the direction of the applied field. If the field is applied along an easy axis direction then we recover figure 2.1. Howeve, rif we apply the field along a hard axis then there will be no hysteresis and the pattern will be as in figure 2.2.

The field at which the magnetization saturates along a hard axis is known as the anistropy field (H_a).

We can also describe the energy associated with magnetocrystalline anisotropy. In the uniaxial case symmetry dictates that only the magnitude of the angle between the field direction and the hard or easy axis can matter. We can then write the energy as a sum of even powers of the angle. We also want the energy to be zero when aligned with the characteristic axis and so only keep the sine terms to get:

$$f = K_1 sin^2\theta + K_2 sin^4\theta + ... \tag{2.12}$$

For field directions close to the easy or hard axis the first term is sufficient. Whether the axis is easy or hard is determined by the sine of k_1, positive for easy axis and negative for hard axis.

2.2.2 Saturation Magnetization

Saturation magnetization is a key parameter in most experimental techniques which measure DMI. As such it is important to have reliable methods to measure it. The two most common techniques are Vibrating Sample Magnetometry (VSM) and Superconducting Quantum Interference Device (SQUID) measurements.

VSM

A vibrating sample magnetometer is a versatile instrument making use of magnetic flux to measure magnetization[20].

A schematic for the experimental setup of VSM can be seen in figure 2.3

the sample is placed within an electromagnet which creates a controllable uniform field. The field will induce a magnetization in the sample. The sample is placed on a sample holder which vibrates perpendicular to the direction of the applied field. Since the sample is magnetized it creates a magnetic field. When the sample is vibrated that field is modulated. In particular the strength of the field at the pickup coiled changes with time as the distance between the sample and the coil changes. The change in magnetic flux will induce a voltage in the pick up coils. For a fixed driving frequency the induced voltage will be proportional to the magnetization of the sample and independent of the applied static field.

To perform a VSM experiment a sample is placed into the chamber and the electromagnet is turned on. The sample is made to vibrate sinusoidally inducing

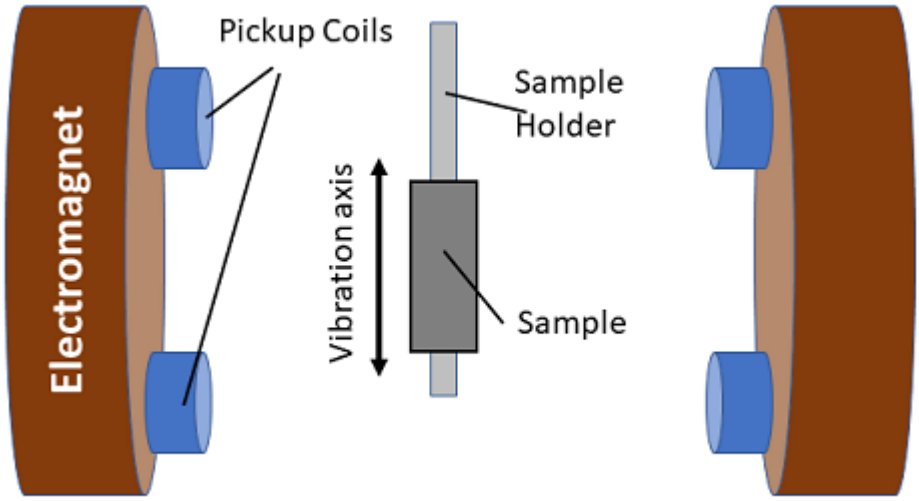

Figure 2.3: Schematic of Vibrating sample magnetometer experiment. The electromagnet magnetizes the sample. The sample holder vibrates the sample creating a change in magnetic flux which creates a voltage in the pickup coils.

voltage into the pick up coils. The vibrations are typically induced by using a piezoelectric material in the sample holder and sending a sinusoidal current. The induced voltage in the pick up coil is amplified through the use of a lock-in amplifier which uses the signal sent to the piezoelectric material as the reference. The magnetic field is then swept back and forth and the voltage is measured at each point. From this a hysteresis loop is generated and saturation magnetization can be found. VSM can be performed within a cryostatic chamber and thus saturation magnetization can be found at low temperatures as well and can even be found as a function of temperature.

SQUID

SQUID[21] uses superconducting loops to measure magnetic flux down to the quantum limit. SQUID devices use Josephson junctions which are two superconductors

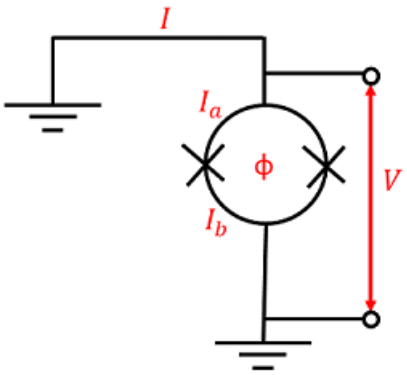

Figure 2.4: Electric diagram of SQUID measurement. X is the symbol for the Josephson junctions.

separated by a thin insulating barrier[22]. Current can flow through the barrier thanks to quantum tunneling. The purpose of the Josephson junction in SQUID is to create distinct superconducting regions which are nevertheless connected.

SQUID creates a loop out of two Josephson junctions as seen in figure 2.4 The operating principle is as follows: when sending a current I to the loop in the absence of a magnetic field it will split evenly between the two branches and recombine, then go to ground. However if there is magnetic flux in the loop screening currents will be generating in each superconductor to cancel out the flux. The current in each branch will become $I_a = I + I_s$ and $I_b = I - Is$ if the current in either branch is above the critical current a voltage will appear across the junction. To ensure this is always the case I is chosen to be higher than the critical current. The SQUID is then said to be operating in the resistive mode.

The current-voltage characteristic of a superconducting loop is hysteretic and so we need to introduce a shunt resistance across the junction to remove the hysterisis. From Lenz's law we know that the screen current must be equal to the applied flux divided by the self inductance of the superconducting ring. The induced voltage from a change in flux can then be estimated as follows:

$$\Delta V = R\Delta I \tag{2.13}$$

and

$$\Delta I = \frac{\Delta\phi}{L} \tag{2.14}$$

and so

$$V = \frac{R}{L}\Delta\phi \tag{2.15}$$

Note that since the Josephson effect is quantum mechanical in nature it will be sensitive to even a single quantum of magnetic flux. As such SQUID is unmatched in its sensitivity to magnetic flux.

Using SQUID to measure saturation magnetization is completely analogous to using VSM. The sample is placed in a static field (no change in flux) and vibrated to create a change in flux. The voltage is measured and yields magnetization in units of quanta of flux.

The main downside of SQUID is cost. The machines are much more complex than for VSM and require the use of cryogenics since there are no room temperature superconductors. The sample itself can be held at different temperatures including room temperature.

2.3 Magnetization Dynamics

Macroscopic magnetic phenomena are described using the magnetization vector defined by

$$M = \frac{1}{V}\sum_i m_i \tag{2.16}$$

where m_i is the magnetic moment from the ith lattice site in the material and V is the total volume. We can see that the magnetization thus represents an average effect from the material making it suitable for describing macroscopic phenomena.

In the case of a ferromagnet below the Curie temperature all the spins point along the magnetization to a good approximation. Therefore the dynamics of the magnetization can be described the same way we describe a single moment precessing in an external field [23]

$$\frac{dM}{dt} = -\gamma M \times H_{eff} \tag{2.17}$$

The above is known as the Landau-Lifshitz (LL) equation. γ is the gyromagnetic ratio given by $g\mu_B/\hbar$ with g, μ_B, $\hbar$ are the Lande g factor, the Bohr magneton and Planck's constant respectively. H_{eff} is the total effective field on the magnetization including the external field, the dipolar field and the exchange field. The LL equation states that magnetization dynamics are entirely determined by field strength. Furthermore it can be solved to determine the frequency of precession.

$$\omega = \gamma H_{eff} \tag{2.18}$$

However the LL equation does not do a complete job in describe magnetization dynamics. If the system isn't driven externally, then the amplitude of the precession will decay over time such that the magnetization points along the effective field direction to minimize magnetic free energy. The LL equation is thus modified to take this decay into account

$$\frac{dM}{dt} = -\gamma M \times H_{eff} + \frac{\alpha}{|M|} M \times \frac{dM}{dt} \tag{2.19}$$

equation 2.19 is known as the Landau-Lifshitz-Gilbert (LLG) equation. The last term describes the phenomenological damping and the α parameter characterizes the strength of this damping and is known as the Gilbert damping constant. The damping term is phenomenological and damping has many different sources. As such it cannot typically be predicted from theoretical calculations and must be measured using techniques such as FMR or BLS.

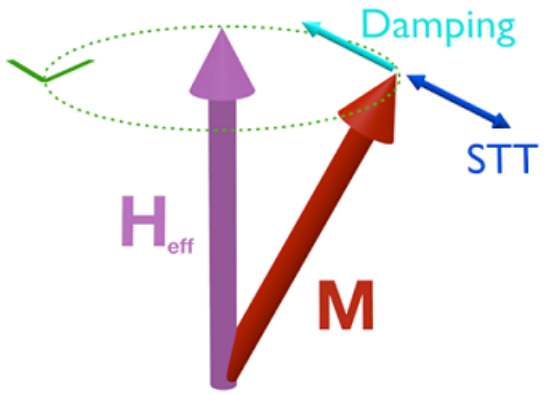

Figure 2.5: Magnetization Dynamics

The effective damping can be controlled by outside factors as well. Injection of spin or spin-polarized current will create a Spin Transfer Torque (STT) which can have a component acting with or against the damping. In the case where the STT term overcomes the damping term the possibility of self-sustaining oscillations opens up. These are known as Spin Torque Oscillators. Details about STT and STOs will be covered in the following section. Figure 2.5 shows a schematic of the motion of the magnetization as well as the forces acting on it.

2.3.1 Magnetization Dynamics in the Presence of Anisotropy

To examine magnetization dynamics we will first consider the damping free case where the LLG equation is given by:

$$\frac{dM}{dt} = -\gamma M \times H_{eff} \tag{2.20}$$

this is the same equation we have seen previously; however we must consider more carefully what H_{eff} should be. As we have seen previously, magnetic fields in materials are reduced by demagnitization factors which are anisotropic.

If we consider the case of an ellipsoid with demagnetization factors $N_x, N_y and N_z$

respectively, and the case of an external field in the z direction (H_z) causing oscillations in the x direction (H_x) then the vector components of the magnetic field are:

$$Heff_x = H_x - N_x M_x \tag{2.21a}$$

$$Heff_y = -N_y M_y \tag{2.21b}$$

$$Heff_x = H_z - N_z M_z \tag{2.21c}$$

entering these expressions for the magnetic fields into eq. 2.20 yields the following:

$$\frac{dM_x}{dt} = \gamma[H_z + (N_y - N_z)M_z]M_y \tag{2.22a}$$

$$\frac{dM_y}{dt} = \gamma[M_z H_x + (N_x - N_z)M_x M_z - M_x H_z] \tag{2.22b}$$

$$\frac{dM_z}{dt} \approx 0 \tag{2.22c}$$

we solve these equations by assuming an oscillating time dependence $e^{-i\omega t}$ and obtain a result for the susceptibility $\chi_x = M_x/H_x$

$$\chi_x = \frac{\chi_0}{1 - (\omega/\omega_0)^2} \tag{2.23}$$

where

$$\chi_0 = \frac{M_z}{H_z + (N_x - N_x)M_z} \tag{2.24}$$

and the resonance frequency ω_0 is

$$\omega_0 = \gamma\sqrt{(H_z + (N_y - N_z)M_z)(H_z + (N_x - N_z)M_z)} \tag{2.25}$$

in the case of an infinite plane ($N_x = N_z = 0, N_y = 4\pi$) equation 2.25 reduces to

$$\omega_0 = \gamma\sqrt{B_z H_z} \tag{2.26}$$

in the case of a sphere ($N_x = N_y = N_z = 4\pi/3$) it reduces to

$$\omega_0 = \gamma H_z \tag{2.27}$$

finally in the case of an infinite cylinder ($N_x = N_y = 2\pi, N_z = 0$ it reduces to

$$\omega_0 = \gamma(H_z + 2\pi M_z) \tag{2.28}$$

A striking feature of these results is that only in the specific cases of a sphere and a plane does the frequency disappear at zero field. Therefore in the case of a sample uniformly magnetized in a single direction there should be nonzero oscillations at zero applied field.

If we take into account magnetocrystalline anisotropy eq. 2.25 is modified by adding to the usual demagnetizing factors.

We derive the modifications by first considering the energy associated with magnetic anisotropy. In the uniaxial case this is:

$$f = K_1 sin^2(\theta) \tag{2.29}$$

where f is the energy per unit volume of the material, K_1 is the leading term of the anisotropy constants and θ is the angle between the easy axis and the applied field.

To simplify analysis we treat the effects of anisotropy as the presence of an effective magnetic field. We define this anisotropy field such that the torque it would apply is equivalent to the torque exerted by the anisotropy energy. This corresponds to the following:

$$\frac{\partial f}{\partial \theta} = M_s \times H^a \tag{2.30}$$

equation 3.38 does not completely define the anistropy field as either the direction or magnitude could be changed without consequency. Thus we define the direction

as being parallel to the x axis in the plane and express the magnitude as an effective demagnetizing factor

$$H_x^a = -N_x^a M_x \tag{2.31a}$$

$$H_y^a = -N_y^a M_y \tag{2.31b}$$

we then add these new effective demagnetizations to the previous ones in equation 2.25 giving

$$\omega_0 = \gamma\sqrt{(H_z + (N_y + N_y^a - N_z)M_z) \times (H_z + (N_x + N_x^a - N_z)M_z)} \tag{2.32}$$

finally we only need to find the magnitudes of these new demagnetization factors.

In the uniaxial case we have

$$\frac{\partial f}{\partial \theta} = 2K_1 sin\theta cos\theta = M_s \times H^a \approx N_x^a M_x M_z \approx N_x^a M_z^2 sin\theta \tag{2.33}$$

so for angles near $\theta = 0$ we get

$$N_x^a = \frac{2K_1}{M_z^2} \tag{2.34}$$

similarly

$$N_y^a = \frac{2K_1}{M_z^2} \tag{2.35}$$

and so the resonance condition becomes

$$\omega_0 = \gamma\sqrt{(H_z + 4\pi M_z + \frac{2K_1}{M_z})(H_z + \frac{2K_1}{M_z})} \tag{2.36}$$

and we have identified $\frac{2K_1}{M_z}$ as the anisotropy field. Note that this once again predicts oscillations at zero applied field although in practice a small biasing field is needed to overcome edge effects. Equation 2.36 is known as the Kittel equation and is useful

in predicting magnon frequencies as well as determining the strength of anisotropy.

2.4 Spin Transfer Torque

There exist processes which result in a change in the angular momentum in the magnetic layer. Such processes are described as torque of the magnetization. These so called Spin Transfer Torques (STT) will change the magnetization dynamics and can give rise to practical effects such as self-sustained oscillations or switching of the magnetic layer. In this section we will consider two types of processes which yield STT, injection of spin polarized current into a magnetic layer as well as injection of a pure spin current into a magnetic layer.

2.4.1 Spin Polarized Current

The first process which can yield Spin Transfer Torque is when a spin polarized current is injected into the magnetic layer[3, 4]. Historically, this was the first STT process discovered when considering systems exhibiting GMR or Giant Magnetoresistance in a FM/NM/FM trilayer system[1, 2]. GMR refers to the difference in resistance through the trilayer when the magnetization of the last layer is switched from parallel to Anti-parallel. Each of the magnetic layers act as a spin filter, only allowing electrons with spin aligned with the magnetization to pass through. A schematic of this can be seen in figure 2.6

The spin filtered current that passed through the first layer carries with it an angular momentum which can be transferred to the third layer. For practical applications the first layer is typically taken to be fixed. One can fix a magnetic layer by making it thicker or by pinning the magnetization using an anti-ferromagnetic layer which will pin the magnetization with exchange bias. The third layer is taken to be free and can be affected by the Spin transfer torque. The magnetization of the free layer points in the $m = M/m_s$ direction and we can write the added terms

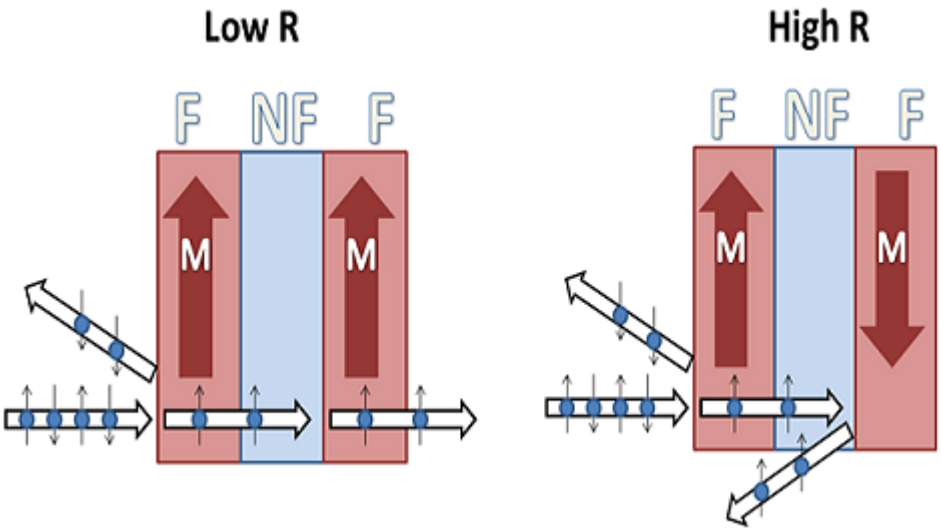

Figure 2.6: Left: low resistance state where current makes it through. Right: High resistance state where no current passes through

to the LLG equation

$$T_{STT} = \frac{1}{t}\frac{g\mu_B}{e} j_z \epsilon \mathbf{m} \times (\mathbf{m} \times \mathbf{m}_{fixed}) + \frac{1}{t}\frac{g\mu_B}{e} j_z \epsilon' \mathbf{m} \times \mathbf{m}_{fixed} \tag{2.37}$$

where t is the thickness of the free layer, g is the electron g factor, j_z is the charge current density flowing normal to the interface along the direction from the fixed to the free layer, defined as the z direction. ϵ and ϵ' are the efficiency factors for the terms which depend on the relative orientations of the two magnetizations, the geometry and material parameters. The efficiencies are typically less than one. The first term, which is typically larger, points in the same direction as the Gilbert damping and is often referred to as the Slonczewski, damping or anti-damping term depending on whether it acts with or against the damping. The second term has the same form as a precessional torque around a magnetic field and is referred to as a fieldlike torque. Since the spin polarized current cannot penetrate into the free magnetic layers, these terms exist at the interface between the magnetic layer

and the normal metal layer. The $1/t$ accounts for this by spreading the effects of the interfacial torque evenly across the entire film. Dephasing of the spin polarized current as it travels across the nonmagnetic layer causes the field like torque to be weak and negligible allowing the damping like torque to be dominant.

The practical usage of polarized charge currents is limited by the amount of angular momentum carried by a single charge carrier which is set by the efficiency factors, so typically less than one. The process is also not energetically efficient to the energy dispersed by the charge carriers. Each electron dissipates on average several tenths of an electron volt, whereas the energy required to excite a magnon is only around $10\mu ev$ leading to an inefficient process.

2.4.2 Pure Spin Currents

Spin Hall Effect

In order to make spin torque processes more efficient we look for ways to directly inject angular momentum without the need to inject a charge current. The Spin Hall Effect (SHE) is one such process[24, 25, 26].

SHE occurs at the interface between a heavy metal and a ferromagnet. When charge current is passed through the heavy metal layer, spin orbit coupling in the material will induce a perpendicular spin current. The strength of the Spin Hall effect is characterized by the spin hall angle θ_{SH} which is the ratio between the vertical spin current generated and the horizontal charge current provided. The geometry can be seen in figure 2.7.

The sign of the spin hall angle indicates the direction of the injected spin and the convention is that Platinum has a positive spin hall angle whereas Tantalum has negative spin hall angle. The terms from this Spin Orbit Torque in the LLG

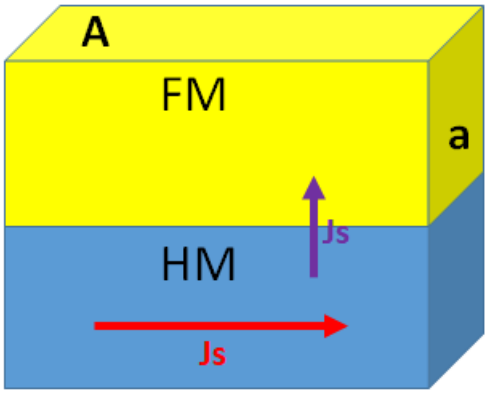

Figure 2.7: Charge current in the Heavy Metal creates a perpendicular spin current which is injected into the ferromagnet

equation are given by

$$T_{SOT} = \frac{1}{t}\frac{g\mu_b}{e}\theta_{SH}\eta j\mathbf{m}\times(\mathbf{m}\times\hat{p}) + \frac{1}{t}\frac{g\mu_b}{e}\theta_{SH}\eta j\mathbf{m}\times\hat{p} \tag{2.38}$$

where j is the in plane charge current density which flows in the direction $\hat{j}$, $\hat{z}$ is the direction perpendicular to the interface between the HM and FM. $\hat{p} = \hat{z}\times\hat{j}$ is the direction of the spin polarization of the spin current propagating in the $\hat{z}$ direction. η and η' are the efficiency factors determined by details of spin transport in the heavy metal and the spin mixing conductance at the interface. These factors are typically less than 1 and for SHE induced torques we also have $\eta' << \eta$. An important difference between Spin Transfer and Spin Orbit torques is that the orientation of the spin damping torque is determined by sample geometry in the spin orbit case, as opposed to the direction of the magnetization in the spin transfer case. Another difference is that the torque is determined by an in plane current for SOT instead of in plane for STT which is critical in improving efficiency.

The overall efficiency of the spin torque generated by the Spin Hall Effect is the total rate at which angular momentum is absorbed by the magnetic layer per

unit charge current. The efficieny is given by

$$\frac{T_{SOT}A}{ja} = \eta\theta_{SH}\frac{A}{a}\frac{g\mu_B}{e} \tag{2.39}$$

where A is the large cross-sectional area looking down at the sample from the top which is where the spin current flows and a is the smaller cross-sectional area on the side of the sample where the charge current flows. This ratio can be as large as 30 even for a small sample. Therefore, the torque can be over an order of magnitude more efficient than one quantized unit of spin per quantized unit of charge which is the limit for the case of spin polarized current.

The simplest way to think about this is that each electron in the charge current is used multiple times to transfer torque to the ferromagnet. The electrons become polarized by the spin-orbit coupling when they deflect to the ferromagnet. Then at the interface they transfer angular momentum to the magnetization the same way they would in the case of a spin polarized current. However, since there is no net charge flow to the magnetic layer the electrons must diffuse back to the heavy metal where the process can repeat. The relevant length scale is then the spin diffusion length, which is typically on the order of nanometers allowing for many cycles to take place even in a small sample.

The issue which limits the practicality of these devices is that materials with high spin orbit coupling also have high resistances. This raises the issue of power efficiency and ohmic heating. These issues require carefuly consideration of sample geometry and spin orbit torque based devices can be significantly more power efficient than spin transfer torque based devices.

2.4.3 Spin Seebeck Effect

Another way of generating a pure spin current is by inducing a temperature gradient in what is known as the Spin Seebeck effect[10].

The Spin Seebeck Effect (SSE) was first demonstrated in 2008[9]. The experimental configuration is the following: two ferromagnetic strips are separated by a nonmagnetic metal. A current is driven through the first ferromagnet to provide asymmetric heating. A voltage is measured across the second ferromagnet. A nonzero voltage indicates the presence of the Inverse Spin Hall Effect and is as such evidence that a spin current has passed through the nonmagnetic metal from one FM to the other.

The first striking result from this experiment is that the ISHE voltage persists for separations on the order of millimeter despite the spin diffusion length in the NM being on the order of microns. Therefore conduction electrons cannot be responsible for carrying the Spin Seebeck generated spin currents. Instead it is the magnons which carry the spin currents. This was verified later when the SSE was measured using an insulating ferromagnet [27] where no conduction electrons are present to transport spin.

The Spin Seebeck effect arises from a nonequilibrium between the magnons in the ferromagnet and the conduction electrons in the normal metal. In some cases the nonequilibrium phonons also play a role.

There are two kinds of Spin Seebeck effects. The first, described above is the tranverse Spin Seebeck Effect where the spin current is perpendicular to the temperature gradient. However, there can also be generation of spin current parallel to the temperature gradient. This is the second SSE known as the longitudinal Spin Seebeck Effect. Tranverse SSE can occur in both metals and insulators but longitudinal SSE can only occur in magnetic insulators.

The Spin Seebeck Effect is very important for applications since temperature gradients will always exist in practical devices. Typically heating is a problem as energy radiated away as heat is wasted so heating must be minimized to improve efficiency. SSE provides another avenue to increasing efficiency which is to use the

heating as a source of spin current. The heating is now built into the functionality of the device, improving efficiency. Spin Seebeck devices are also highly scalable with output power proportional to the length perpendicular to the temperature gradiant.

2.4.4 Magnetization Reversal

While both the field like and the damping like torques have the potential to affect magnetization dynamics in interesting and useful ways, typically the damping like torque does so much more efficiently.

The first effect discussed is magnetization reversal. A large anti-damping torque can destabilize the magnetization sufficiently to induce a reversal. The anti-damping torque must induce precessions for switching to occur. If the magnetization is in plane, then the magnetization precesses elliptically, tilting in and out of plane. The out of plane tilts create a large demagnetizing field which increases magnetic energy losses. The energy losses must be compensated by the anti-damping torque. Perpendicularly magnetized systems will precess circularly, only tilting in plane which causes smaller demagnetization. Therefore, perpendicular magnetization is preferable for switching applications since the required current is smaller. Materials with perpendicular magnetic anisotropy have therefore become much sought after.

There is however an issue with using PMA materials for these memory applications. The in plane torque is typically in the sample plane and therefore does not favor either magnetization direction (up or down). This is a problem because applications require deterministic switching. The symmetry between the directions must be broken which can be done by applying an in plane field parallel or anti-parallel to the current direction which will favor a given torque direction. The state with zero torque will now occur at nonzero current and depend on the direction of the field and the sign of the current. Removing the current will then cause the magnetization to relax in the direction of the tilt. The additional requirement of a

magnetic field causes design issues which can be solved by using exchange bias from an Anti-Ferromagnet or a magnetic dipole interaction with a nearby magnetic layer.

Controllable and efficient switching of magnetization is of great use to a number of memory applications meaning that SOT can be of great use for future technologies.

2.4.5 Spin Torque Oscillators

In the case where the magnetic system only has one equilibrium position the negative damping torque will not induce switching. Instead the amplitude of the magnetization precession will increase. When the magnitude of the spin torque term matches the magnitude of the damping term in the LLG equations the magnitude of the oscillations will dramatically increase and the system will undergo self-sustaining oscillations. This is often referred to as the auto-oscillatory regime. These oscillations can have frequencies from the 100 MHz to the tens of GHz range depending on the magnetic system. These magnetic oscillations will result in voltage oscillations due to magneto-resistive effects which in turn will cause microwave emission. These microwave oscillators can form key components in spintronic circuits. Spin Torque Oscillators (STOs) are particularily attractive since the frequency of the oscillations can be controlled by varying the DC current and because the power output can be increased via synchronization of multiple oscillators.

Some of the key challenges facing STOs are:

1. increasing the frequency of oscillations in order to enable high clock speeds
2. increasing output power of generated microwaves
3. increasing spectral purity of the oscillations
4. improving frequency tunability
5. lowering the required Direct Current

Some of the ways scientists have used to improve performance in these areas include: synchronizing several STO's in order to improve output power[28, 29, 30, 31], increasing the active area of oscillations by extending into 1 spatial dimension in hopes of improving output power, exploring different magnetic materials to increase frequency, finding new measurement techniques to detect higher frequency oscillations, synching STO's to an external drive frequency to increase spectral purity[32, 33], developing lower damping materials to reduce the required current[34, 35], exploring thermally driven oscillator's to make use of Joule heating and reduce required current as well as heat waste[36, 37] and finally exploring unique properties of higher dimensional oscillators in order to improve frequency tunability.

One particularily interesting application of spin torque oscillators is the possibility of using them as building blocks for neuromorphic computing. The idea behind neuromorphic computing is that the neurons in the brain act as nonlinear oscillators which interact in further nonlinear ways to process information [38]. It has already been experimentally demonstrated that STOs can be formed into neuromorphic computers achieving spoken digit recognition on par with state of the art neural networks [8]. The nonlinearity, ability to interact with one another, long lifetime and low energy consumption make Spin Torque Oscillators very promising candidates for larger scale neuromorphic computing.

2.5 DMI

The Dzyaloshinksii-Moriya interaction was first proposed in 1957 by I.E. Dzyaloshinskii [39] to explain the weak ferromagnetic moment in antiferromagnetically ordered αFe_2O_3 (Hematite). Hematite has two antiferromagnetic phases, one with spins along the crystal axis and one with the spins lying in one of the symmetry planes. However only the latter state shows the weak ferromagnetism. This led Dzyaloshinskii to explore the symmetry properties for both states. He came to the conclusion

that in the state with weak ferromagnetism a new interaction which rotates the spins is allowed by symmetry. This rotation is forbidden in the state without weak ferromagnetism. The spins are this still in antiferromagnetic order, but have rotated such that there is now a canting and a net magnetic moment.

The description of the interaction in Dzyaloshinskii is phenomenological. Three years later, Toru Moriya[40] formalized the interaction as an anisotropic superexchange process and gave it its Hamiltonian form:

$$D \cdot [S_1 \times S_2] \tag{2.40}$$

The term above arises as the largest contribution to the anisotropic superexchange and is linear in spin orbit coupling. Therefore systems without significant spin orbit coupling will not exhibit DMI.

In his paper Moriya also details the symmetry considerations of the coupling between two atoms. Calling the first atom A, the second B and the point exactly between the two C we get:

- If there is a center of inversion at C

$$D = 0$$

- If there is a mirror plane perpendicular to AB passing through C

$$\text{D} \parallel \text{mirror plane or D} \perp \text{AB}$$

- If there is a mirror plane including A and B

$$\text{D} \perp \text{mirror Plane}$$

- If there is a two fold rotation axis, perpendicular to AB and passing through C

$$D \perp \text{two fold axis}$$

- If there is an n fold axis(n $n \geq 2$) along AB

$$D \text{ —— } AB$$

Another symmetry consideration of the utmost importance is that of the Hamiltonian term itself which breaks inversion symmetry. Therefore the physical system considered must also break inversion symmetry. The cases originally considered by Dzyaloshinskii and Moriya were crystals with broken inversion symmetry.

However, magnetic bilayers must by construction break inversion symmetry and therefore can exhibit DMI. The following sections will consider two different classes of bilayer and detail the mechanisms which provide DMI.

2.5.1 DMI in Thin Film Bilayers

The most common form of system which exhibits strong DMI is a bilayer consisting of one magnetic layer and one nonmagnetic Heavy metal. This section will provide the theoretical framework for the existence of DMI, the consequences of DMI in such a system and finally possible applications of such bilayers will be discussed.

2.5.2 The Fert Levy Model

The Fert-Levy model which is used to explain the origin of DMI in Magnetic bilayers was originally developed to explain properties of doped Spin-Glasses[41].

Doping CuMn spin-glass alloys with heavy metal Au or Pt created a significant enhancement of the anisotropy field maintaining remnant magnetization. Fert and Levy set out to understand the interaction between the magnetic ions and the added impurities that gave rise to this enhancement.

The mechanism they proposed is that the heavy metal impurities create a spin orbit scattering of the conduction electrons of the magnetic ions. This scat-

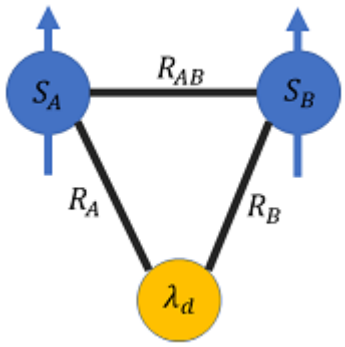

Figure 2.8: Schematic of the Fert-Levy model. Blue Atoms at sites R_A and R_B are magnetic and have spins S_A and S_B respectively. Yellow atom is at $R = 0$ and has spin-orbit coupling coefficient λ_d

tering creates an additional term in the Ruderman-Kittel-Katsuya-Yosida (RKKY) interaction. The RKKY interaction comes from the shift in ground state energy of an electron gas interacting with two localized spins.

The interaction occurs between two magnetic ions, A and B at sites R_A and R_B, and one non-magnetic impurity at $R = 0$. The ions have spins S_A and S_B and the strength of the spin orbit coupling at the magnetic impurity is given by λ_d. The geometry is detailed in figure 2.8.

The perturbation potential is taken to be

$$V = -\Gamma\delta(\vec{r} - \vec{R}_A)\vec{s}\cdot\vec{S}_A - \Gamma\delta(\vec{r} - \vec{R}_B)\vec{s}\cdot\vec{S}_B + \lambda_d(r)\vec{l}\cdot\vec{s} \tag{2.41}$$

The d-states of the impurity atoms mix with the electron gas. In particular, the conduction electrons are affected and can experience the spin-orbit coupling from the heavy metal impurity atoms. The new electronic state resulting from the mixture of the atomic d states with plane waves is given by:

$$\psi_k = exp(i\vec{k}\cdot\vec{r}) + exp(i\eta_2)sin(\eta_2)\frac{\langle d|V_0|k\rangle}{\Delta}\sum_{m=-2}^{2} Y_{2m} * (\hat{k})\psi_{2m}(\vec{r}) + ... \tag{2.42}$$

for electrons near the impurity (R close to 0). For a large R the wavefunction is given by

$$\psi_k = exp(i\vec{k}\cdot\vec{r}) + 4\pi exp(i\eta_2)sin(\eta_2)(e^{ikr}/kr)\sum_{m=-2}^{2} Y_{2m} * (\hat{k})Y_{2m}(\vec{r}) \tag{2.43}$$

where Δ is the half life of the virtual bound state,Y_2m are the spherical harmonics and η_2 is the phase shift of the $l = 2$ partial states. At the Fermi level this phase shift is given by:

$$\eta_2(E_F) = (\pi/10)Z_d \tag{2.44}$$

where Z_d is the number of d electrons. The matrix element $\langle d|V_0|k\rangle$ is related to the density of states for a given spin orientation at the Fermi level as follows

$$|\langle d|V_0|k\rangle|^2 = 4\Delta/N(E_F) \tag{2.45}$$

We can therefore write the lowest order correction to the ground state energy due to the perturbation given by equation 2.41 which includes a contribution from all three atoms

$$E^{(3)} = P\int_{k_1}^{k_F} d^3k_1 \int\int d^3k_{2,3}[\zeta - \frac{\pi^2}{3}\delta(E_2 - E_1)\delta(E_3 - E_1)]Tr_\sigma V_{\vec{k_1}\vec{k_2}} V_{\vec{k_2}\vec{k_3}} V_{\vec{k_3}\vec{k_1}} \tag{2.46}$$

where $A = (\frac{1}{8\pi^3})^2$, $\zeta = [\frac{1}{(E_1-E_2)(E_1-E_3)}]$ and P denotes the principal part of the integral. In physical systems, the magnetic ions are far from the impurity and as such we use the form of equation 2.43 when calculating the exchange terms (Γ). Since the spin-orbit coupling occurs at or near the impurity we use the form of equation 2.42 when calculating the spin-orbit terms. The trace over the conduction electron spin states is given by

$$Tr_\sigma(\vec{S_A}\cdot\vec{s})(\vec{s})(\vec{S_B}\cdot\vec{s}) = (-i/4)(\vec{S_A}\times\vec{S_B}) \tag{2.47}$$

Now we can finally perform the integration in equation 2.46, and keeping the leading term in $(1/r)$ that is trilinear in the three parts of the perturbation we get

$$H_{DM} = -V_1 \frac{sin[k_f(R_A + R_B + R_{AB}) + (\pi/10)Z_d]\hat{R_A} \cdot \hat{R_B}}{R_A R_B R_{AB}} (\hat{R_A} \times \hat{R_B}) \cdot (\hat{S_A} \times \hat{S_B}) \tag{2.48}$$

with

$$V_1 = (135\pi/32)(\lambda_d \Gamma^2 / E_F^2 k_f^3) sin[(\pi/10)Z_d] \tag{2.49}$$

Where R_A, R_B, R_{AB} are the lengths of the three sides of the triangle seen in figure 2.8, λ_d is the spin orbit coupling constant of a d electron and we have assumed one conduction electron per Heavy Metal atom.

We can identify the energy term given by equation 2.48 as being of the Dzyaloshinskii type since it is proportional to $(S_A \times S_B)$. Furthermore, we note that if the three atoms are aligned the whole term becomes zero. The impurity being offset from the two magnetic ions provides the inversion symmetry breaking which is crucial to the existence of DMI. The impurity atom also supplies the spin-orbit coupling which is essential as well.

Magnetic Bilayers

The formalism developed for impurity atoms also applies to the bilayer case[42]. At the magnetic interface we can have three atom configurations completely analogous to the case of the magnetic impurities where there is mixture between two of the atoms from the magnetic layer and one of the atoms from the heavy metal layer.

Yang et Al performed ab initio calculations to evaluate the distribution of DMI energy in a Co/Pt bilayer[43]. They found that the DMI is primarily located in the first layer of Co. The spin orbit coupling on the other hand is primarily located in the first layer of Pt. This confirms that DMI in HM/FM bilayers in an interfacial effect. As we increase the thickness of the magnetic layer we expect a

$1/t$ dependence of any effect which depends on the strength of DMI, since DMI is generated at the interface and so as thickness increases the percentage of the material which contributes to DMI decreases. This effect has been demonstrated several times[44, 45, 46, 47], however other magnetic effects can change the thickness dependence and mask the intrinsic $1/t$ dependence[48, 49].

The same $1/t$ dependence is not seen as we change the thickness of the Heavy Metal layer. This layers properties are not affected by the strength of DMI which only affects the magnetic layer so we don't see dilution. In fact we see an increase in the strength of DMI as we increase the thickness of the HM layer. This is because even though most of the spin orbit coupling contribution is from the first layer, layers further away from the interface also contribute. The three atom model from Fert-Levy still applies here and increasing the Heavy Metal thickness increases the number of available Heavy Metal atoms to from the three atom system.

We should expect this effect to saturate as eventually the added layers will be too far away from the interface to contribute anything meaningful. This saturation was observed in Co/Pt bilayers[46, 50]. the strength of DMI in this case saturated at 3nm of Pt.

In the Fert-Levy model, the spin-orbit coupling comes from a mixture of the electronic states of the heavy metal atom and the ferromagnetic atoms. As such, it is natural to ask whether the choice of Heavy Metal atom will affect the strength of DMI. We would expect that the differences in band filling when changing Heavy Metal atom would affect the mixture and thus the strength of DMI.

The effect of atomic composition was studied by Xin et al[51]. In their paper they changed their choice of Heavy metal going along the periodic table from Tantalum all the way to gold. In all cases the FM used was CoFeB. They found that not only does the choice of HM affect the strength of DMI by up to an order of magnitude but also in sign. Therefore the choice of HM layer is crucial when

designing structures for DMI.

2.5.3 Rashba Effect Induced DMI

The previous section detailed a model for the cause of DMI which relies on the presence of heavy metal atoms, either as impurities or at an interface. However DMI can arise even in the absence of these atoms. Spin orbit coupling is still required for DMI. The spin orbit coupling in this case comes from the Rashba effect[52].

The Rashba Effect

Crystals which lack inversion symmetry should have Spin Orbit coupling which is odd in momentum due to symmetry considerations. The simplest form of this is SOC linear in momentum. Such a SOC is known as the Rashba effect.

The effect is often derived phenomenologically. The lack of inversion symmetry in the crystal is expressed as an electric field $\vec{E} = E_z\hat{z}$. An electron moving in this electric field at velocity v will experience a magnetic field $B = -(v \times \vec{E})/c^2$ this magnetic field couples to the electron spin via the Zeeman effect.

$$H_{SO} = \frac{g\mu_B}{2c^2}(v \times \vec{E}) \cdot \sigma \tag{2.50}$$

where $\frac{g\mu_B}{2c^2}$ is the magnetic moment of an electron. Using the fact that $\vec{E} = E_z\hat{z}$ we obtain the Rashba Hamiltonian

$$H_R = \alpha(\sigma \times \rho) \cdot \hat{z} \tag{2.51}$$

where $\alpha = \frac{g\mu_B E_z}{2mc^2}$ is the Rashba coefficient. This hamiltonian will induce a momentum dependent splitting of the electron bands.

The above derivation is not entirely accurate since the electronic wavefunction will be distorted by the lack of inversion symmetry. Nevertheless the result is

still useful and is a good approximation. The Rashba effect like all other spin Orbit Coupling effects in intrinsically relativistic.

DMI from Rashba

Rashba effect induced DMI was first proposed for magnetic impurities residing in a nonmagnetic film where the interactions between two magnetic ions are mediated by free electrons via the RKKY interaction. The free electron band is then modified by Rashba Spin Orbit Coupling (RSOC) and DMI can arise. However it is more interesting to apply this model to ferromagnetic films where both RSOC and spin polarization of the electron bans must be accounted for. Such a treatment is given Kundu and Zhang [53]

Assuming a two dimensional film with uniform magnetization m we can write the following Hamiltonian:

$$H_o = -\frac{\hbar^2}{2m}\nabla^2 + J\sigma \cdot m + \alpha(-i\hbar\nabla \times \hat{z}) \cdot \sigma \tag{2.52}$$

where the first term describes the kinetic energy, the second term describes the exhange coupling between the conduction electron and the magnetization (with J as the exchange constant) and the last term describes the RSOC (with α characterizing the strength of RSOC). $\hat{z}$ is the axis perpendicular to the film and σ is the pauli vector. Equation 2.52 is the simplest, one body free Hamiltonian that includes the two essential properties of ferromagnetic films: spin polarized bands and spin orbit coupling.

Equation 2.52 yields the following energy dispersion:

$$\epsilon_{ks} = \frac{\hbar^2 k^2}{2m} + s|Jm + \alpha(\hbar k \times \hat{z})| \tag{2.53}$$

where $s = \pm 1$ represents the two spin split bands. The direction of the spin polar-

ization is momentum dependent and given by:

$$\hat{n}_s = s\frac{Jm + \alpha(\hbar k \times \hat{z})}{|Jm + \alpha(\hbar k \times \hat{z})|} \tag{2.54}$$

the wave function of the free electrons is:

$$\psi_{ks}(r) = \frac{1}{\sqrt{A}} e^{ik\cdot r}\chi_s(k) \tag{2.55}$$

where A is the area of the thin film and $\chi_s(k)$ is the spin part of the wave function which satisfies:

$$(\sigma \cdot \hat{n}_s)\chi_s(k) = s\chi_s(k) \tag{2.56}$$

if we imagine perturbing the direction of two spins S_1 and S_2 at positions R_1 and R_2 away from the average magnetization m we get the following perturbation Hamiltonian.

$$H' = V_0 \sum_{i=1,2} \delta(r - R_i)\sigma \cdot \Delta S_i \tag{2.57}$$

where $V_0 = Ja_0^2$ is the exchange potential, the δ function represents a zero range interaction between the magnetic moment and the conduction electron and $\Delta S_i = S_i - m$ is the deviation of the spin away from its average value.

We use the perturbation Hamiltonian to calculate corrections to the energy dispersion. The first order perturbation would yield a single site correction which cannot account for DMI since DMI must be an interaction between two sites. So we must take a second order perturbation theory

$$\delta E = \sum_{ks,k's'} |\langle\psi_{ks}|H'|\psi_{k's'}\rangle|^2 \frac{f_{ks} - f_{k's'}}{\epsilon_{ks} - \epsilon_{k's'}} \tag{2.58}$$

where f_{ks} is the fermi distribution function which is equal to 1(0) if the energy of

state ks is below (above) the fermi energy and

$$\begin{aligned} & A^2V_0^2|\langle\psi_{ks}|H'|\psi_{k's'}\rangle|^2 \\ & = |(p_1^{ss'} + ip_2^{ss'}) \cdot (\Delta S_1 e^{i(k-k')\cdot R_1} + \Delta S_2 e^{i(k-k')\cdot R_2})|^2 \\ & = \textstyle\sum_{ij=1,2}(p_i^{ss'} \cdot \Delta S_j)^2 + 2(p_i^{ss'} \cdot \Delta S_1)(p_i^{ss'} \cdot \Delta S_2) \times cos[(k-k') \cdot R_{12}] \\ & \quad +2(p_1^{ss'}{}_2^{ss'}) \cdot (\Delta S_1 \times \Delta S_2) sin[(k-k') \cdot R_{12}] \end{aligned} \tag{2.59}$$

where $R_{12} = R_1 - R_2$ and the real and imaginary parts of the spin matrix element are defined as $\langle\chi_s(k)|\sigma|\xi_{s'}(k')\rangle \equiv p_1^{ss'} + ip_2^{ss'}$.

Only one term in equation 2.59 is asymmetric with respect to inverting S_1 and S_2, the last term which contains $\Delta S_1 \times \Delta S_2$. In fact, this term is antisymmetric under such an exchange and acquires a minus sign. All other terms are symmetric when inverting S_1 and S_2. Recalling that $\Delta S = S_i - m$ we can write $\Delta S_1 \times \Delta S_2 = S_1 \times S_2$ and so from equation 2.58 and 2.59 we can identify

$$E_{DM} = D_{12} \cdot (S_1 \times S_2) \tag{2.60}$$

where

$$D_{12} = \frac{V_0^2}{8\pi^4} \sum_{ss'} \int dk \int dk' (p_1^{ss'} \times p_2 ss') \frac{f_{ks} - f_{k's'}}{\epsilon_{ks} - \epsilon_{k's'}} \times sin[(k-k') \cdot R_{12}] \tag{2.61}$$

It is not practical to perform analytical integration over k,k' as it is quite complex in general. However it is still possible to notice some general features of equation 2.61.

The first is that the direction of D is set by the following vector additions:

$$D_{12} = A\hat{R}_{12} + B\hat{z} \times \hat{R}_{12} + C\hat{m} \tag{2.62}$$

The relative strength of the three parameters A,B and C is set by the strength

of RSOC relative to the strength of the exchange coupling. The last term proportional to C will not induce chirality into the magnetic system and can generally be ignored when considering the effects of DMI.

Another feature that can be noted is that the coefficient D_{12} will undergo an oscillatory decay as the distance between R_1 and R_2 increases, similarly to the conventional RKKY. Noting that the denominator of equation 2.61 contains the energy difference between occupied and unoccupied states we can say that the largest contribution to the integral over k,k'comes from k states near the fermi energy. As such the sine function will oscillate with period $2k_F R_{12} = 2\pi$.

There are two limiting cases where the integration of equation 2.61 can be simplified. The first is when J=0 which is the case of a nonmagnetic film. This is not very interesting since we want to understand DMI in magnetic films. The second case is when exchange coupling is much stronger that Rashba Spin Orbit Coupling ($J \gg \alpha$)

We simplify by only keeping terms of the lowest order in α from equation 2.61. To zeroth order in α D = 0 and there is no asymmetric contribution and no DMI. So we must take DMI to the first order in α. Furthermore, eq 2.61 would be identically zero if we kept $p_1^{ss'} \times p_2^{ss'}$ to the zeroth order in α $\epsilon_{ks} - \epsilon_{k's'}$ to the first order in α. Thus to find DMI to the first order in α we must discard the terms proportional to α in the dispersion of eq.2.53. We are left with

$$\epsilon_{ks} - \epsilon_{k's'} = \frac{\hbar^2 k^2 - \hbar^2 k'^2}{2m} + (s - s')J \tag{2.63}$$

we must also calculate $p_1^{ss'} \times p_2^{ss'}$ to the first order in α. Tedious calculation yields:

$$p_1^{ss'} + ip_2^{ss'} = -\hat{z} - is\frac{\alpha\hbar}{2J}(k - k') \quad (for\ s = s') \tag{2.64}$$

and

$$p_1^{ss'}+ip_2^{ss'} = s\frac{(k-k')\times\hat{z}}{|k-k'|}-i(\hat{m}+\frac{\alpha\hbar}{2J}(k+k')\times\hat{z})\times\frac{(k-k')\times\hat{z}}{|k-k'|} \quad (for\ s\neq s') \tag{2.65}$$

and so

$$p_1^{ss'}\times p_2^{ss'} = -s\frac{\alpha\hbar}{2J}(k-k')\times\hat{z} \quad (for\ s=s') \tag{2.66}$$

and

$$p_1^{ss'}\times p_2^{ss'} = -s(\hat{m}+\frac{\alpha\hbar}{2J}(k+k')\times\hat{z}) \quad (for\ ') \tag{2.67}$$

By substituting equations 2.63-2.67 into equation 2.61 the angular parts of the k,k' can be integrated out. The following variable changes are made to simplify notation: $x = kR_{12}$,$x' = k'R_{12}$, $k_{F\pm} = \sqrt{2m(\epsilon_F \mp J)}/\hbar$, $\Delta = 2mJR_{12}^2/\hbar^2$, $\xi_\pm = k_F \pm R_{12}$, $\epsilon_F = \hbar^2 k_f^2/2m$

we can now finally obtain an expression for DMI:

$$D_{12} = (\hat{z}\times\hat{R}_{12})(\frac{2m}{\hbar})^2\frac{V_0^2\alpha\hbar)}{4\pi^2 R_{12}}[I_0(\xi_+,\xi_-)+I_1(\xi_+,\xi_-)] \tag{2.68}$$

Where I_0 and I_1 represent the intraband and interband contributions respectively.

$$I_0(\xi_+,\xi_-) = \frac{1}{\Delta}\int_{\xi_-}^{\xi_+}dx\int_0^\infty dx'\frac{G_+(x,x')}{x^2-x'^2} \tag{2.69}$$

and

$$I_1(\xi_+,\xi_-) = \frac{1}{\Delta}\int_{\xi_-}^{\xi_+}dx\int_0^\infty dx'\frac{G_+(x,x')}{x^2-x'^2-2\Delta} - 4\int_0^{\xi_+}dx\int_{\xi_+}^\infty dx'\frac{G_+(x,x')}{(x^2-x'^2)^2-4\Delta^2} \tag{2.70}$$

where

$$G_\pm(x,x') = xx'[xJ_1(x)J_0(x')\pm x'J_0(x)J_1(x')] \tag{2.71}$$

with J_0, J_1 being Bessel functions of the first kind.

now that DMI from RSOC has been calculated it is a reasonable question to

ask whether or not it can ever be observed in real systems.

One system that has shown RSOC DMI is a Co/graphene bilayer. The bilayer provides the inversion symmetry breaking essential for both DMI and the Rashba effect. Fert-Levy type DMI us ruled out because graphene is composed of Carbon atoms which do not exhibit strong spin orbit coupling therefore the three site impurity model cannot apply.

Furthermore in their paper Yang et Al[54]. performed a calculation to determine which layers were contributing to SOC and DMI. Unlike the previous result on Co/Pt where DMI was in Co and SOC was in Pt, both DMI and SOC are entirely in the Co layer. What the graphene is contributing is a Rashba effect in the Co whose free electrons are being subjected to the modified RKKY interaction detailed earlier in this section. As such this mechanism has been shown to contribute significant DMI. (order of magnitude is same as traditional FM/HM bilayers)

2.5.4 Effect of DMI on Spin Wave Dispersion

The presence of DMI will impact properties of spin waves such as frequency dispersion, decay length and even amplitude. Predictions for the effect can be made both from a quantum and a classical approach. Both approaches follow the methods of Moon et Al[55].

Quantum Spin Wave Theory

Restricting to the simpler case of a one dimensional chain of spins lying in the x direction and the symmetry breaking in the y direction by the symmetry rules of Moriya we must have the D vector in the z direction. The Hamiltonian for the DM interaction is thus given by:

$$H_{DM} = -2\frac{D_0}{\hbar^2}\sum_j \hat{z}\cdot(S_j \times S_{j+1}) \tag{2.72}$$

where D_0 is the DM energy. Rewriting in terms of raising and lowering operators $S_j^+ = S_{jx} + iS_{jy}$ and $S_j^- = S_{jx} - iS_{jy}$ yields

$$H_{DM} = \frac{D_0}{i\hbar^2} \sum_j (S_j^+ S_{j+1}^-) - S_j^- S_{j+1}^+ \tag{2.73}$$

Again for simplicity the case where magnetization is pointing along the direction of D_{ij} is treated since it will result in the largest asymmetry. In addition, only nearest neighbour exchange is considered. Making a Holstein-Primakoff transformation while assuming the number of flipped spins in the system is small compared to the total number of spins, i.e. that we are close to the ferromagnetic ground state, we can approximate $S_j^+ (S_j^-)$ as $\hbar\sqrt{2s}a_j(\hbar\sqrt{2s}a_j^+)$ where s is the total spin at the atomic site and a_j and a_j^+ are the magnon annihilation and creation operators respectively. Substituting these definitions into equation 2.73

$$H_{DM} = \frac{2sD_0}{i} \sum_j (a_j a_{j+1}^+ - a_j^+ a_{j+1}) \tag{2.74}$$

fourier transforming the operators and summing over j we get

$$H_{DM} = \frac{2sD_0}{i} \sum_k (e^{-ika} a_k a_k^+ - e^{ika} a_k^+ a_k) \tag{2.75}$$

where a is the lattice constant. The contribution to the magnon energy from equation 2.75 is given by

$$H_{DM}^{magnon} = -4sD_0 \sum_k sin(ka) a_k^+ a_k = \sum_k \hbar\omega_k^{DM} \hat{n}_k \tag{2.76}$$

where $\hat{n}_k = a_k^+ a_k$ is the number operator for magnons with wave vector k. From this we can identify how DMI affects the spin wave dispersion.

$$\hbar\omega_k^{DM} = -4sD_0 Sin(ka) \tag{2.77}$$

in the limit of small k the dispersion becomes

$$\hbar\omega_k^{DM} = -4sD_0ka \tag{2.78}$$

This contribution to the spin wave dispersion is asymmetric and linear in k. Therefore if one can measure the asymmetry in spin wave dispersion one can measure the strength of DMI.

The Quantum approach gives us a qualitative form of the dispersion which can guide experiments. However to extract an actual value for D one needs a more quantitative form of the dispersion which can be found by considering classical spin waves.

Classical Spin Wave Theory

We can derive a similar form from a classical theory considering spins propagating in the x direction with magnetization in the z direction which is in plane and perpendicular to the propagation of the spins. We then have

$$\hat{m} = \rho\hat{z} + m_0 exp[i(kx - \omega t)]exp[-x/\Lambda] \tag{2.79}$$

where $m_0 = (m_x, m_y, 0)$, $|m_0| << 1$, $p = \pm 1$ and Λ is the spin diffusion length. The spin wave dynamics are governed by the LLG equation

$$\frac{\partial\hat{m}}{\partial t} = -\gamma\hat{m} \times \mu_0 H_{eff} + \alpha\hat{m} \times \frac{\partial\hat{m}}{\partial t} \tag{2.80}$$

where γ is the gyromagnetic ratio and *alpha* is the Gilbert damping. the effects of DMI, Heisenberg exchange and dipolar interaction are all contained in the effective field.

$$H_{eff} = \rho H\hat{z} + \frac{2D}{\mu_0 M_s} \triangle^2 \hat{m} - \frac{2A}{\mu_0 M_s}(\hat{z} \times \frac{\partial\hat{m}}{\partial x}) + H_{dipole} \tag{2.81}$$

where H is the applied field, A is the exchange stiffness, M_s is the saturation magnetization, $H_{dipole} = -\frac{M_s}{4}(1 - e^{-2|k|d})m_x\hat{x} - M_s(1 - (1 - e^{-2|k|d})/4)m_y\hat{y})$, the local demagnetization field is equal to M_s and the sample thickness is given by d. Inserting equations 2.79 and 2.80 into equation 2.81 and neglecting small terms proportional to $1/(k\Lambda)^2$, α^2 and $\frac{\alpha}{k\Lambda}$ gives the following expressions for frequency and dispersion length.

$$\frac{\omega}{\gamma\mu_0} = \sqrt{(H + M_s/4 + \frac{2Ak^2}{\mu_0 M_s})(H + 3M_s/4 + \frac{2Ak^2}{\mu_0 M_s}) - \frac{e^{-4|k|d}M_s^2}{16}(1 + 2e^{2|k|d})} + \rho\frac{2D}{\mu_0 M_s}k \tag{2.82}$$

and

$$\Lambda_\pm = \frac{1}{\alpha\omega}(2\gamma\mu_0 J|k_\pm| + \frac{\gamma\mu_o M_s^2 d e^{-4|k_\pm|d}(1 + e^{2|k_\pm|d})/8 \pm \rho\frac{2D}{\mu_0 M_s}(\omega \mp \gamma\mu_0\rho\frac{2D}{\mu_0 M_s}|k_\pm|)}{H + M_s/2 + \frac{2A}{\mu_0 M_s}k_\pm^2}) \tag{2.83}$$

where a + (-) corresponds to the case k > 0 (k < 0). Equation 2.82 shows that the dispersion is the sum between a term in the square root which is the dispersion in the absence of DMI, and a term linear in k. This replicates the quantum result of DMI affecting dispersion asymmetrically linearly in k. The spin wave dispersion also depends on the sign of k as long as $D \neq 0$.

In the large k limit nonlocal terms may be neglected and the terms simplify to

$$\frac{\omega}{\gamma\mu_0} = \sqrt{(H + \frac{2Ak^2}{\mu_0 M_s})(H + M_s + \frac{2Ak^2}{\mu_0 M_s})} + \rho\frac{2D}{\mu_0 M_s}k \tag{2.84}$$

and

$$\Lambda_\pm = \frac{1}{\alpha\omega}(2\gamma\mu_0\frac{2A}{\mu_0 M_s}|k_\pm| + \frac{\rho\frac{2D}{\mu_0 M_s}(\omega \mp \gamma\mu_0\rho\frac{2D}{\mu_0 M_s}|k_\pm|)}{H + M_s/2 + \frac{2Ak^2}{\mu_0 M_s}}) \tag{2.85}$$

In the small k limit more relevant to experimental conditions the exchange contri-

bution may be neglected and we can assume $|k_{\pm d}| << 1$ so now the expressions for frequency and diffusion length reduce to

$$\frac{\omega}{\gamma\mu_0} = \sqrt{H(H+M_s)} + \frac{M_s^2|kd|}{4\sqrt{H(H+M_s)}} + \rho\frac{2D}{\mu_0 M_s}k \tag{2.86}$$

and

$$\Lambda_\pm = \frac{1}{\alpha\omega}\left(\frac{\gamma\mu_0 M_s^2/4 \pm \rho\frac{2D}{\mu_0 M_s}(\omega \mp \gamma\mu_0\rho\frac{2D}{\mu_0 M_s}|k_\pm|)}{H + M_s/2}\right) \tag{2.87}$$

In this small k limit we notice that the dipolar term is linear in k, same as the DMI term. It is therefore not sufficient to extract the linear component of the dispersion to measure the strength of DMI. The key difference is that the dipolar term is symmetric whereas the DMI term is asymmetric. Therefore we get that the asymmetric, DMI induced shift in the spin wave dispersion is given by

$$f_{dmi} = \rho\frac{D}{\pi M_s}k \tag{2.88}$$

where $\rho = \pm 1$ is the direction of the magnetization, M_s is the saturation magnetization and D is the strength of the DM interaction. Measuring this shift allows for experimental investigation into DMI.

Note that the spin diffusion length is also affected by DMI. However it is not as promising experimentally because the effect is small and difficult to decouple from other competing effects.

2.5.5 Creating and Stabilizing Skyrmions

The first approach to creating magnetic Skyrmions is by using the way a spin current can affect domain walls[56]. A HM/FM/I structure is chosen and current is sent through the HM layer. The Spin Hall effect will then generate a spin current into the FM layer. The domain walls of the FM are all chiral with the same chirality which is fixed by DMI which is present thanks to the presence of a bilayer. .The

domains are all elongated "Stripe" domains. The spin hall effect can be modeled as an effective field given by:

$$\vec{B}_{sh} = B^0_{sh}[\hat{m} \times (\hat{z} \times \hat{j}_e)] \tag{2.89}$$

where $B^0_{sh} = (\hbar/2|e|) \cdot (\theta_{sh} J_c / t_f M_s)$ where e is the charge of an electron, t_f is the thickness of the magnetic layer, $\theta_{sh} = J_s/J_s$ is the spin hall angle and M_s is the saturation magnetization.

For a homogenous current along the x axis, the symmetries of equation 2.89 dictate that there is no torque on the sides of the stripe domain. There is only torque on the ends of the domain such that if one end is pinned the domain will be elongated.

The situation changes when the current is inhomogeneous. A controllable way to generate inhomogeneous current is by fabricating a constriction in the current carrying HM layer. The total current will then converge as it approaches the constriction and then diverge as it leaves the constriction. As such there will be inhomogenous torques in the y direction which expands the ends of the domains. The surface tension in the domain wall increases as the end of the domain expands and eventually the expanding domain breaks off into a circular domain which is a Skyrmion. The generated Skyrmion is topologically protected and can thus survive. The process described above for generating Skyrmions is analogous to how soap bubbles are formed when air is blown into a film. Therefore Skyrmions generated this way are known as Skyrmion bubbles.

Typically Skyrmion bubbles are on the order of micrometers in size which is too large for state of the art applications. Therefore it is desirable to find other methods which can generate smaller Skyrmions.

The key to generating smaller skyrmions is material engineering. By designing materials with the appropriate properties smaller skyrmions can be generated.

The first discovery was that materials with perpendicular magnetic anisotropy will form skyrmion bubbles under 100nm in size. Furthermore the precise size can be tuned by controlling the strength of the anisotropy [57].

Later a more detailed theory of Skyrmions was developed in which it was found that there are different types of Skyrmions [17]. The micrometer sized Skyrmions first discovered are known as bubble Skyrmions and are well studied.

The smaller Skyrmions found in PMA materials can actually be classified into two categories based on what the stabilizing force is.

The larger Skyrmions (above 10nm in size) are stabilized by stray fields from the magnetization. There can also be even smaller Skyrmions (less than 10nm in size) which are stabilized by the DMI itself.

Both types of Skyrmions have a stable energy minimum at a finite radius. Typically the energy minimum is lower for the stray field Skyrmions and so in order to generate the smallest Skyrmions in order to be useful for practical applications we need to supress the formation of stray field Skyrmions by minimizing the saturation magnetization.

However we run into a problem doing this. In ferromagnetic materials M_s and $K_\perp$ are not independent. Minimizing M_s will also lower anisotropy and possibly change the magnetization to being in plane or otherwise affect the formation and size of Skyrmions. To avoid this problem we can turn to ferrimagnets where anisotropy and magnetization are decoupled. By manufacturing ferrimagnets close to the saturation point we can minimize M_s while leaving anisotropy unchanged. As such ferrimagnets are promising candidates for practical skyrmionic applications.

2.5.6 Moving Skyrmions

Once Skyrmions are formed they can be moved by spin orbit torque generated by applied currents[16, 58, 59, 60]. The motion can be described by the Thiele equation

developed to describe the dynamics of magnetic solitons.

$$F + G \times v + \alpha D v = 0 \tag{2.90}$$

where F is the force applied by the Spin Hall Effect sombined with the repulsion from the edges, G is a gyrovector directed out of plane and proportional to the Skyrmion number and D is the dissipative tensor determined by the parameters of the Skyrmion. For a Skyrmion purely driven by the SHE the longitudinal(V_x) and transverse(V_y) velocites are given by:

$$v_x = \frac{\delta}{1+\delta^2}\frac{F_{SHE}}{G_z} \tag{2.91}$$

$$v_y = \frac{1}{1+\delta^2}\frac{F_{SHE}}{G_z} \tag{2.92}$$

we can define the Skyrmion Hall angle θ_{SH} as the angle between the direction of Skyrmion motion and the applied current

$$\theta_{SH} = atan(|\frac{v_y}{v_x}|) = atan(\frac{1}{\delta}) \tag{2.93}$$

with $\delta = \alpha D_{xx}/G_z$ when the repulsion from the track edges is included the final longitudinal velocity is $v_x = \frac{1}{\delta}\frac{F_{SHE}}{G_z}$. There have been several demonstrations of Skyrmion motion but all of the velocities measured so far are too slow for practical applications. One more encouraging feature of Skyrmionic motion as observed is that the topological protection allows for Skyrmions to move around defects without loss in velocity or compromising the skyrmion structure.

Increasing the speed of Skyrmionic motion is crucial for racetrack memory applications.

Chapter 3

Experimental Methods

3.1 Brillouin Light Scattering Spectroscopy

[61]Brillouin Light Scattering spectroscopy is an inelastic light scattering technique sensitive to wavelike excitations in matter which are in the GHz frequency range. The light interacts with modulations in the dielectric constant. The two main excitations probed with this technique are phonons which relate to the dielectric constant via the Pockels coefficients and magnons which relate to the dielectric constant via the spin orbit interaction. The polarization induced by light impingent on a material is given by:

$$P(r,t) = \epsilon_0 \ddot{\chi} E_i(r,t) \tag{3.1}$$

where the susceptibility is related to the dielectric function via $\epsilon_0(\ddot{I}+\ddot{\chi}) = \ddot{\epsilon}$Therefore the scattered light must follow the following relation

$$(\Delta^2 + k_s^2)E_s(r,t) = -\frac{\omega_s}{\epsilon_0 c^2} P(r,\omega_s) \tag{3.2}$$

so if we consider, as discussed before, an modulated dielectric function we can examine the effect on the scattered light. Since we are interested in wavelike excitations in

naturally follows that we can write the dielectric function as the sum of an isotropic term constant in time and a fluctuating term given by

$$\ddot{\epsilon}(w,k) = \ddot{\epsilon}_r + \delta\ddot{\epsilon} sin(\omega t - k \cdot r + \phi) \tag{3.3}$$

Given an incoming beam of light with $E_i(r,t) = E_i sin(\omega_i t - k_i \cdot r + \phi)$ the scatterd light will split into three separate beams

$$\begin{aligned} E_{Elastic} &\propto E_i sin(\omega_i - k_i \cdot r) \\ E_{Stokes} &\propto E_i sin((\omega_i - \omega)t - (k_i - k) \cdot r) \\ E_{AntiStokes} &\propto E_i sin((\omega_i + \omega)t - (k_i + k) \cdot r) \end{aligned} \tag{3.4}$$

The beams with shifted frequency result from inelastic scattering and carry information about the excitations being studied. The overall process satisfies momentum and energy conservation

$$\omega_s = \omega_i \pm \omega \tag{3.5}$$

$$k_s = k_i \pm k \tag{3.6}$$

the plus sign corresponds to the absorption of a phonon by the incoming light and is known as the Anti-Stokes process, whereas the negative sign corresponds to the creation of a phonon and is known as the Stokes process. The historical reason for this is that when Stokes performed the experiment he did so at a temperature unsuited for high phonon populations which lead him to only observe the downshifted line. The central peak is known as the Raman peak. The three peaks can be seen in figure 1.

When scattering from opaque materials, the light intensity decays as it penetrates into the material and only material within the penetration depth is probed. A further consequence is that the momentum in that direction is no longer con-

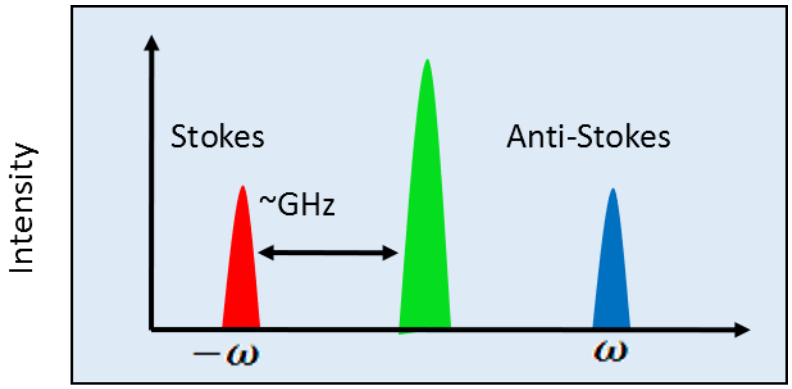

Figure 3.1: Sketch of the BLS spectrum. The left and right peaks are known as the Stokes and Anti-Stokes peaks respectively while the middle peak is known as the Raman peak.

served due to the decay in intensity. Therefore only the in plane component of the momentum is now being conserved.

The first case we can analyze is scattering from phonons. The absorption from the opacity leads to the following relation for the momenta

$$K_s - K_i = k' + ik'' \tag{3.7}$$

In the simplified case of normal incidence we can take k as k_z and we can write the intensity of the scattered light as

$$I = \frac{i}{2} e_i \delta_{q_x,0} \delta_{q_y,0} L_x L_y \int_0^\infty exp[i(q_z - k'_z)z - k''_z z] dz \tag{3.8}$$

The above equation becomes

$$I = \frac{i}{2} e_i \delta_{q_x,0} \delta_{q_y,0} L_x L_y \frac{1}{i(q_z - k'_z) - k''z} \tag{3.9}$$

we can then write the q dependence of the scattered power

$$\frac{dp}{d\Omega} \approx \frac{1}{(q_z - k')^2 - k''^2} \approx \frac{1}{(\frac{q}{k_0} - 2\eta)^2 + (2\kappa)^2} \tag{3.10}$$

where we have used the complex index of refraction defined by

$$n = \eta + i\kappa \tag{3.11}$$

Equation 3.10 tells us that in the presence of optical absorption the phonon wave vector q is no longer uniquely defined. There is instead a range of wave vectors $\Delta_q \approx k''$ centered around $q = k'$ which will all scatter light in the direction k_s. The energy of accoustic phonons is proportional to the wavevector so there will be a broadening of the phonon peak observed in BLS with a peak width defined by

$$\Delta\omega = 4\nu K_0 \kappa \tag{3.12}$$

The peak position is identical for the transparent and opaque case and is given by

$$\omega = 2\eta\nu k_0 \tag{3.13}$$

3.1.1 Polarization of Scattered Light

We have so far looked at what governs the intensity and frequency of the scattered light. Another important consideration is whether or not the polarization of light is affected. In the case of phonons the polarization may or may not be affected depending on the crystal symmetries of the materials and on the specific symmetry groups of the phonon motion. However all magnons modes will create a polarization perpendicular to the incident light when the incident light is linearly polarized.

To see how the polarization of scattered light is affected we first consider the equation of motion of a single electron in: a harmonic potential from being inside a

material, an oscillating electric field from the laser, and a static external magnetic field.

$$m\ddot{r} = -\Delta V = qEe^{-i\omega t} - q\dot{r} \times B \tag{3.14}$$

where r is the displacement of the elctron V is the harmonic potential $V = 1/2mr^2\omega_0^2$, m is the electron mass and q is the electron charge. If we take a steady state solution ($r(t) = r_0 e^{-i\omega t}$) equation 3.14 becomes:

$$m(\omega_0^2 - \omega^2)r_0 - i\omega q r_0 \times B = -qE \tag{3.15}$$

instead of looking at an individual electron's displacement we can look at the macroscopic polarization vector $P = -Nqr_0$ where N is the number of electrons and r_0 is the average electron displacement we can rewrite equation 3.15 in matrix form.

$$\frac{m}{Nq^2}\begin{bmatrix} \omega_0^2 - \omega^2 & i\frac{\omega q}{m}B_z & -i\frac{\omega q}{m}B_y \\ -i\frac{\omega q}{m}B_z & \omega_0^2 - \omega^2 & -i\frac{\omega q}{m}B_x \\ i\frac{\omega q}{m}B_y & i\frac{\omega q}{m}B_x & \omega_0^2 - \omega^2 \end{bmatrix}\begin{pmatrix} P_x \\ P_y \\ P_z \end{pmatrix} = \begin{pmatrix} E_x \\ E_y \\ E_z \end{pmatrix} \tag{3.16}$$

We can find the susceptibility, defined by $P = \overleftrightarrow{\chi}E$, by taking the inverse of equation 3.16. We separate $\overleftrightarrow{\chi}$ into a linear and nonlinear term such that $\overleftrightarrow{\chi} = \overleftrightarrow{\chi}_L + \overleftrightarrow{\chi}_{NL}$

$$\overleftrightarrow{\chi}_L = A(\omega^2 - \omega_0^2)\begin{bmatrix} \omega^2 - \omega_0^2 & -i\frac{\omega q}{m}B_z & i\frac{\omega q}{m}B_y \\ i\frac{\omega q}{m}B_z & \omega^2 - \omega_0^2 & -i\frac{\omega q}{m}B_x \\ -i\frac{\omega q}{m}B & i\frac{\omega q}{m}B_x & \omega^2 - \omega_0^2 \end{bmatrix} \tag{3.17}$$

and

$$\overleftrightarrow{\chi}_{NL} = A(\frac{\omega q}{m})^2\begin{bmatrix} -B_x^2 & B_xB_y & B_xB_z \\ B_xB_y & -B_y^2 & -B_yB_z \\ B_xB_z & -B_yB_z & -B_z^2 \end{bmatrix} \tag{3.18}$$

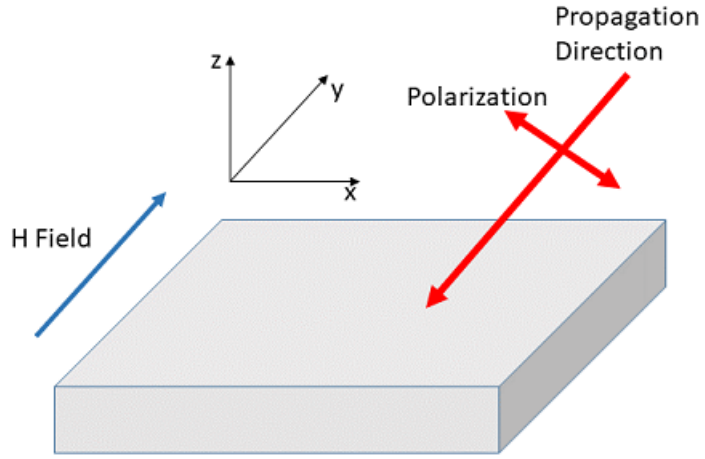

Figure 3.2: Schematic of the relevant directions for determining polarization. Incident light is P-polarized and the magnetic field is perpendicular to the plane of incidence

where

$$A = -\frac{Nq^2}{m(\omega^2 - \omega_0^2)[(\omega^2 - \omega_0^2)^2 - (\frac{\omega q|B|}{m})^2]} \tag{3.19}$$

Ignoring the nonlinear contributions the polarization becomes

$$P_L = -\overleftrightarrow{\chi}_L E = A(\omega^2 - \omega_0^2) \begin{bmatrix} \omega^2 - \omega_0^2 E_x & -i\frac{\omega q}{m} B_z E_y & i\frac{\omega q}{m} B_y E_z \\ i\frac{\omega q}{m} B_z E_x & \omega^2 - \omega_0^2 E_y & -i\frac{\omega q}{m} B_x E_z \\ -i\frac{\omega q}{m} B_y E_x & i\frac{\omega q}{m} B_x E_y & \omega^2 - \omega_0^2 E_z \end{bmatrix} \tag{3.20}$$

equation 3.20 simplifies to

$$P_L = A(\omega^2 - \omega_0^2)[(\omega^2 - \omega_0^2)E + i\frac{\omega q}{m} B \times E] \tag{3.21}$$

Equation 3.21 shows that in addition to a polarization parallel to the incident polarization, a polarization perpendicular to the incident field can arise in the presence of a nonzero magnetic field. If we consider the case of an electric field polarized in the plane of the material The incident electric field oscillates in the xz plane such that

$E = E_x\hat{x} + E_z\hat{z}$. The magnetic field is applied along the y axis. The perpendicular component of the reflected light's polarization is given by:

$$B \times E = -B_y E_z \hat{x} + (B_x E_z - B_z E_x)\hat{y} + B_y E_x \hat{z} \tag{3.22}$$

Since the incident light was oscillating in the xz plane, the perpendicular component of the polarization is the y direction. This y component is given by $(B_x Ez - B_z E_x)$ meaning that it is created by the small oscillaitons in the magnetic field in the x and z direction. These oscillations come from the magnetic excitations we study and as such collecting this small perpendicular component of the scattered light we collect information about the magnetic oscillations.

The method of collecting scattered light which is perpendicular to the incident light has the added advantage of screening the large intensity elastically scattered light. A lower overall intensity hitting the detector protects it from damage and enables longer duration scans and the use of highly sensitive detectors which might otherwise be damaged. In our setup we use a Glan-Laser Polarizer. This is a crystal which will transmit linearly polarized light along an axis and reflect the perpendicular light out the side. By changins the direction in which we enter the crystal we change which side the perpendicular light exits. By placing our collection optics and detector on the side where light reflected off of the sample with the perpendicular polarization exits we collect our signal and screen out the elastically scattered light.

3.1.2 Analyzing Scattered Light

There are actually several techniques which take advantage of the inelastic scattering of light. The main difference between these techniques is what kind of instrumentation is used to separate the shifted light from the elastically scattered light. For example Raman spectroscopy uses a diffraction grating, whereas Brillouin light scat-

tering uses a Fabry-Perot interferometer. The reason for this is that the diffraction grating can only detect frequency shifts down to about $5cm^{-2}$ whereas the interferometer can resolve even smaller shifts.

A basic Fabry-Perot interferometer primarily consists of a cavity which consists of two closely spaced mirrors which allow roughly 90-98% of light to pass through. The reflectance needs to be less than one, so that light can enter and eventually pass through the cavity. Light can only pass through the cavity when there is constructive interference within the cavity. That is that the optical path length through the cavity must be an integer multiple of the wavelength of the incoming light so that :

$$m\lambda = 2nL$$

where n is the index of refraction of light inside the cavity and L is the length of the cavity. It is therefore possible to scan through possible incoming frequencies by varying the distance between the mirrors, or by varying the index of refraction. In our case it is the mirror spacing which is varied by piezoactuators. The frequency resolution is determined by the finesse of the cavity. The finesse is defined by the following expression, which describes the transmission lineshape given by the Airy distribution.

$$A(\sigma) = (\frac{T}{1-R})^2 \frac{1}{1 + (\frac{2F}{\pi})^2 sin^2(\frac{2\pi nL}{\lambda})} \tag{3.23}$$

where F is the Finesse, T and R are the transmission and reflectivity of the mirrors respectively, and λ is the wavelength if the light. The finesse is given by the free spectral range divided by the full width at half maximum of the above lineshape. The free spectral range is the distance that we must scan to get from one mode of the cavity to the next. Therefore the free spectral range is what sets the frequency resolution, and thus a higher finesse yields better resolution. The total finesse is

given by:

$$\frac{1}{F^2} = \frac{1}{F_f^2} + \frac{1}{F_r^2} + \frac{1}{F_p^2} \tag{3.24}$$

where F_f is the flatness finesse, F_R is the reflectivity finesse and F_p is the pinhole finesse. The flatness finesse is set by the flatness of the mirror and is given by:

$$F_f = \frac{M}{2} \tag{3.25}$$

where $\frac{1}{M}$ is the deviation away from true flatness of the mirror as multiple of the wavelength. A non-flat mirror leads to an ill defined length of the cavity which broadens the lineshape. The reflectivety finesse is greater the closer the reflectivity is to one. However for practical purposes we cannot have it be too close to one so that light still passes through the cavity. The reflectivity finesse is given by:

$$F_m = \frac{\pi\sqrt{R}}{1-R} \tag{3.26}$$

Finally the pinhole finesse must be taken into account because the light incoming to the cavity will have a certain width dependent on the focus and the size of the pinhole. The width of the incoming lineshape will affect the width of the transmission lineshape. This finesse is given by:

$$F_p = \frac{4\lambda f^2}{D^2 L} \tag{3.27}$$

where f is the focal length of the focusing lens and D is the diameter of the pinhole. Usually the finesse is set by the mirror flatness and reflectivity and the limiting value is usually around 100. Another factor in determining the performance of an interferometer is the contrast ratio which is defined as the ratio of the maximum of the Airy function to the minimum. This ratio is determined by the finesse and is

given by:

$$C = 1 + \frac{4F^2}{\pi^2} \tag{3.28}$$

clearly a higher contrast ratio is desired as it improves the signal to noise ratio. For a typical cavity the contrast ratio can only be as high as 10^4. This is sufficient when the ratio between the signal and the scattered light is greater than 10^{-4}. This is not the case for opaque or reflective surfaces, so the contrast must be improved. This is done by passing the light through the cavity several times. The contrast will then be C^p where p is the number of passes. While this improves the contrast ratio it does nothing to affect the finesse or change the free spectral range.

In order to extend the free spectral range one can add a second cavity to the interferometer with its own distinct spacing. Such a device is known as a Sandercock interferometer. The first cavity will only transmit light satisfying the condition:

$$\lambda_1 = \frac{2L_1}{m_1} \tag{3.29}$$

where m_1 is an integer and L_1 is the length of cavity 1. The second cavity will only transmit light with

$$\lambda_2 = \frac{2L_2}{m_2} \tag{3.30}$$

where m_2 is an integer and L_2 is the length of cavity 2. The only way we can have light pass through both cavities is if $\lambda_1 = \lambda_2$ and as such the sensitivity to frequency is greatly improved. We can see in figure 3.3 that the higher order transmissions are suppressed extending the region where we can see a signal. The difficulty in creating such an arrangement is that the scans of the two mirrors must be synchronized. A scan over the desired frequencies must increment the length changes δL_1, δL_2 such that

$$\frac{\delta L_1}{\delta L_2} = \frac{L_1}{L_2} \tag{3.31}$$

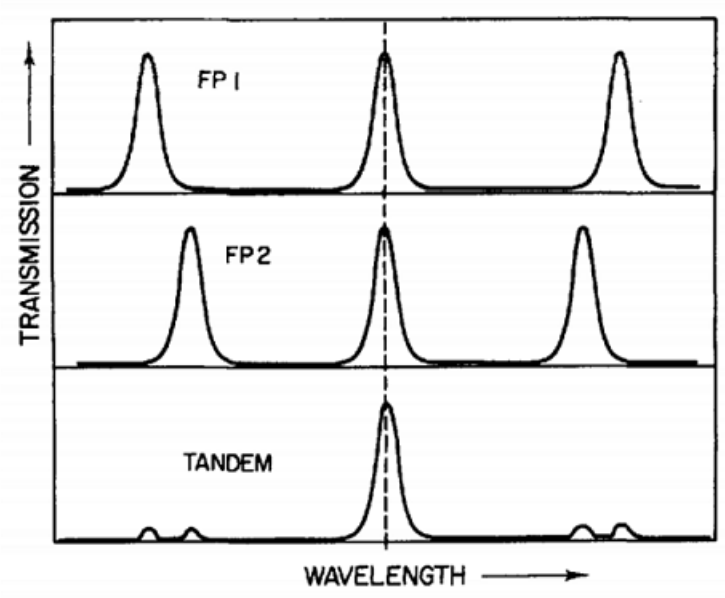

Figure 3.3: Higher order transmission is suppressed in the tandem arrangement

The initial way this was done was by scanning the pressure inside the interferometer. This changes the index of refraction which corresponds to a change in effective path length. Since both cavities have the same change in pressure the ratio is maintained. The problem with that method is that it limits the range of effective path lengths we can scan over. Instead we have both cavities sharing a common translation stage with one mirror from each cavity resting on this stage. As seen in figure the other mirrors are not at the same angle relative to the stage. Here we have $L_1 = L_2 cos(\alpha)$ and as such the condition of equation 3.31 is always satisfied since by moving in the direction indicated in the figure3.4 we are scanning over L_1. Using a single translation stage has a number of advantages.

1. The scan is tilt free

2. The scan is linear

3. The mirror spacing can be changed without loss of alignment

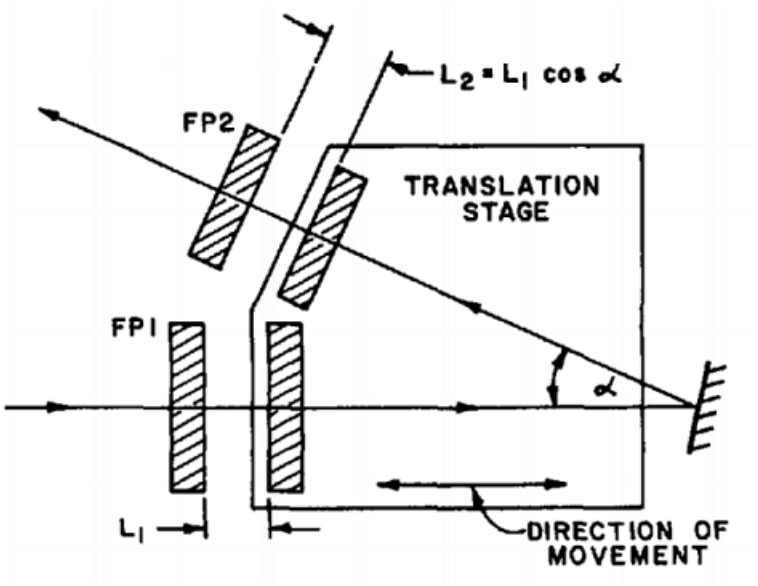

Figure 3.4: Using a single translation stage ensures the scans over the two cavities are properly synchronized

4. The two cavities share the same environment (same index of refraction)

5. The setup is stable against thermal fluctuations

In order to improve contrast and free spectral range it is possible to pass the light through the tandem cavities multiple times. In the case of our setup light is passed 3 times through the tandem cavities for a total of 6 passes through a cavity.

Due to the sensitive nature of the constructive interference which allows light to pass through the cavities small thermal fluctuations are enough to disrupt the experiment entirely within minutes. The way this is dealt with is with an active alignment procedure.

It is only possible to check and maintain the alignment by passing a laser through the cavities, as such when the experiment is not running alignment will be lost. Therefore it is necessary to have a procedure to recover alignment before an experiment is started. A reference beam of 532nm light is sent into the interferom-

eter which is set to alignment mode. This mode shifts the mirrors such that light reflected away from the cavities is sent to the detector as opposed the measurement mode where the transmitted light is sent to the detector. In this mode there are 6 parameters which can be varied to recover alignment. Each mirror can rotate about a vertical and horizontal axis. The rotation about each axis is varied either manually using a controller or through the software's auto-alignment program. When the cavities are out of alignment a flat background will be seen by the detector. Once the cavities enter alignment there will be two dips in the signal corresponding to light being transmitted by the cavities as opposed to reflected. Once each dip is maximized we can say that the cavities are individually in alignment. The next parameter is the angle between the cavities which controls the relative spacing. Changing this will move the two dips seen on the spectrum and once the dips overlap then the cavities will be in alignment with each other. The final parameter is the overall spacing which will shift the dip up and down in frequency. Once the dip is lined up with the zero frequency we can say the cavities are aligned and properly calibrated since 532nm light is now being properly transmitted.

Next the interferometer is switched back to transmission mode, which is the mode we perform experiments in. Once in this mode the computer will make micro-adjustments to the 6 parameter to fine tune and optimize transmission. Once the peak in the transmission is maximized we can begin our experiments. The reference beam is not blocked during measurements allowing the dynamic alignment process to continue and making sure alignment is maintained throughout the experiment.

A further note about alignment is that the procedure described above works well for relatively small changes in alignment. In some cases the shift is larger than the range of the piezo actuators which control the processes described. The first method of coarse alignment is to make larger shifts in the tilts of the mirrors using switches on the interferometer itself. This can get you back in the range of the piezo

stages and allow for alignment. If alignment is lost beyond this range it becomes necessary to open the interferometer and refer to its manual in order to reproduce the alignment procedure used when first setting up the cavities. The overall cavity spacing can also be adjusted manually in order to change the free spectral range and control the range of frequencies being detected. A larger overall spacing allows for more precise measurements but reduces the available frequency range. Choosing the right spacing becomes a balancing act between the requirements of frequency resolution and frequency range.

3.1.3 DMI Measurement

[48]BLS can be used to probe the strength of the Dzaloshinskii-Moriya interaction by accessing its effect on the dispersion of spin waves which was discussed previously. In order to access this dispersion we need some way to control or measure the wavelength of the probed excitations. This is done by carefully considering energy and momentum conservation of the scattered light.

If light scatters of a material such that the reflected angle is not equal to the incident angle then there must have been a change of momentum. The magnitude of this change is given by the following relation:

$$\frac{4\pi}{\lambda} Sin\theta = K \tag{3.32}$$

. Experimentally this corresponds to changing the angle of incidence of the light on the material without changing the collection optics which are aligned for normal incidence. This is done in our lab by tilting the sample without changing any of the optics which are optimized for normal incidence. Therefore any light collected must have scattered in this non-momentum conserving fashion.

There are two scattering processes which result in a change of k in the scattered light: Absorption of a magnon with momentum k or creation a magnon with

momentum -k. Energetically the first process increases the scattered energy, and therefore frequency, of the scattered light and the second represents a decrease corresponding to the Anti-Stokes and Stokes processes respectively. Any asymmetry between the frequencies of the two peaks therefore corresponds to an asymmetry in dispersion. This asymmetry can either be from DMI or from non-reciprocity. The latter case will be discussed in the next section and the former will be further analyzed in this section.

In order to measure DMI we first take a series of BLS spectra for a number of incident angles typically ranging from 0-45 degrees. Higher angles of incidence require greater changes in momenta to occur and are as such less likely and less efficiently collected. We can compensate for this by adjusting integration time but there are practical limits to the integration time as well. These limits are primarily alignment of the cavity being maintained and stability of the laser which is probing the material. These factors are what set the upper limit of our collected angle. The interferometer can be reliably stable for 5 hours at a time so once data taking exceeds this limit we know the maximum angle has been rached. The maximum angle can be as high as 55 degrees and as low as 20 depending on the material. A larger range of measurable angles allows for a better determination of D. In figure 3.5 we can see a sample spectrum for normal incidence and for 32 degrees. Note that the height of the peaks is highly asymmetric in the high k case.

This is not related to the population of the modes but rather a consequence of nonreciprocity. Modes with opposite k propagate on opposite surfaces and as such the mode propagating on the bottom surface is less efficiently probed since our laser needs to go through the thickness of the material. We verify this interpretation of the data by noting that reversing the magnetic field reverses which k values are associated to which surface meaning that we should see the asymmetry in intensity flip as well which we can see in figure 3.5 where the stokes is now stronger.

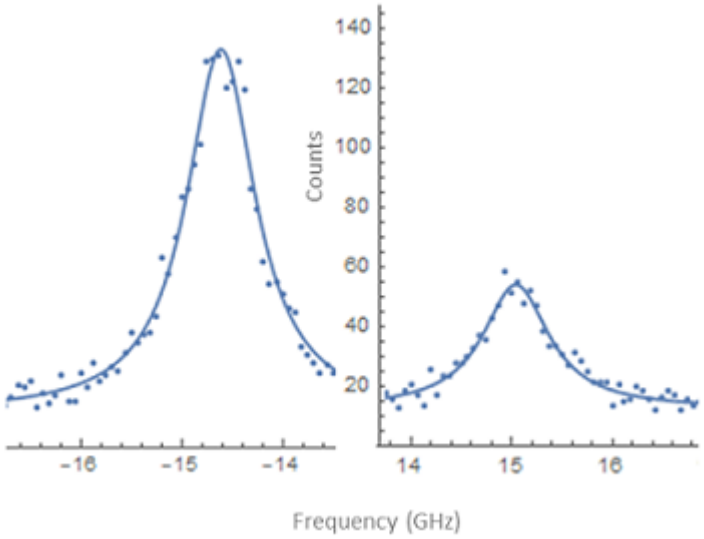

Figure 3.5: (a) (b) Stokes and Anti-Stokes peaks respectively for normal incidence on CoFeB/Pt. There is minimal difference between the heights of the peaks. (c) (d) Stokes and Anti-Stokes peaks respectively for 32 degree incidence on CoFeB/Pt.

Once the spectra are all taken each peak is fit to a Lorentzian lineshape given by:

$$F = \frac{I\gamma}{(\omega - \omega_0)^2 + \gamma^2} \tag{3.33}$$

where I gives the integrated intensity, γ gives the linewidth and ω_0 gives the central frequency.These three parameters are always extracted although in the case of DMI only the central frequency is needed. Note that the Stokes and Anti-Stokes peaks are always fit separately and independently. We can see an example of this by looking at the fit to the Stokes peak of the normal incidence case of figure 3.5 and verify that the Lorentzian lineshape fits the data well

Once the frequencies of the Stokes and Anti-Stokes peaks are found the anti-symmetric component is extracted by simple subtraction.

$$f_{as} = |f(k)| - |f(-k)| \tag{3.34}$$

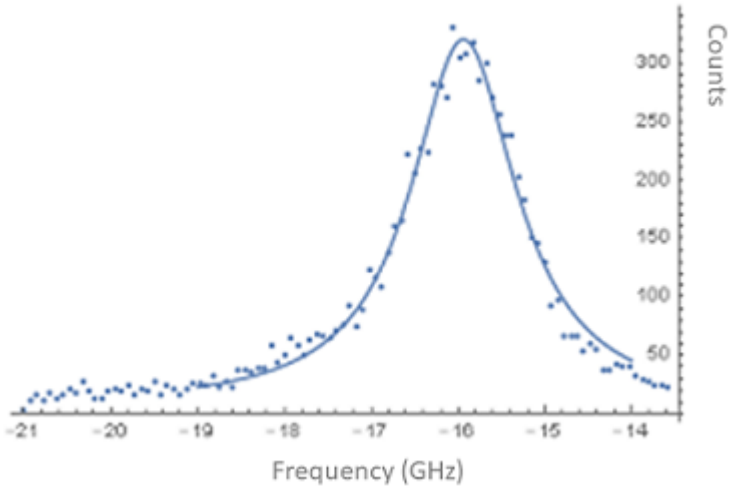

Figure 3.6: Lorentzian lineshape fit to the Stokes peak of normally incident light on CoFeB/Pt

this anti-symmetric frequency is often known as the dmi frequency shift f_{dmi}. By analyzing eq 2.82 which gives the full dispersion for surface spin waves in the presence of DMI and noticing that when we take the anti-symmetric frequency shift we are left with

$$f_{dmi} = sgn(M_s)\frac{\gamma}{\pi M_s}Dk \tag{3.35}$$

where γ is the gyromagnetic ratio, M_s is the saturation magnetization and D gives the strength of DMI. We see from this that we expect the DMI induced shift should be linear with respect to k. We also expect that for k = 0 there should be no asymmetric shift. In addition the direction of the slope gives the sign of the DMI. We see in figure 3.6 for both positive and negative fields the shift is roughly linear and opposite in slope as we expect. However, neither the positive nor the negative field have zero shift at k = 0. The offset seen comes from intrinsic shifts due to the experimental setup. Another issue is that there are deviations from linearity which are due to random error.

We can fix both of these issues by taking the average contribution of the

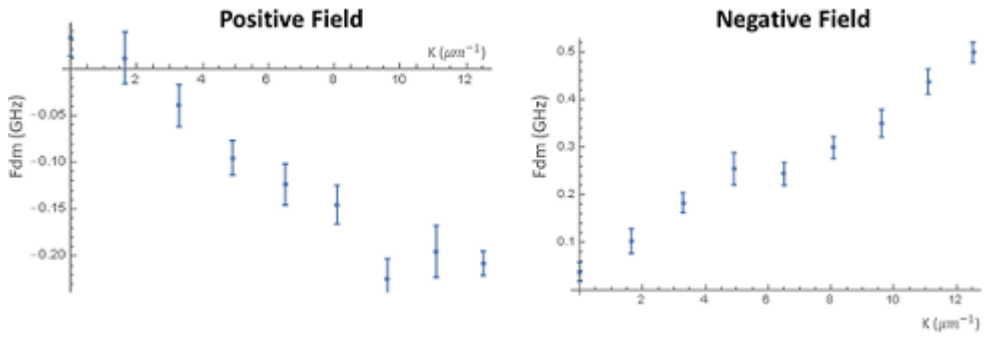

Figure 3.7: DMI induced frequency shift for opposite field directions.

positive and negative field we get a more accurate representation of f_{dmi}.

$$f_{dmi} = \frac{((f(-k,+H) - f(k,+H)) - (f(-k,-H) - f(k),+H)))}{2} \tag{3.36}$$

Looking at this new f_{dmi} we see that it now properly passes through zero and is well fit by a line. From the slope of this line we were able to determine a dmi constant of around -525 $\frac{\mu J}{m^2}$

It is important to note that there are two distinct BLS techniques which can be used in our lab. Micro and Macro BLS differ by the spotsize of the laser light on the sample. Following is a brief discussion of the advantages of each technique.

Micro-BLS uses a microscope objective to achieve a spotsize of approximately one micron on the sample. This allows for the study of smaller magnetic structures. However, the small spot size limits the amount of laser power that can be sent to the sample for fear of damaging the sample. Additionally, by achieving a large spatial resolution, momentum resolution is lost. Micro-BLS is most suitable for samples with strong magnetic signal and for samples with small magnetic structures.

Macro BLS doesn't focus the laser light onto the sample and has a spot size of 10s of microns. This allows for larger laser power to be used and we retain some angular resolution. Macro BLS is most useful for samples with weaker magnetic

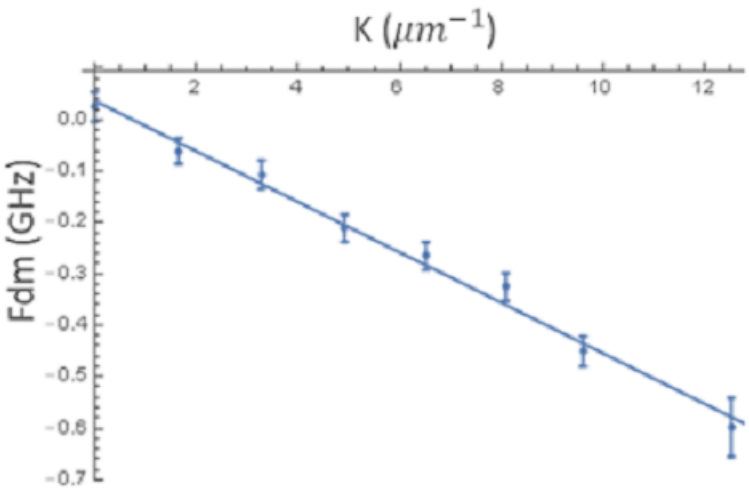

Figure 3.8: DMI induced frequency shift for average of positive and negative fields

signal or experiments which require a well defined momentum of the incoming laser light.

Anisotropy and Exchange

For normal incidence (k = 0) equation2.82 simplifies to:

$$f = \frac{\gamma}{2\pi}\sqrt{H(H + 4\pi M_e f f)} \tag{3.37}$$

meaning that by taking a series of measurements with normal incidence and varying the external field we can find the effective magnetization, which contains information about the anisotropy:

$$4\pi M_e f f = 4\pi M_s - \frac{2k_\perp}{M_s} \tag{3.38}$$

we therefore use the μBLS setup which allows magnetic field control and take a series of measurements at varying field. We take a full spectrum focusing on the Anti-Stokes peak, which typically has a stronger signal in our setup, at each magnetic field. The raw spectra are all fit to Lorentzian lineshapes as previously described

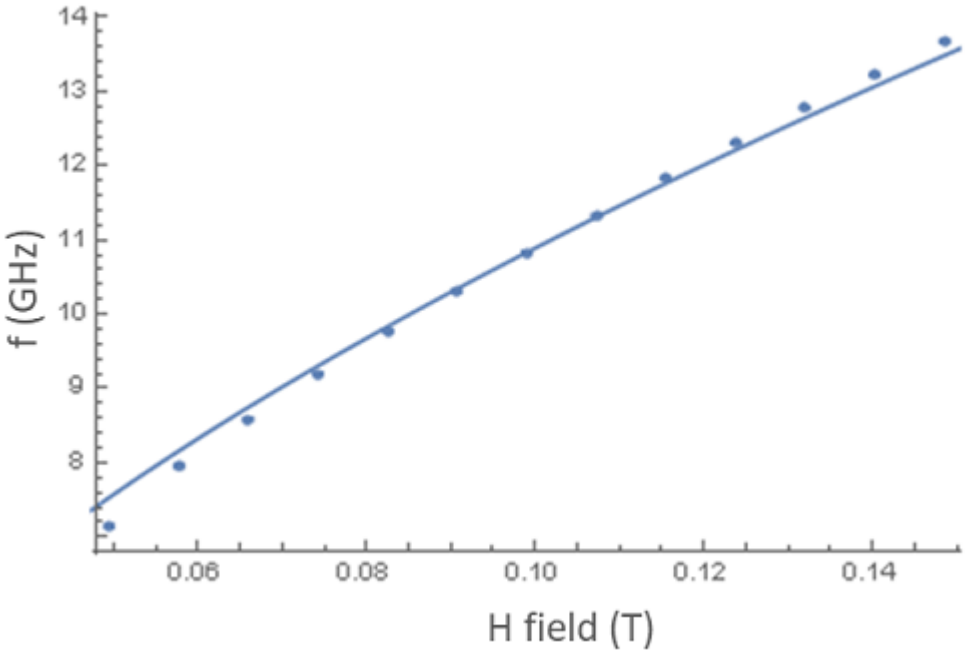

Figure 3.9: Frequency as a function of applied field. Solid line is fit to equation 3.38

and the peak frequencies are extracted. The frequencies as a funciton of applied field are then fit to eq. 3.38. The result can be seen in figure 3.38 M_eff is extracted from the fit since it is one of the fit parameters which in turn allows us to determine the anisotropy

Once anisotropy is extracted it can be used to determine exchange and the non-reciprocity induced frequency shift. In addition to this the strength of anisotropy is an important parameter to determine since it determines a host of magnetic properties such as easy axis direction and Skyrmion size.

Determining Exchange stiffness

Using the asymmetric shift in frequency dispersion we were able to determine the asymmetric exchange also known as the Dzyaloshinskii-Moriya interaction. It stands

to reason then that the symmetric shift in frequency dispersion should yield information about the symmetric or Heisenberg exchange.

This intuition is correct although the functional dependence on k is more complicated. It is found by taking the dispersion from eqx. as we did when finding D but instead of taking the difference in frequency between the Stokes and Anti-Stokes we take the average as follows:

$$f_s = (|f(k)| + |f(-k)|)/2 \tag{3.39}$$

The result of this using eq2.82 is

$$\omega_s = \gamma\sqrt{(H_{eff} + \frac{2A}{M_s}k^2 + 4\pi M_s(1 - \xi(kL)) - \frac{2K_\perp}{M_s})(H_{eff} + \frac{2A}{M_s}k^2 + 4\pi M_s\xi(kL))} \tag{3.40}$$

where A is the exchange stiffness which will emerge as a fitting parameter, M_s is the saturation magnetization, H_eff is the magnetic field felt by the system, $K_\perp$ is the magnetic anisotropy and ξ is defined in eq 3.43. We know can take the same raw data used in a previous section and fit the above equation to it. The result of this can be seen in figure 3.10. From the fit equation we can extract a value for exchange stiffness. The ability to characterize a wide range of magnetic properties such as exchange, DMI and anisotropy using a single technique is quite powerful and can allow for a consistent characterization of magnetic materials. This consistent characterization is key to making meaningful comparisons of strengths of different effects. We can also track how these parameters are related to each other. Of course comparisons are still possible when using different techniques to measure different properties. However the issue is that different techniques can be sensitive to different length scales or different perturbations. This muddies comparisons and makes it more difficult to understand the relationships between these properties.

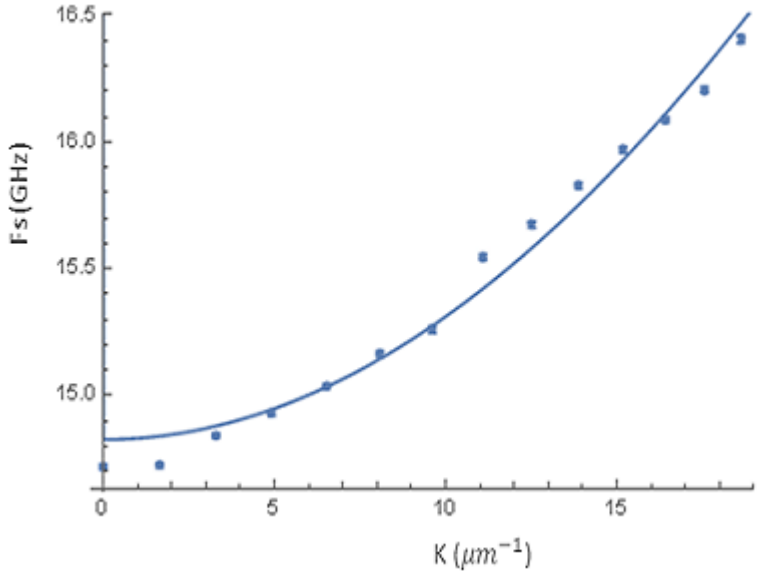

Figure 3.10: Symmetric frequency shift as a function of k along with fit

NonReciprocity Induced Frequency Shift

DMI isn't the only thing which can cause a frequency shift which is antisymmetric in k. Damon-Eschbach modes with opposite k vectors will travel on opposite surfaces. In the case of a thin film magnetized in the +z (-z) direction modes with k > 0 will be localized to the top (bottom) interface. If there is anisotropy in the material, the effective magnetic field at each surface will differ, causing a shift in the frequency.

We can calculate this shift in frequency using the fact that in the long wavelength limit the modes will decay exponentially away from their respective surfaces into the film thickness with a decay length of $\frac{1}{k}$. The anisotropy in the material is assumed to come from the Pt interface as seen in Nembach et al.[48] Therefore the anisotropy field is assumed to be localized within the first monolayer of magnetic material. To properly model this effect the extent of the anisotropy field is chosen to be 0.5Åwhich is smaller than the size of a single layer. This is because the effect is

interfacial and therefore it's length scale is set by the interatomic bonds between the first magnetic layer and the Platinum. The magnitude of the interfacial anisotropy field is found using the method described in section 2.3. The effective field from the anisotropy on each of the modes is given by:

$$H_k^{eff_\pm} = \frac{\int H_k^{int} m^\pm(t)dt}{\int m^\pm(t)dt} \tag{3.41}$$

Once the effective anisotropy field is found the frequency shift induced by nonreciprocity is calculated using the dispersion

$$\frac{\gamma}{2\pi}\sqrt{(H + \frac{2A}{M_s}k^2 + 4\pi M_s(1-\xi(kL)) - H^{eff+}(k))(H + \frac{2A}{M_s}k^2 + 4\pi M_s\xi(kL))} \\ - \frac{\gamma}{2\pi}\sqrt{(H + \frac{2A}{M_s}k^2 + 4\pi M_s(1-\xi(kL)) - H^{eff-}(k))(H - \frac{2A}{M_s}k^2 + 4\pi M_s\xi(kL))} \tag{3.42}$$

where A is the exchange stiffness as determined by the methods in sectionx, H_eff is the effective external field applied to the sample, M_s is the saturation magnetization which must be measured using VSM or SQUID as described in sectionx, γ is the gyromagnetic ratio of the electron which is a constant ($\approx 1.76X10^{11}\frac{Rad}{s\cdot T}$) and $\xi(kL)$ is defined as:

$$\xi(kL) = 1 - \frac{1-e^{-kL}}{kL} \tag{3.43}$$

An example of the results can be seen in figure 3.11 where the frequency shift is being calculated for Co/Pt. The shift induced by nonreciprocity is 2 orders of magnitude smaller than the dmi induced shift in this case. This is typical for most materials and the DMI induced shift is almost always dominant. This shift is strongly thickness dependent since we are looking at a shift between top and bottom surfaces where one surface is affected by an interfacial field. Since DMI in these samples comes from the

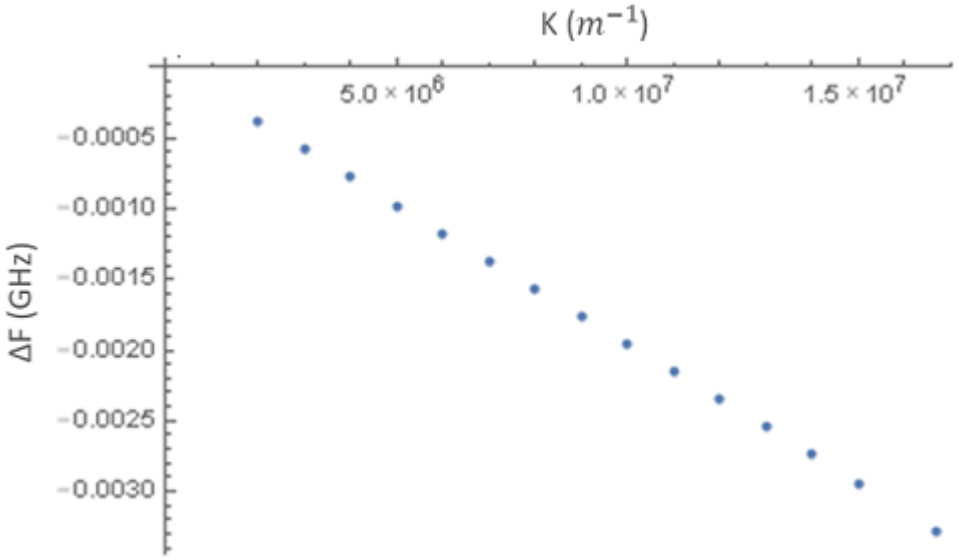

Figure 3.11: Non-reciprocity induced frequency shift for Co/Pt.

interface it's effect is weakened when the sample thickness increases. Therefore thick samples are more heavily influenced by non-reciprocity. The strength of magnetic anisotropy also influences the importance of non-reciprocity where materials with stronger anisotropy will be more affected by nonreciprocity.

3.2 Techniques for Measuring DMI

Characterizing the strength of DMI in material systems is crucial for designing devices as well as gaining a better understanding of the effect. This section will detail different measurement techniques explaining how they work to determining the strength of DMI as well as some strengths and weaknesses of each techniques.

A first method of using MOKE to measure DMI is found in Shahbazi et. al. [62]. Domain walls will move in the presence of a magnetic field. In order to move a domain wall an energy barrier must be overcome known as the pinning barrier. For strong fields above the so-called depinning field the energy to overcome the barrier

comes from the field itself. Howver even below this field there can be domain wall motion when $T \neq 0$ and thermal excitations assist the field in moving the domain wall. The motion in this regime, known as the creep regime, is slower and can be affected by the presence of DMI. MOKE can be used to determine this velocity by taking a static MOKE image of the domain structure, pulsing a magnetic field for a fixed duration and imaging the field structure with MOKE again. By dividing the distance travelled by the wall by the pulse length a domain wall velocity can be determined.

The domain wall velocity in the creep regime is modeled by:

$$v = v_0 exp(-\zeta H_{OP}^{-\mu}) \tag{3.44}$$

where, H_{OP} is the out of plane component of the applied field, v_0 is a characteristic velocity set by the material, μ is the creep scaling exponent which is 1/4 and ζ is a scaling constant dependent on the applied field as follows:

$$\zeta = \zeta_0 [\sigma(H_{IP})/\sigma(0)]^{1/4} \tag{3.45}$$

ζ_0 is a scaling constant and

$$\sigma(H_{IP}) = \sigma_0 + 2\Delta K_D - \pi \Delta M_S |H_{IP} + H_{DMI}| \tag{3.46}$$

is the domain wall energy density with $\Delta = \sqrt{A/K_{eff}}$ is the domain wall width, M_S is the saturation magnetization, H_{IP} is the in plane component of the applied field and H_{DMI} is the effective field created by the DMI.

From the above we can see that there will be a minimum in the domain wall velocity when $H_{IP} = -H_{DMI}$ and so by varying the strength of the pulsed magnetic field and measuring velocity we can find the strength of DMI. We relate the effective

field to D using

$$D = \mu_0 H_{DMI} M_S \Delta \tag{3.47}$$

This technique is not fully independent as it relies on an independent measurement of M_S. The creep regime of Domain wall motion relies on thermally activated jumps between pinning sites which are typically around 5-10nm apart. As such the DMI probed is on a very local scale.

One limitation of the method presented above is that in cases where the DMI is strong H_{DMI} may become too large for practical experimental capabilities to be able to produce a matching H_{IP} or alternatively we may be pushed out of the creep regime. A proposed solution is to place the domain wall at an angle θ with the in plane component of the magnetic field. This method comes from kim et. Al. [63]

The domain wall energy becomes

$$\sigma_0 + 2\Delta K_D - \pi \Delta M_S H_{IP} cos(\theta) + H_{DMI} \tag{3.48}$$

The condition for minimizing domain wall velocity becomes:

$$H_{IP} = (\pm H_k sin\theta - H_{DMI}) cos\theta \tag{3.49}$$

where $H_k = 4K/M_S$ is an effective field from the domain wall anisotropy and is typically small. Note that in the case $\theta = 0$ we recover $H_{IP} = -H_{DMI}$ which was our previous condition.

Increasing the angle θ lowers the required field to reach minimum domain wall velocity and thus a larger range of materials can be studied without the need for potentially costly upgrades to an experimental system. There are other advantages to lowering the required field for experiments. Large fields can induce a magnetic moment in the optical setup which will affect mechanical stability, magneto-optical effects can change the properties of the objective lens and the large currents required

to produce the field will induce significant Joule heating in the elecromagnets coils.

The techniques described in this section have so far all relied on static MOKE. However, time resolved MOKE can also be used to measure DMI as seen in Korner et. Al[64].

The technique requires an antenna to be patterned on the sample. Then a microwave oscillation at a fixed frequency is sent into the antenna. This excitation will create spin waves propagating on either side of the antenna. The spin waves on either side of the antenna will have k vectors of opposite sign.

The magnitude of the k vector is determined by measuring the MOKE signal at different points moving away from the antenna. The key to retaining the phase information required is that the tr MOKE signal must be phase locked to the microwave signal sent through the antenna. When this is the case the signal strength as a function of distance from the antenna will be a damped sign. From the spatial period of the sine the magnitude of k can be extracted. The decay length is also measured incidentally by this technique.

To obtain a value of D one simply tunes the excitation frequency and looks for asymmetry in the magnitude of k for the two counterpropagating spin waves generated by the microwave. Equation 2.86 still relates frequency to k vector and a value for d can be extracted by considering the terms asymmetric in frequency. To ensure the asymmetry measured originates from DMI it is necessary to reverse the applied field and verify that the asymmetry is also reversed.

This method is extremely analogous to using BLS with the difference being that in BLS k is fixed and frequency is measured whereas this tr-MOKE technique fixes frequency and measures k.

An advantage of the tr-MOKE technique is that it can be used for materials which do not have strong thermal magnons since the magnons are being generated. Challenges for this method are the need for additional fabrication, the need for

optical access to the material, the need for a supporting measurement of saturation magnetization and the fact that phase locking the MOKE signal to the microwave excitation is very experimentally challenging.

Nitrogen Vacancy centers in diamonds have been shown to be extremely sensitive to small magnetic fields enabling the possibility of single spin sensing. By placing an NV center onto an AFM tip we enable sensing with atomic resolution.

The measurement scheme detailed in Gross et. Al. [65] for using NV centers to measure DMI is to measure stray fields from domain walls. Domain walls can be characterized by the angle ψ between the in plane DW magnetization and the axis perpendicular to the DW (here defined as the x axis).

Bloch domain walls have $\psi = \pm\pi/2$ and the magnetization rotates as a spiral when crossing the DW. Neel type domain walls on the other hand have $\psi = 0 or \pi$ causing a cycloidal rotation of the magnetization. The two possible values of ψ gives the chirality of the DW. Whether Neel or Bloch type walls will form is dependent on the strength of DMI which favors the cycloidal Neel walls. In fact above a critical value of D all walls will be Neel type. The critical value is given by:

$$D_c = 2\mu_0 M_s^2 t ln2/\pi^2 \tag{3.50}$$

where t is the sample thickness and M_s is the saturation magnetization. For $D > D_c$ we have $\psi = 0$ and for $D < D_C$ we have $\psi = \pi$ and walls are of the neel type. For $D << D_c$ we have $\psi = \pm\pi/2$ and Bloch type walls. However in the intermediate regime $D \leq D_c$ the domain wall is a hybrid and $\psi = \pm acos[\frac{D}{D_c}]$. Therefore by measuring ψ we can measure D. ψ is determined by measuring the stray field and using the relation

$$B^{\psi}(x) = B^{\perp}(x) + B^{\parallel}(x) cos\psi \tag{3.51}$$

the left hand side of equation3.51 is the experimentally determined quantity. The

components on the right hand side can be calculated for a point a distance d above the sample:

$$B_x^{\perp}(x) = \frac{\mu_0 M_s t}{\pi} \frac{d}{x^2 + d^2} \tag{3.52}$$

$$B_z^{\perp}(x) = -\frac{\mu_0 M_s t}{\pi} \frac{x}{x^2 + d^2} \tag{3.53}$$

and

$$B_x^{\parallel}(x) = \frac{1}{2} \mu_0 M_s t \frac{x^2 - d^2}{(x^2 + d^2)^2} \tag{3.54}$$

$$B_z^{\parallel}(x) = \mu_0 M_s t \frac{xd}{(x^2 + d^2)^2} \tag{3.55}$$

where $\Delta = \sqrt{A/K_{eff}}$ is the DW width. By measuring the stray field and using the above equations ψ can be extracted and D can be found.

The strength of this method is its ability to sense local variations of D on a small scale. The main weakness is that it can only measure systems with weak D. $D_c = 0.2 mJ/m^2$ is a typical value so only D less than that could be measured by this technique.

Another problem is the need for complementary measurements of M_s and Δ. The former can be measured quite precisely but there are problems for the latter. In particular there doesn't exist a reliable way to measure exchange stiffness in thin films and so Δ cannot be found precisely. This uncertainty accounts for the bulk of the uncertainty in obtained D values using this NV center method.

As seen in Jiang et. Al [66]Lorentz TEM can measure the magnetic state of a sample by detecting a phase shift of the electron wave passing through the sample. Magnetic contrast will only be seen when the objective is out of focus ($\Delta f \neq 0$) and in regions with a nonzero gradient in phase. Bloch Skyrmions can be observed

at normal incidence but Neel Skyrmions do not have a phase gradient. However by tilting the sample magnetic contrast can be obtained and Skyrmions can be observed to nanometer spatial resolution.

The size of the Skyrmion is determined by Lorentz TEM. Micromagnetic simulations are then performed for a wide variety of D values. Typically only a small range of D values will generate Skyrmions of a given size and so D can be determined.

The main downside of this technique is that only the size of the Skyrmion can be determined, not the chirality. As such only the magnitude and not the sign of D can be determined. Additionally, supplementary measurements of both saturation magnetization and anisotropy would be required to find the input parameters for the micromagnetic simulations.

The main advantage of this technique is the direct imaging and resolution of nanometer sized Skyrmions.

In samples lacking lateral inversion symmetry DMI can cause asymmetry in magnetic hysteresis loops. This was first demonstrated by Han et. Al [67]in triangular shaped samples which are of lower symmetry than the usual square or rectangular samples which have two fold lateral symmetry about the z axis perpendicular to the sample.

In such an asymmetric sample, applying a static in plane magnetic field will cause asymmetry in the out of plane hysteresis loop only in samples with nonzero DMI. The DMI acts like an effective field shifting the hysteresis loop in a manner analogous to exchange bias.

Micromagnetic simulations are performed to determine the value of D by finding the value that appropriately replicates the observed shift. To ensure proper determination of D the shift is found for a number of in plane fields and a number of different sample shapes. In the case of a triangle varying the angles is a sufficient

change to the shape.

This technique is static and provides an average DMI for the entire sample. A static technique avoids some of the pitfalls of the more common dynamic techniques which are often muddied by competing effects (e.g. chiral damping for domain wall motion or nonreciprocity for counterpropagating spin waves). In addition by using hysteresis loops saturation magnetization need not be measured independently.

The main challenges are that an independent value of exchange stifness is needed and more importantly, that not all samples can be grown or cut into arbitrary shapes. In particular, devices will typically need their own specific geometry to operate.

[54]Spin Polarized Low Energy Electron Microscopy can distinguish between Neel and Bloch type Domain walls. In particular it can determine the angle between the domain wall magnetization and the normal to the domain wall. This angle characterizes DWs as Neel or Bloch types and can describe intermediate states as well.

D is measured by looking at several samples of different magnetic thicknesses and determining the thickness at which there is a transition between Neel and Bloch walls being stable. From this thickness we can calculate the value of D.

The main advantag of this technique is that the calculation is independent of Anisotropy and Exchange Stiffness removing the need for supplementary measurements. Since SPLEEM is measuring the angle of the domain wall magnetization it is sensitive to chirality and will appropriately determine the sign of D.

The main drawback is that it is unsuitable for a single sample, rather it must be used to characterize material systems since a series of samples with varying thicknesses are required. Therefore this technique cannot be used to characterize a single device.

Chapter 4

Auto-Oscillation in FM/HM Nanowires

4.1 Spin Hall induced auto-oscillations in ultrathin YiG grown on Pt

[1]We experimentally study nanowire shaped spin hall oscillators based on nanometer thick epitaxial films of Yttrium Iron Garnet grown on top of a layer of pt. We show that, although these films are characterized by significantly larger magnetic damping in comparison with films grown directly on Gadolinium Gallium Garnet, they allow one to achieve spin current driven auto-oscillations at comparable current densities, which can be an indication of the transparency of the interface to the spin current. These observations suggest a route for improvement of the flexibility of insulator based spintronic devices and their compatibility with semiconductor technology.

[1]The discussion in this section closely follows that of ref.[37]. Project was suggested by I. Krivorotov, samples were provided by C. Evelt, experimental results were performed by K. Sobotkiewich. Writing by borth C.Evelt and K.Sobotkiewich

4.1.1 Spintronic Devices Driven by Pure Spin Current

Spintronic devices driven by pure spin current have recently become a subject of intense research[5, 68, 69, 70, 71, 72, 73, 74, 75, 36, 6, 7, 28] thanks to their flexible layout which is not restricted by the requirement that the eectrical current pass through the active magnetic layer. This advantage is particularily important for the possibility of implementing spintronic devices based on magnetic insulators such as Yttrium Iron Garnet (YIG) a material known for its unmatched small magnetic damping. Additionally, using magnetic insulators eliminates the shunting of the driving electrical current through the active magnetic layer which is known to be a significant shortcoming of all-metallic spintronic devices[7]. Initially, YIG based spintronics progressed relatively slowly due to the difficulty of preparing high quality nanometer thick YIG films. It is only thanks to recent developments in growth techniques[76, 77, 78, 79, 80, 81] that insulator based spintronic devices have become feasible.

The magnetic damping in YIG films is closely related to their structural properties[76, 77, 78, 79, 80, 81]. Therefor, high quality YIG films are usually grown on Gadollinium Gallium Garnet (GGG) substrates which provide precise lattice matching between the two materials. Using a different substrate than GGG results in a significant increase of the damping constant[82]. This requirement limits the compatibility of YIG with traditional silicon based semiconductor technology. Additionally, it significantly reduces the flexibility of spin current devices using materials with strong spin orbit interaction (Pt e.g) for generation of spin current via the Spin Hall Effect[83, 24]. Indeed, The requirement that YIG be grown directly on the substrate forbids fabricating devices with double-sided injection of spin current into the magnetic film[84].

Here we demonstrate experimentally that epitaxial films grown on top of Pt layers can be utilized in SHE driven spintronic devices. We show that by injecting

spin currents with moderate density, one can achieve an efficient enhancement or suppression of magnetic fluctuations, complete compensation of the natural magnetic damping, and observe a transition to the magnetization auto-oscillation regime. Surprisingly, in spite of the relatively large magnetic damping of YIG grown on Pt, the density of electrical current necessary for the onset of auto-oscillations is very close to that previously reported for high quality YIG films grown directly on GGG. This observation suggests that the transparency of the YIG/Pt interface to the spin current[84] is likely improved by growing YIG on Pt. We also show evidence for the presence of SSE induced spin currents collaborating with SHE induced spin currents to drive samples into the auto-oscillation regime.

4.1.2 Sample Details

The schematic of the experiment can be seen in figure 4.1a. The studied devices are patterned in a shape of 200 nm wide and 2 μm long nanowires from an epitaxial YIG(35 nm)/Pt(5 nm) bilayer grown on top of a GGG(110) substrate. Figure 4.1b and c show the results of the structural characterization of YIG/Pt/GGG. The X-ray difraction (XRD) measurements (Fig. 4.1b) reveal three main Bragg peaks of YIG and GGG: 220, 440, and 660, suggesting the (110) orientation of YIG and GGG. A small peak at$2\theta \approx 40.15^\circ$ (inset in Fig. 4.1b) can be identifed as the 111 peak of the Pt layer suggesting its (111) texture.

The high-resolution transmission electron microscopy (HRTEM) in real space (Fig. 4.1b) confrms sharp and clean Pt/YIG and GGG/Pt interfaces. Te (110) atomic planes of YIG and GGG are parallel to each other and show closely matched inter-planar spacing. This indicates that the crystal orientation of YIG is locked to that of the substrate through single-crystal Pt. Since GGG possesses the same crystal symmetry and nearly the same lattice constant (mismatch $\approx 0.056\%$) as YIG, it is natural to choose GGG as a material for substrate.

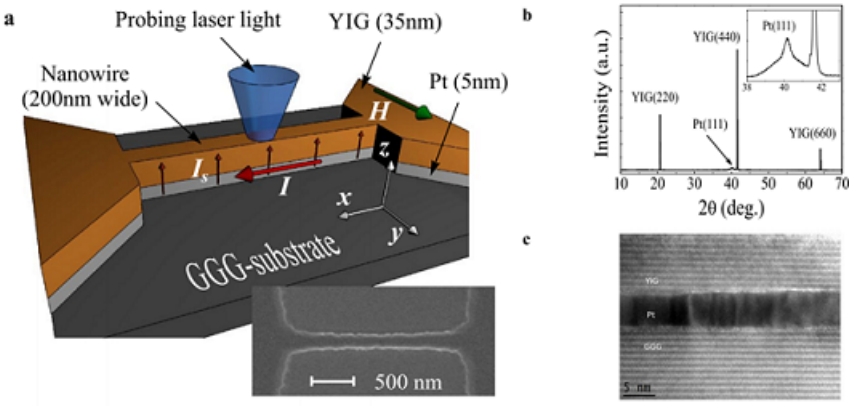

Figure 4.1: a)Test devices. (a) Schematic of the experiment. Inset shows the SEM image of the device. (b) XRD of YIG flm grown on Pt/GGG. Inset: Pt 111 peak. (c) HRTEM image of YIG/Pt/GGG multilayer.

The operation of the test device is based on the SHE, which converts the electrical current I flowing in the plane of the Pt layer into the out-of-plane spin current IS. The spin current is injected into the YIG layer through the YIG/Pt interface. It exerts a spin-transfer torque (STT)[3, 85] onto the magnetization in YIG resulting, depending on the direction of I, in an increase or decrease of the effective magnetic damping[86] and in a variation of the intensity of magnetic fluctuations[87]. The device is magnetized by the in-plane static magnetic field H applied perpendicular to the axis of the nanowire providing the maximum efficiency of the SHE-induced STT. The current passing through the Pt layer will also induce Ohmic heating resulting in a vertical temperature gradient across the sample stack which can also result in the presence of the Spin Seebeck Effect.

4.1.3 BLS measurements

Brillouin Light Scattering (BLS) was used to probe the samples. This technique uses 532 nm laser light which inelastically scatters off of the sample. The scattered light will create(destroy) a magnon and scatter with lower(higher) energy resulting

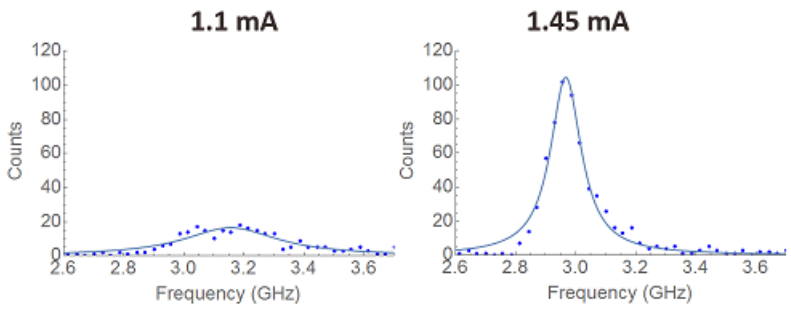

Figure 4.2: BLS spectra for different current values through the Pt layer. Integration time is 1 minute for all 3 spectra

in a frequency shift which is detected using an interferometer. The intensity of the resulting peak is proportional to the magnon number. Therefore BLS is well suited to measure the transition towards auto-oscillations, since as the natural damping is compensated by the SHE induced STT the magnon number will increase. Sample BLS spectra at three different currents can be seen in figure 4.2

The spectrum at 0.5mA shows no signal whatsoever. At 1.1 mA we can see a signal appear and by 1.45mA the peak intensity has grown sixfold. Therefore by gradually increasing current and taking BLS spectra we can see the system approach and undergo auto-oscillations. A plot of BLS intensity vs applied current can be seen in figure 4.3 where we can see that intensity initially increases with current as the intrinsic damping is overcome and magnon number increases. Instead of increasing indefinetely or going to infinity, intensity actually starts to decrease at higher currents. This is due to the effects of nonlinear magnon scattering which opens new decay channels and suppresses magnon number and therefore BLS intensity.

In order to characterize devices based on magnetic auto-oscillations it is important to note the critical current after which the system is said to be in the auto-oscillatory regime. There are a number of ways to define this current, but one rigorous method is to look at the inverse intensity. As the system approaches atuo-oscillation there will be a region of currents where there will be linear decrease

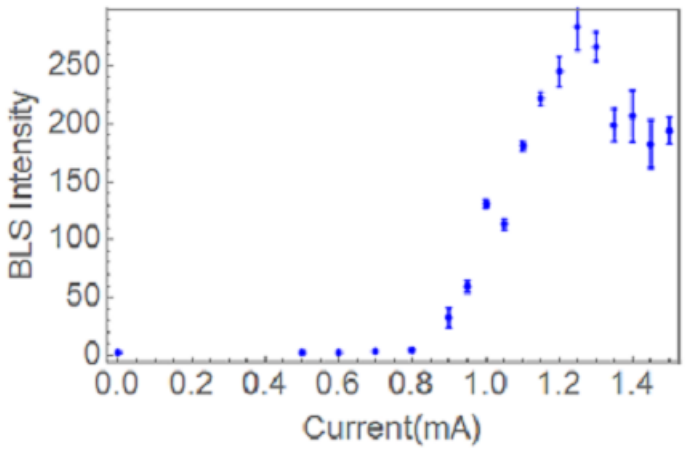

Figure 4.3: BLS intensity as a function of current through the Pt layer. The intensity increases as the system undergoes auto-oscillations, then lowers as nonlinear magnon scattering becomes dominant

in inverse intensity. By performing a linear fit we can define the critical current as the current at which the extrapolation of the linear fit predicts the inverse intensity to reach zero [88]. An example of the fitting process ca be seen in figure 4.4

All critical currents presented are determined using the technique described in this section.

In all of the measurements presented so far the angle between the applied magnetic field and the nanowire has been 90degrees in order to maximize the efficiency of the Spin Hall Effect. However, by tuning the angle between the wire and the applied field we can begin to separate the effects of the SHE from the SSE which might also be contributing to the anti-damping torque.

The spin Seebeck effect depends on the direction of the temperature gradient relative to the applied field which will remain 90 degrees for any in plane rotation. Therefore, the SSE should have no angular dependence. The Spin Hall Effect's contribution to anti-damping torque however is proportional to $m \times (m \times \sigma)$. σ is set by the direction of the interface which is unchanged and as such the SHE induced

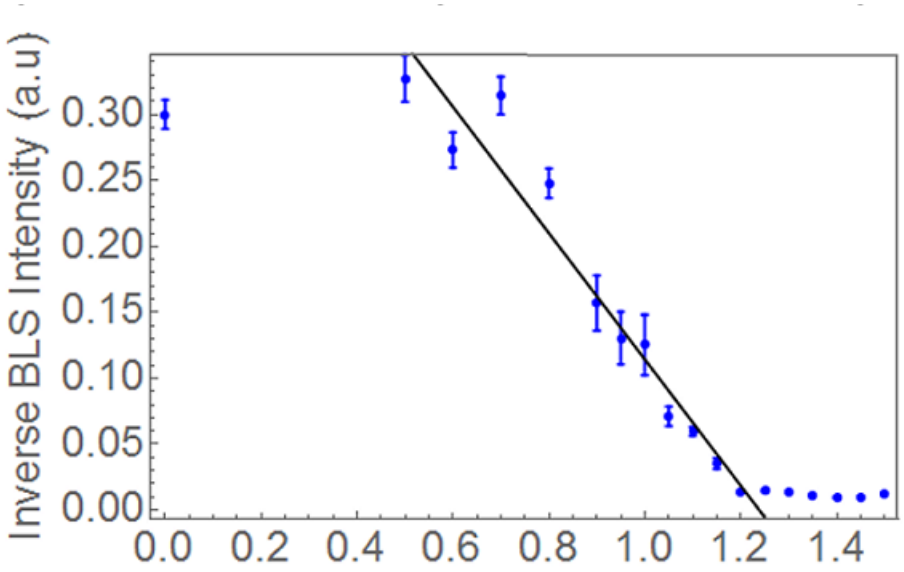

Figure 4.4: Inverse BLS intensity as a function of current through the Pt layer. Solid line is a fit through the linear region. Intercept of the fit defines the critical current

effect should be proportional to $1/\sin\theta$ where θ is the angle between the nanowire and the applied field.

The first thing to do is verify that changing the angle has any effect at all. Our expectation should be that deviating from 90 degrees should result in a larger critical current. A comparison of current dependence at 80 and 55 degrees seen in figure 4.5 shows that the sample with $\theta = 55$ degrees has a higher onset current.

Next, we performed a series of measurements in order to determine the functional behaviour of critical current as a function of θ. The results are seen in figure 4.6 which also includes the behaviour predicted for a pure SHE system as a solid line.

Figure 4.6 shows that at larger angles the behaviour deviates from that predicted for a pure SHE system. Furthermore, the critical current is actually reduced compared to the prediction. Therefore, the Spin Seebeck Effect must be contributing

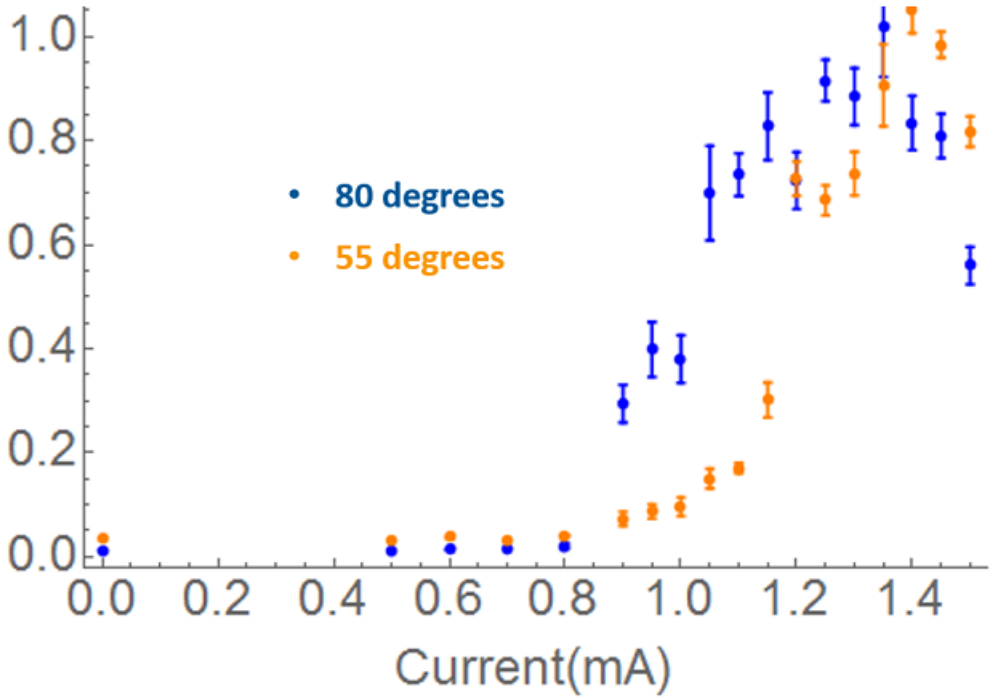

Figure 4.5: BLS intensity as a function of current for samples placed at 80 degrees (blue) and 55 degrees(orange) w.r.t. the applied field. Onset of current increase happens at a higher current for the sample with $\theta = 55$ degrees

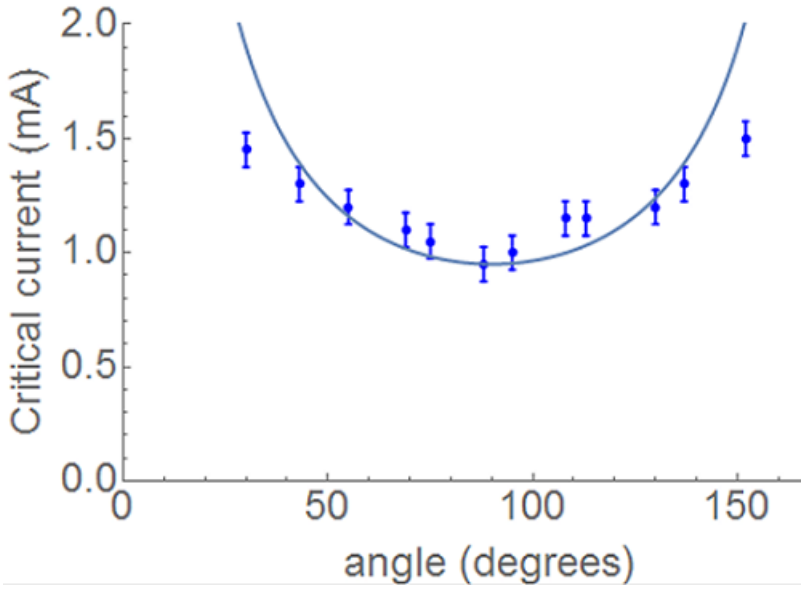

Figure 4.6: BLS intensity as a function of current for samples placed at 80 degrees (blue) and 55 degrees(orange) w.r.t. the applied field. Onset of current increase happens at a higher current for the sample with $\theta = 55$ degrees

to the generation of spin current and lowering the required onset current.

This reduction of critical current via the Spin Seebeck Effect opens the possibility of designing devices in which sample heating becomes an advantage rather than a problem by converting heat currents into spin currents to increase efficiency.

4.1.4 Conclusion

We have shown the feasibility of creating magnetic insulator based Spin Torque oscillators by growing YIG directly on platinum instead of on GGG. The current density found compares favorably to that in a device with YIG grown directly on GGG being only 20 % larger for YIG grown on platinum than the value of $4 \times 10^{11} A/m^2$ reported previously reported for YIG grown on GGG [74]. However, the linewidth reported in [74] of 2-4GHz is smaller than about a factor of two than that of our devices. This means that the similarity in current density comes from competi-

tion between increased efficiency of SHE and an increase in the amount of intrinsic damping that needs to be overcome. We also found evidence of contribution from the Spin Seebeck Effect by noting deviations from the expected angular dependence of the Spin Hall Effect.

In conclusion, we have demonstrated that efficient spin current-driven devices can be made from YIG flms grown on Pt, where the auto-oscillation characteristics are not adversely affected by the unavoidably increased magnetic damping. Our observations suggest a route for implementation of highly flexible insulator-based spintronic devices, where both interfaces of the magnetic-insulator flm are available for spin-current injection. Our results should stimulate further development of spintronic devices based on magnetic insulators.

4.2 Multiple Modes in a Nanowire Spin Torque Oscillator

[2] We investigate a Py/Pt nanowire spin torque oscillator with micron-sized lateral dimensions using the micro-Brillouin light scattering technique. We show that these wires sustain two distinct oscillatory modes with their intensity distributed in the center and along the edges of the wire, respectively. We study their different evolution towards the auto-oscillatory regime and frequency dependence beyond the threshold. The edge mode exhibits a higher critical current than the bulk mode and a qualitatively different frequency dependence as a function of the driving current. A general nonlinear oscillator model is used to explain the different characteristics of these two modes. Such information provides guidance in designing new spin torque oscillators.

[2]The discussion in this section closely resembles that of a paper not yet submitted. Work was proposed and supervised by X. Li. Measurments and modelling by K. Sobotkiewich. Samples provided by A. Smith

4.2.1 Introduction

To make more compact and energy efficient spintronic devices, it is preferred to control magnetization or its dynamics using an electric current or spin current instead of an applied magnetic field[89, 90, 91, 92, 93, 94, 95, 96, 85, 97] One class of devices that has attracted great interest is the spin torque oscillators (STOs)[68, 98, 28, 69, 5, 99, 100, 70, 101, 102] in which spin current from a heavy metal layer is transmitted to an adjacent magnetic layer and produce a sustained oscillation. The amplitude and frequency of the oscillation are controlled by the direct current passing through either the heavy metal layer or both layers. Some challenges faced in practical applications of STOs include a small output power, a limited range of oscillation frequency and frequency tunability. One possibility for increasing the output power is to explore different geometries of STOs and to increase the spatial dimension of the oscillatory region [71, 37, 103, 36, 7, 74]. Nanodisks [74], nanoconstraints [5, 70, 102] and nanowires [94, 71, 37, 103, 36] are commonly used geometries of STOs. A consequence of using a nanowire or other geometries with a larger spatial dimension is that multiple modes may co-exist in the oscillator.

In this work, we investigate a nanowire STO consisting of a Py/Pt bilayer with lateral dimensions of 1 by 2 μm. We characterize the modes of the STO using a spatially resolved micro-Brillouin light scattering (μ-BLS) technique. We observe two modes, termed a bulk mode concentrated in the center of the wire and an edge mode concentrated on the edge of the wire. As the driving direct current (DC) increases, different properties associated with the modes are observed. First of all, the critical current for the onset of the auto-oscillation is different. Frequencies of these two modes both depend on the current but in different ways. A monotonic frequency decrease is observed in the bulk mode whereas the edge mode exhibits a non-monotonic frequency change. A general nonlinear oscillator model was introduced to describe this distinct frequency dependence of the bulk and edge

modes. New information obtained in our experiments can be used to design more complex devices, which may take advantage of the rich properties of the multiple modes simultaneously present in a single STO.

4.2.2 Sample Details

The nanowire investigated is illustrated in Fig. 4.7a, with dimensions of 6 mm by 1 μm. The active area for STO devices is 1 by 2 μm. The multilayer thin film consisting of Pt(5nm)/Ni80Fe20(6nm)/AlOx (4 nm)/(GaAs substrate) were deposited by magnetron sputtering. The nanowires were fabricated via e-beam lithography and Ar plasma etching. Two Au(35 nm)/Cr(7 nm) electric contacts were attached to each nanowire to inject the driving DC. Pt is chosen as the heavy metal layer for its high spin orbit coupling strength, which leads to a high DC (J_c) to spin current (J_s) conversion efficiency whereas Ni80Fe20(6nm), which is referred to as Py, is chosen as the FM layer due to its relatively low damping. An in-plane external field of $\approx$ 500 Oe was applied perpendicular to the wire to saturate the magnetization. The current and B-field direction were chosen such that the spin current transmitted to the Py layer created an anti-damping like torque. An auto-oscillation was induced when the DC passed a threshold value.

4.2.3 BLS Measurements

We apply μ-BLS to characterize the oscillation modes supported by the nanowire STO. A 532 nm laser is incident on the sample with a focused spot size of 0.8 m in diameter. The laser spot and the wire are imaged in Fig. 4.7. The inelastically scattered light is sent to a Sandercock interferometer. BLS offers several advantages in comparison to typical microwave measurements performed on STNOs. The high sensitivity of the BLS allows us to observe thermally excited magnons even in the absence of any driving DC and to monitor the cross-over into the auto-oscillation

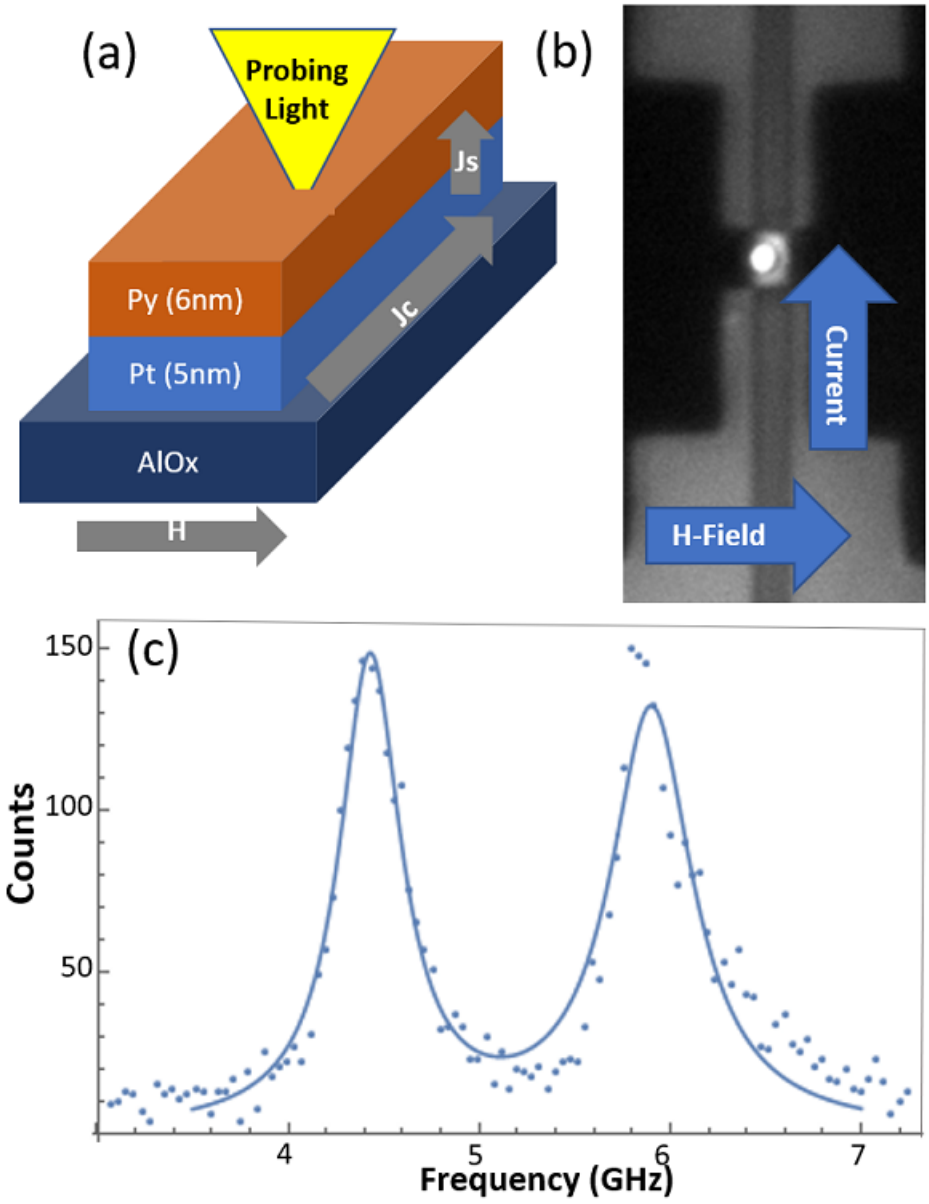

Figure 4.7: Sample Structure, experimental geometry, and a BLS spectrum. a) Schematic of the Py/Pt nanowire STO device. The applied B field is perpendicular to the wire axis. A charge current J_c is sent through the wire and the spin hall effect creates a perpendicular spin current J_s. The probing light comes from the top along the surface normal and the reflected light is sent to the Fabry-Perot interferometer. b) Optical microscope image of the sample used to monitor the laser position on the sample. c) An example BLS spectrum from BLS at a driving current of 8.75 mA and with the laser spot positioned as shown shown in b). Two distinct peaks correspond to the two oscillation modes.[94]

regime as the driving DC is gradually increased. Additionally, μ-BLS enables a direct spatial mapping of the intensity distribution of each mode, allowing one to identify the bulk and edge modes without any ambiguity. A representative BLS spectrum taken at 8.75 mA is shown in Fig. 4.7c. Two peaks are clearly observed in the BLS spectrum. Information about their central frequency, linewidth, and integrated intensity is extracted following fitting with a Lorentzian function to each mode. This spectrum alone is not insufficient to unambiguously identify the resonances as the bulk or edge modes.

We then performed spatially resolved BLS measurements. The beam spot was scanned across and along the wire to obtain a BLS spectrum at each location. Then, the integrated intensity of each mode following the fitting was plotted as a function of position as shown in Fig.4.8. The two modes in the raw BLS spectrum have distinct spatial profiles along the width of the wire. The higher frequency mode is concentrated in the center of the wire and, thus, is identified as the bulk mode. The lower frequency mode is concentrated near the edges, which is referred to as the edge mode. We compare the properties of these two modes in the following.

The BLS intensity as a function of applied current for both modes is summarized in Fig. 4.9., where nonmonotonic behaviors are observed for both modes. A linear relation is observed in the low DC region, corresponding to the build-up of the auto-oscillations. At higher DCs, nonlinear magnon scattering processes create new damping channels which lead to a saturation and eventual decrease of the integrated intensity. We examine the critical current associated with the onset of auto-oscillations of each mode. Critical current is usually estimated in electrical measurements because the signal is too weak to monitor the graduate change before auto-oscillations occur. Using BLS, we can define and evaluate this threshold current systematically. We plot the inverse of the BLS intensity vs. DC of the edge mode in the inset of Fig. 4.9a. A linear fit is applied in the low DC range

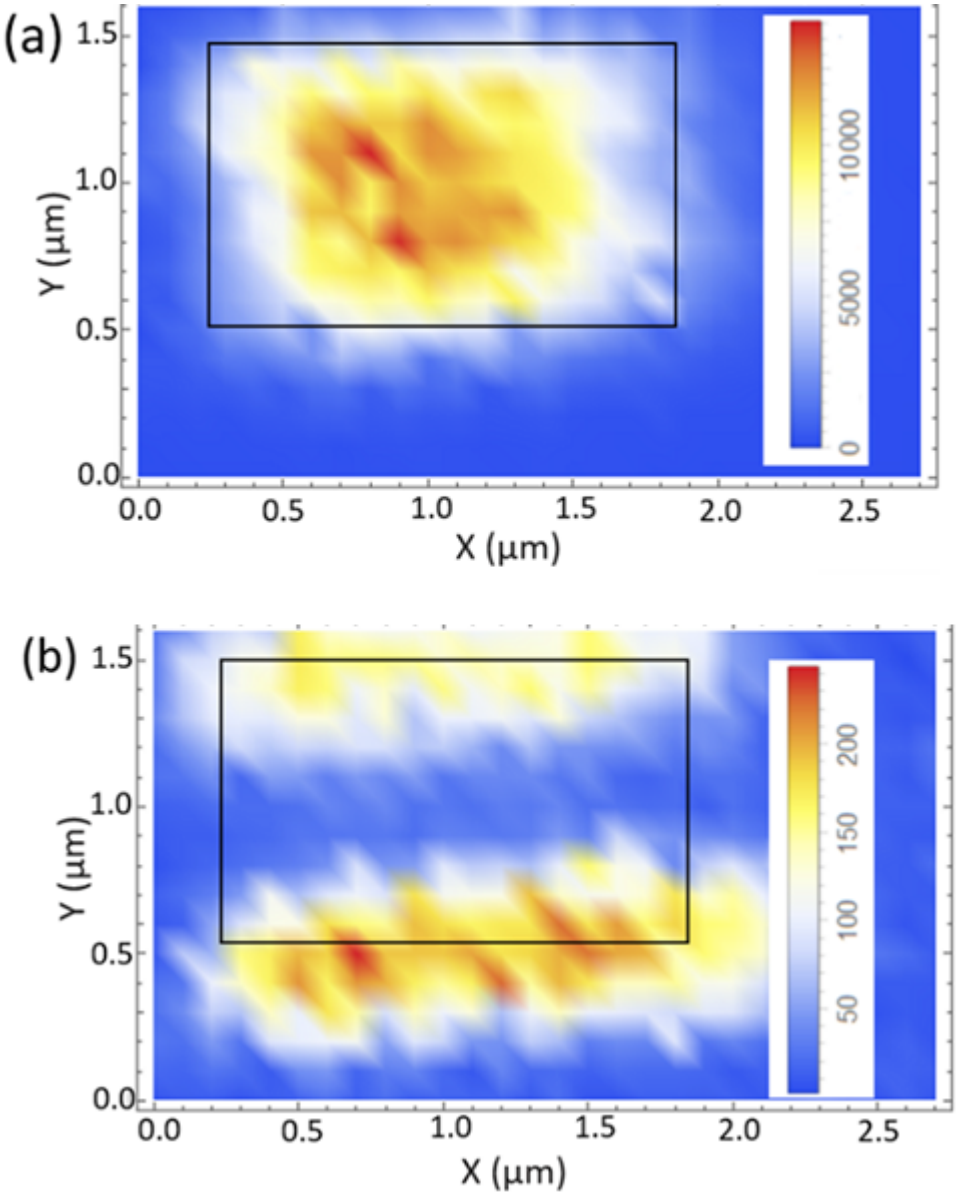

Figure 4.8: Spatial distribution of BLS intensity on the nanowire. (a) Spectrally integrated BLS intensity of higher frequency resonance is found to concentrate in the middle of the wire. This mode is referred to as the bulk mode; (b) Spectrally integrated BLS intensity of the lower frequency resonance is distributed along the sides, which is referred to as the edge mode. Intensity of bulk mode is higher than the edge mode. The black box outlines the nanowire. The spatial resolution of these images is limited by the optical diffraction limit.

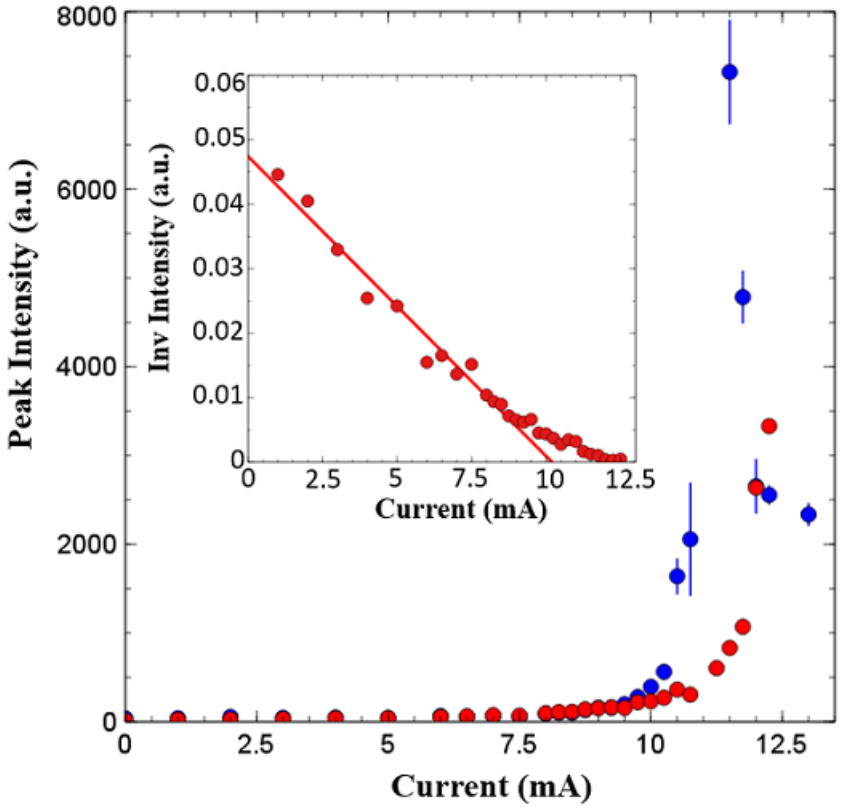

Figure 4.9: Amplitude as a function of current for both the bulk (blue) and edge (red) modes. Inset shows the inverse amplitude and a fit to the linear region. The intersection of the linear fit with the x-axis is used to determine the critical current

and the intercepting point with the x axis is defined as the critical current for the onset of auto-oscillations. This method provides a consistent definition for critical current and makes it possible to compare different modes or different devices more accurately. A critical current of 10.7mA for the edge mode and 10.2mA for the bulk mode are found, respectively. This analysis is repeated several times and for several different samples. In each case, we consistently found a higher critical current for the edge mode than the bulk mode.

4.2.4 Discussion

Difference in Critical Current

There are likely several factors contributing to the higher critical current of the edge mode. First, damping may be intrinsically higher near the edge of the wire because defects and imperfections at the edges from the fabrication process may cause additional damping. Secondly, spins injected from the regions within one diffusion length of the edge will not contribute to STT. This is because STT is proportional to[95] $(\hat{m} \times \hat{m}) \times \hat{n}$, and near the edge $\hat{n}$ is no longer well defined. The only way edge spins can contribute to STT is if the magnetization at the edge is deviated from the saturation direction [104].

Difference in frequency behaviour

Another key difference between the edge and bulk mode is how the oscillation frequency evolves with the applied current. As seen in figure 4.10 The bulk mode frequency decreases monotonically with the applied DC whereas the edge mode initially increases and then decreases in frequency.

We use the simplest model to account for the complex frequency dependence of STOs on the applied current, as first proposed by Slavin and coworkers[105]. This model is adapted from a general model of nonlinear oscillators with an effective negative damping term. Briefly, the time dependent oscillation amplitude c is governed by:

$$\frac{dc}{dt} + i\omega(|c|^2)c + \Gamma_+(|c|^2)c + \Gamma_-(|c|^2)c = 0 \tag{4.1}$$

where ω is the oscillation frequency, Γ_+ is proportional to the Gilbert Dampings and Γ_- is the effective negative damping induced by the Spin Transfer Torque. All of these parameters depend on the oscillation amplitude as follows:

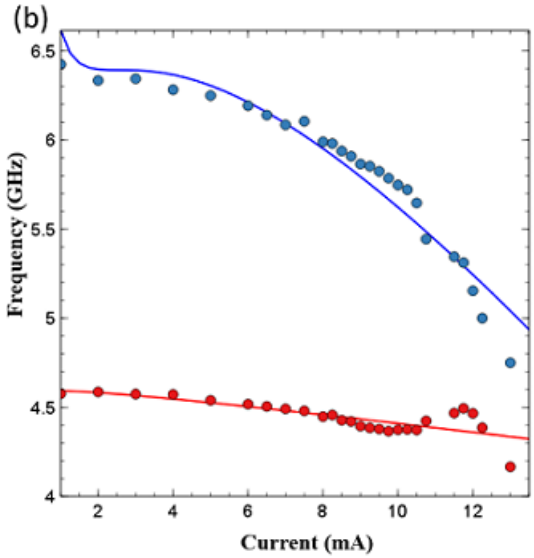

Figure 4.10: Frequency as a function of applied DC for both the bulk (blue) and edge (red) modes. Solid lines are fit to a nonlinear oscillator model. The fit to the edge mode only considers those data points below the onset of auto-oscillation

$$\Gamma_+(|c|^2) = \Gamma_G(1 + Q|c^2|) \tag{4.2}$$

$$\omega(|c|^2) = \omega_0 + N|c|^2 \tag{4.3}$$

$$\Gamma_-(|c|^2) = \sigma I(1 - |c|^2) \tag{4.4}$$

where $\Gamma_G = \alpha_G\omega$, α_G is the Gilbert damping, ω_0 is the oscillation frequency in the absence of a driving current and I is the applied current. N, and Q are parameters characterizing the nonlinearity of the anti-damping term, frequency and Gilbert damping, respectively. Of particular interest is the parameter N whose sign determines whether frequency increases or decreases.

To find a nontrivial steady-state solution for the amplitude, we take $\Gamma_+ = \Gamma_-$ which corresponds to the anti-damping like torque overcoming the intrinsic damping and thus the onset of auto-oscillations. Under this condition, the amplitude satisfies:

$$|c|^2 = \frac{\frac{\sigma I}{\Gamma_G} - 1}{\frac{\sigma I}{\Gamma_G} + Q} \tag{4.5}$$

The onset of auto-oscillations is defined by the emergence of coherent magnon with an amplitude described by c. When the driving current exceeds $I_{th} = \Gamma_G/\sigma I$ the coherent magnon intensity becomes positive. The current dependence of frequency can be rewritten as:

$$\omega(|c|^2) = \omega_0 + N\frac{\frac{I}{I_{th}} - 1}{\frac{I}{I_{th}} + Q} \tag{4.6}$$

The result of this fit for the edge and bulk modes can be seen in figure 4.10. This model works well for the bulk mode and doesnt work for the edge mode. This is because the model assumes that N itself is not frequency dependent which is a good approximation for the bulk modes but not for the edge mode.

We further explain the distinct DC dependence of the bulk and edge mode frequencies by examining the explicit forms of the nonlinear parameter N following the prior work by Dvornik et Al[106]. For the bulk mode,

$$N_{Bulk} = -\frac{\gamma^2 B N_\perp M_s}{\omega_{bulk}} \tag{4.7}$$

where γ is the gyromagnetic ratio, B is the B field in the material, $N_\perp$ is the perpendicular out-of-plane component of the demagnetization and M_s is the saturation magnetization. N_{bulk} is always negative which explains the monotonic behaviour of frequency in the bulk mode. On the other hand, this parameter for the edge mode is described by:

$$N_{edge} = -\frac{\gamma^2 B N_\perp M_s}{\omega_{edge}} + 2\frac{\gamma^2 N_\parallel M_s}{\omega_{edge}}[B + M_s(N_\perp - N_\parallel)(1 - |c|^2)] \tag{4.8}$$

where $N_{\parallel}$ is the in plane demagnetization factor. The sign of N_{edge} depends on the relative magnitude of the in-plane and out-of-plane demagnetization factors, $N_{\parallel}$ and $N_{\perp}$. The in-plane component depends on the static component of the magnetizationM_s along the direction of the applied external field. The perpendicular component depends on the dynamic component since it arises from the precession. Thus, as the system undergoes auto-oscillation, the amplitude of precession increases, leading to an increase of the perpendicular term $N_{\perp}$. As a result, N_{edge} changes its sign as the amplitude of the edge mode increases, leading to a non-monotonic change in the edge mode frequency.

We also suggest the following descriptive explanation for the non-monotonic frequency dependence of the edge mode. By increasing the amplitude of the oscillations, the deviation from saturation magnetization is increased. As the net magnetization decreases, a frequency reduction is initially observed. Further increase in the oscillation amplitude reduces the depth of the spin wells which confine the edge modes. These spin wells are created by the reduction of the effective magnetic field at the edges of the nanowire. The reduced confinement increases the frequency. These effects compete and lead to the complex frequency dependence of the edge mode. Nonmonotonic behavior of edge mode frequency was simulated and predicted in a previous paper[106]. Our experiments provide an unambiguous demonstration supported by spatial scans to ensure the identification of the modes.

4.2.5 Conclusion

In conclusion, we have studied multiple modes in a Py/Pt nanowire STO. Using the μBLS technique, we mapped out the spatial intensity distribution of these modes and identified the bulk and edge modes without any ambiguity. These two modes are found to have different critical currents for the onset of auto-oscillations. Furthermore, the oscillation frequency of the modes evolves differently as the driving DC

increases. While the frequency of the bulk modes monotonically decreases with increasing DC, the frequency of the edge modes exhibits a more complex dependence. Based on a general nonlinear oscillator model, this complex dependence is attributed to a change in the nonlinear coefficient arising from a competition between static and dynamic effects. An improved understanding of STOs with extended spatial dimensions as provided in our current studies will facilitate the development of future spintronic devices. In particular it has already been shown experimentally that by taking advantage of the more complex properties of STOs one can achieve neuromorphic computing [8] capablities. Therefore understanding more complicated behaviour may open the door to future applications.

Chapter 5

Combining Strong Damping-Like Spin Orbit Torque with tunable DMI

[1] Despite their great promise for providing a pathway for very efficient and fast manipulation of magnetization, spin-orbit torque (SOT) operations are currently energy inefficient due to a low damping-like SOT efficiency per unit current bias, and/or the very high resistivity of the spin Hall materials. This chapter shows that $Pd_{1-x}Pt_x$ is an advantageous spin Hall material as shown by three different SOT ferromagnetic detectors. The optimal $Pd_{0.25}Pt_{0.75}$ alloy has a giant internal Spin Hall ratio 0.6 (damping like efficiency ≈ 0.26 for all three ferromagnets) and a low resistivity of $\approx 57.5\mu\Omega cm$ at a 4nm thickness. Moreover, it is found that the Dzyaloshinskii-Moriya interaction (DMI) which is the key ingredient for the manipulation of chiral spin arrangements(e.g. Skyrmions and chiral domain walls)

[1]The discussion in this chapter follows closely that of ref.[34]. Samples were prepared by L.Zhu,STT work was proposed and supervised by R. Buhrman. STT measurements performed by L.Zhu. BLS measurements supervised by X.Li. BLS measurements performed by K.Sobotkiewich. Writing primarily by L.Zhu

is considerably strong at the $Pd_{1-x}Pt_x/Fe_{0.6}Co_{0.2}B_{0.2}$ interface when compared to the DMI at $Ta/Fe_{0.6}Co_{0.2}B_{0.2}$ or $W/Fe_{0.6}Co_{0.2}B_{0.2}$ interfaces and can be tuned by a factor 5 through control of the interfacial Spin Orbit Coupling via the heavy metal composition. This work establishes a very efficient spin current generator that combines a notably high energy efficiency with a very strong and tunable DMI for advance chiral spintronics and spin torque applications.

5.1 Introduction

Current induced Spin Orbit Torques (SOTs) in heavy metal/ferromagnet (HM/FM) systems have promise for faster and more efficient electrical control of the magnetization at the nanoscale than magnetic field or conventional spin transfer torque[5, 107, 56, 108, 109, 68, 110]. The damping like Spin Orbit Torque generated by the bulk Spin Hall Effect (SHE) of the HMs is of particular interest in exciting magnetization dynamics at microwave and terahertz frequencies[5, 107] driving Skyrmion and chiral domain wall displacement[56, 108] or switching the magnetization of thin film nanomagnets[109, 68, 110]. Despite extensive efforts[5, 107, 56, 108, 109, 68, 110, 111, 112] the energy efficiency of present SOT operations is limited by a relatively low damping like SOT efficiency(ξ_{dl})[68] and/or a high resistivity(ρ_{xx}) of the spin hall materials[111, 112](see Table 1). when ρ_{xx} of the spin Hall material is comparable to or larger than that of the metallic FM being manipulated, the detrimental shunting of applied current through the magnetic layer will be significant. Another important ingredient for Spin Orbit Coupling (SOC) phenomena is the Dzyaloshinskii-Moriya Interaction (DMI) at HM/FM interfaces due to the combination of broken inversion symmetry and interfacial SOC[43]. Interfacial DMI is a short range asymmetric exchange interaction that can promote chiral spin arangements such as magnetic skyrmions or chiral domain walls. [56, 108]. The sign and magnitude of the interfacial DMI influence the direction and velocity of chiral spin

	ξ_{dl}	ρ_{xx} $[\mu\Omega cm]$	$\sigma_S^* H$ $[10^5\hbar/2e\Omega^{-1}m^{-1}]$	P	ref
$Pd_{0.25}Pt_{0.75}$	0.26	57.5	4.5	0.68	[34]
$Au_{0.25}Pt_{0.75}$	0.3	83	3.6	0.82	[112]
Pt(high$\rho_x x$)	0.2	51	3.9	1	[34]
Bi_2Se_3	3.5	1755	2.0	2.1	[113]
Pt (low ρ_{xx})	0.07	20	3.5	2.8	[114]
$\beta - W$	0.3	300	1.0	5.7	[111]
$\beta - Ta$	0.12	190	0.63	16.7	[68]
Bi_xSi_{1-x}	18.6	13000	1.4	20	[115]
$(Bi, Se)_2Te_3$	0.4	4020	0.1	1479	[112]

Table 5.1: Comparison of $\xi_d l$, ρ_{xx},$\sigma_S^* H$, and normalized power consumption P for various strong spin current generators (thickness = 4 nm)

texture movement driven by damping-like SOT. For a perpendicularily magnetized multi-domain HM/FM structure, the interfacial DMI presents an obstacle for SOT switching of magnetization via a thermally activate reversal domain nucleation and domain wall depinning process[109] because it requires an external field or its equivalent that is larger than the DMI field applied in the direction of the bias current in order to switch the magnetization. This restriction leads to additional complexity in the design and implementation of SOT devices. DMI may also play a role in the sub nanosecond switching of nanoscale SOT magnetic random access memories (MRAMs)[116, 117]Therefore the exploration of new, more efficient, HM spin Hall materials and new routes to tune the the DMI strength continues to b of significant interest and technological application.

Pt is a particularily interesting spin Hall material due to its giant intrinsic spin Hall conductivity (σ_{SH}) arising from the Berry curvature of its band structure [118, 119]. However the reported values of ξ_{dl} for Pt/FM systems are generally low ≈ 0.07 in Pt/Py bilayers ($\rho_{xx} \approx 20\mu\Omega cm$) [114] and ≈ 0.12 in Pt/Co bilayers ($\rho_{xx} \approx 30\mu\Omega cm$)[120] The introduction of impurities [121] or disorder [122] has been found to raise ρ_{xx} and degrade σ_{SH} of Pt at the same time. A good trade off between ρ_{xx}

and σ_{SH} can enhance ξ_{dl} to some degree (0.16 [122]) because $\xi_{dl} = T_{int}(2e/\hbar)\sigma_{SH}\rho_{xx}$ for the intrinc SHE mechanism ($T_{int}$is the interfacial spin transparency). Alloying Pt with Au was recently found to be more effective than introducing impurities or disorders in enhancing $\xi_d l$ as it allows significant increase in ρ_{xx} without degrading the σ_{SH} in the Face Centered Cubic(FCC) alloy with the optimized composition [119]

In this work, based on direct spin torque measured using Perpendicular Magnetic Anisotropy(PMA) Co, In-Plane Magnetic Anisotropy (IMA) Co and IMA $Fe_{0.6}Co_{0.2}B_{0.2}$(CoFeB) as the FM detectors, we report an effective magnification of the damping-like SOT efficiency and internal Spin Hall conductivity (i.e ξ_{dl} and σSH) in $Pd_{1-x}Pt_x$ alloys. A large ξ_{dl} of ≈ 0.26 and a giant σ_{SH} of $1.1 \times 10^6\hbar/2e\Omega^{-1}m^{-1}$ was obtained in $Pd_{0.25}Pt_{0.75}$ which still has a relatively low resistivity of $\approx 57.5\mu\Omega cm$ making $Pd_{0.25}Pt_{0.75}$ a strong and particularly advantageous spin Hall material from the point of view of energy efficiency and spintronic applications. We also find from Brillouin Light Scattering (BLS) measurements that the DMI at $Pd_{1-x}Pt_x/Fe_{0.6}Co_{0.2}B_{0.2}$ interfaces is both considerably strong and variable over a wide range (factor of 5) by controlling the interfacial SOC via the HM composition.

5.2 Sample Details

$Pd_{1-x}Pt_x(d)/Co(t)$ and $Pd_{1-x}Pt_x(d)/Fe_{0.6}Co_{0.2}B_{0.2}(t)$ bilayers were sputter deposited (t and d are thicknesses in nm) with different Pt concentrations onto oxidized Si substrates (see figure 5.1a).

The Co layers were wedges with thicknesses varying between 0.75 and 1.4 nm for x=1 and between 0.64 and 0.94 nm for x $\leq$ 0.75 across the wafer to enable the study of both IMA and PMA $Pd_{1-x}Pt_x/Co$ devices. For $Pd_{1-x}Pt_x(d)/Co(t)$ bilayers the saturation magnetization (M_s) varies between 1450 and 1700 emu cm^{-3}

for different x, indicative of an enhancement due to a magnetic proximity effect at the interface[123]. However the proximity effect should not degrade ξ_{dl} as seen in previous works[124, 125]. M_s for the $Pd_{1-x}Pt_x/Fe_{0.6}Co_{0.2}B_{0.2}$ bilayers remains at an almost constant value of $\approx$ 1200 emu cm^{-3}. The magnetic bilayer samples were further patterned into $5\times60\mu m^2$ Hall bars for measuring SOT by out of plane (PMA bilayers) and in-plane (IMA bilayers) harmonic response measurements[126, 127].

5.3 Tuning the SHE by Composition

We determined ρ_{xx} for 4nm $Pd_{1-x}Pt_x$ by substracting the sheet conductance of reference stacks Ta 1/Co t/MgO 2/Ta 1.5 and Ta 1/CoFeB t/MgO 2/Ta 1.5 from that of our samples containing the $Pd_{1-x}Pt_x$ layer. The result is plotted in figure 5.1b and we can see that ρ_{xx} for 4nm $Pd_{1-x}Pt_x$ layers varies between 37.0 and 57.6 $\mu\Omega cm$ for different x. The alloys with 0.25 leq x $\leq$ 0.75 have greater ρ_{xx} than pure Pt or Pd for all three FM cases, which we attribute to enhanced electron scattering in the chemically disordered alloys. At a given x there are only small differences in ρ_{xx} for the three ferromagnets, likely due to small differences in interfacial scattering. Figure 5.1c shows the x dependence of ξ_{dl} generated by 4nm $Pd_{1-x}Pt_x$ for PMA Co (t=0.64 or 0.75) IMA Co (t = 0.94 or 1.4) and IMA CoFeB (t = 2.8) detectors. Here $\xi_{dl} = 2e\mu_0 M_s t H_{dl}/\hbar j_e$ where H_{dl} is the damping like SOT effective field and M_s is the saturation magnetization. For all three FM cases ξ_{dl} increases quickly from $\approx$ 0.07 at x=0 (pure Pd) to the peak value of $\approx$ 0.26 at x=075 then drops to $\approx$ 0.2 at x = 0 (pure Pt). The consistent peak behaviour of ξ_d at x $\approx$ is attributable to the monotonic dependence of ρ_{xx} on x (see figure5.1b) and the giant apparent spin Hall conductivity $\sigma^*_{SH} = T_{int}\sigma_{SH} = (\hbar/2e)\xi_{dl}/\rho_{xx}$ for x $\geq$ 0.75. As seen in figure 5.1d σ^*_{SH} for 4nm $Pd_{1-x}Pt_x$ increases monotonically with x and exhibits a weak peak at x $\approx$ 0.75 for the PMA case. The x dependence is functionally similar to the predicted behaviour for the intrinsic spin Hall conductivities of $Pd_{1-x}Pt_x$ alloys in

a recent ab initio calculation[128] although as we will discuss later the actuall spin Hall conductivites for $Pd_{1-x}Pt_x$ are much larger than the ones indicated by Ma et. al.[128] once the degradation of T_{int} by spin backflow (SBF) and spin memory loss (SML) at the FM interfaces is taken into account[129]. Finally, it is important to note that for each FM case the σ^*_{SH} of the 4 nm $Pd_{1-x}Pt_x$ is comparable to that of pure Pt. This is distinct from the case of introducing Hf impurities into Pt[121] where σ^*_{SH} is degraded by over 25 % after the Hf concentration reaches 12.5%. Another interesting observation is that σ^*_{SH} for each of the three FM detectors. This difference is attributable in part to the Co thickness in the PMA sample being less than the spin dephasing length ($\approx$ 1nm) because of which the spin is not completely absorbed after going through thr FM layer[120]. The difference could also be due to differences in SBF and SML at the different interfaces although there isn't direct evidence for this.

The spin diffusion length (λ_s) and the spin conductance $1/\lambda_s\rho_{xx}$ are two key parameters for understanding a spin Hall material, for determining the spin Hall angle (θ_{SH}) of a HM via an inverse spin Hall experiment, and for optimizing the SOT effectiveness of the material. We determined $1/\lambda_s\rho_{xx}$ for $Pd_{0.25}Pt_{0.75}$ (the optimal composition for ξ_{dl} by studying H_{DL} and ξ_{dl} for a series of $Pd_{0.25}Pt_{0.75}d/Co$ 0.64 bilayers as a function of d. As seen in figure 5.2a H_{DL}/E initially increases quickly and then gradually saturates with increasing d which is consistent with the spin diffusion behaviour expected by the SHE model. ξ_{dl} however, first increases as d increases from 2nm, peaks at 3-4 nm and then drops gradually as d increases further as seen in figure 5.2b. This is a direct consequence of the combination of the decrease in ρ_{xx} with d as interfacial scattering becomes less dominant(figure 5.2c, and the rapid then saturating increase in σ^*_{SH} as d increases up to and beyond the heavy metal's spin diffusion length(black squares in figure 5.2d). Overall the average resistivity ρ_{xx} of the $Pd_{0.25}Pt_{0.75}$ layers drops from 86.8 $\mu\Omega cm$ at d = 2nm to 37.4

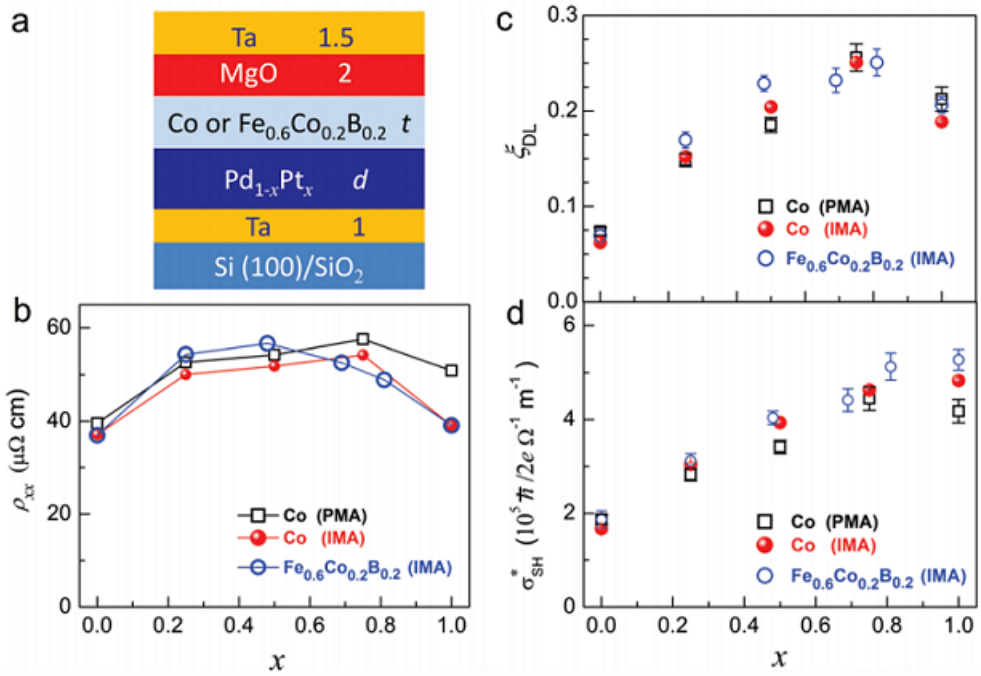

Figure 5.1: a) Schematic depiction of the magnetic stacks. b) x dependence of $Pd_{1-x}Pt_x$ resistivity (ρ_{xx} c) x dependence of ξ_{dl} d) x dependence of σ^*_{SH}. b,c,d are for 4nm $Pd_{1-x}Pt_x$ using Co and CoFeB as FM detectors in the SOT measurement

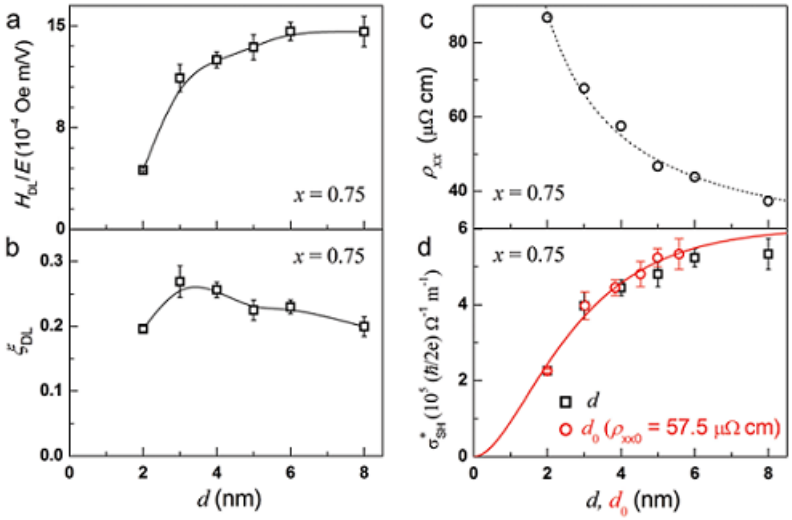

Figure 5.2: $Pd_{0.25}Pt_{0.75}$ thickness(d) dependence of a) H_{DL}/E b)ξ_{dl} and c) ρ_{xx} d)σ^*_{SH} plotted as a function of d(black squares) and the rescaled effective thickness (d_0, red circles). The solid curve donates the best $\sigma^*_{SH} - d_0$ fit. In (d), d_0 was rescaled with the resistivity of the 4 nm $Pd_{0.25}Pt_{0.75}$ film ($\rho_{xx0} = 57.5\mu\Omega cm$)

$\mu\Omega cm$ at d = 8nm. This interesting peak beaviour of ξ_{dl} and the strong thickness dependence of ρ_{xx} were not observed in $Au_{0.25}Pt_{0.75}$ where the mean free path is very short[119].

If we assume the typical case where the spin mixing conductance can be approximated by $G^{\uparrow\downarrow} \approx ReG^{\uparrow\downarrow}$, SML is negligible at HM/FM interface and λ_s is independent of ρ_{xx}, then we can obtain both λ_s and σ_{SH} using[130]:

$$\sigma^*_{SH} = \sigma_{SH}(1 - sech(d/\lambda_s))(1 + tanh(d/\lambda_s)/2\lambda_s\rho_{xx}ReG^{\uparrow\downarrow})^{-1} \tag{5.1}$$

However, this equation is not valid for $Pd_{0.25}Pt_{0.75}$ since ρ_{xx} varies with both d and $lambda_s$ is not a constant if the Elliot-Yafet spin mechanism dominates, where $\lambda_s \propto 1/\rho_{xx}$. Considering this effect we use the "rescaling method introduced in Nguyen et. al[130] to analyze the data. In figure 5.2d σ^*_{SH} is plotted as a function of

the rescaled thickness d_0 (red circles) which uses 57.5 $\mu\Omega cm$, the average resistivity of the 4nm $Pd_{0.25}Pt_{0.75}$ film as the constant reference resistivity ($\rho xx0$). Using $G^{\uparrow\downarrow} = 6\times10^{14}\Omega^{-1}m^{-2}$, a value calculated for Pt/Co[131], as an approximation, the best fit of σ^*_{SH} versus d_0 to the above equation gives $\sigma_{SH} \approx (1.05\pm0.02)\times10^6\hbar/2e\Omega^{-1}m^{-1}$, $\lambda_s \approx 1.95\pm0.12$(for 4nm thickness) and $T_int = 0.43$. Accordingly the internal θ_{SH} for 4 nm $Pd_{0.25}Pt_{0.75}$ is determined to be greater than 0.6 after the SBF correction.

From these results we find $1/\lambda_s\rho_{xx}$ for $Pd_{0.25}Pt_{0.75}$ to be $\approx 0.89\times10^{15}\Omega^{-1}m^{-2}$ which is slightly larger than $0.71\times10^{15}\Omega^{-1}m^{-2}$ for $Au_{0.25}Pt_{0.75}$ but considerably lower than $1.3\times10^{15}\Omega^{-1}m^{-2}$ obtained for Pt from a similar Pt thickness dependence study[130]. The relatively low spin conductance of $Pd_{0.25}Pt_{0.75}$ is advantageous for reducing SBF at $Pd_{0.25}Pt_{0.75}/FM$ interfaces. It is also to be noted that the large value for σ_{SH} is still a lower bound as it assumes an ideal $Pd_{1-x}Pt_x/Co$ interface and does not take into account any SML induced by interfacial spin-orbit scattering. This lower bound spin conductivity is substantially larger than those previously reported for pure Pt and for the $Au_{0.25}Pt_{0.75}$ alloy[130, 130].

5.4 Strong and Tunable Interfacial DMI

Interfacial DMI is an important factor for many SOT phenomena and applications [56, 108, 109] and so it makes sense to determine the strength of DMI for bilayers involving $Pd_{1-x}Pt_x$ alloys. In particular, we determined the strength of DMI in $Pd_{1-x}Pt_x(4)/CoFeB(2.6)$ bilayers by using Brillouin Light Scattering (BLS) to measure the DMI induced shift in frequency between counter-propagating Damon-Eschbach modes (Δf_{DM}). Figure 5.4a shows the geometry of the BLS measurements where a magnetic field H = 1700 Oe is applied along the x direction to saturate the magnetization of the FM layer. The total in plane momentum is conserved during the scattering process. The (anti)Stokes peaks in the BLS spectra correspond to the (annihilation) creation of magnons with wave vector $k = \pm4\pi sin\theta/\lambda$ where θ

is the angle of incidence with respect to the normal to the surface and $\lambda = 532nm$ is the wavelength of the incident light. Figure 5.4b shows Δf_{DM} as a function of k for dfferent values of x. As discussed in section 2.1.7 Δf_{DM} is an average of the shift for positive and negative H. Figure 5.4c shows a sample BLS spectrum with H = + 1700 Oe, x = 1 and $k = 9.6\mu m^{-1}$. The linear relation between k and Δf_{DM} follows the usual relation $\Delta f_{DM} = (2\gamma/\pi\mu_0 Ms)Dk)$ [55, 48] where $\gamma = 17.6GHz/T$ is the gyromagnetic ration and D is the averaged(volumetric) DMI constant over the FM thickness. Figure 5.4d shows that by increasing x the value of D was tuned by a factor of $\approx$ 5 from -0.57 to -0.12 erg cm^{-2}. This strong tunability of interfacial DMI is mainly attributed to the variation of the SOC strength at the $Pd_{1-x}Pt_x(4)/CoFeB(2.6)$ interface as indicated by the linear relation between D and the interfacial magnetic anisotropy energy density (K_s) seen in figure 5.4e. K_s was determined from CoFeB thickness dependent anisotropy studies using spin-torque ferromagnetic resonance.

We interpret the intercept of the K_s-D fit as representing the contribution of the CoFeB/MgO interface to the overall interfacial anisotropy energy density i.e. $K_s(\text{MgO}) \approx 0.49 ergcm^{-2}$ for these as-grown/unnannealed samples while $K_s - K_s(MGO)$ is the contribution from the $Pd_{1-x}Pt_x/Fe_{0.6}Co_{0.2}B_{0.2}$ interface and is an indicator of the interfacial SOC strength. Taking into account the inverse dependence of D on FM thickness t we can define the interfacial DMI strength of the HM/CoFeB interface as $D_s = Dt$. For $Pd_{1-x}Pt_x/Fe_{0.6}Co_{0.2}B_{0.2}$ interfaces D_s ranges from $-1.47 \times 10^{-7} ergcm^{-1}$ at x =1 to $-0.30 \times 10^{-7} ergcm^{-1}$ at x = 0. The DMI at these interfaces is strong compared to Ta/CoFeB or W/CoFeB interfaces which have D_s = 0.36 and 0.73 $\times 10^{-8}$ erg cm^{-1} respectively[51]. The large amplitude of the DMI, combined with its tunability of roughly a factor of three in the regime of x $\geq$ 0.5 where $\xi_{dl} \geq 0.2$ makes $Pd_{1-x}Pt_x$ especially intriguing for developping new chiral spintronic devices and for exploring new DMI effects on the

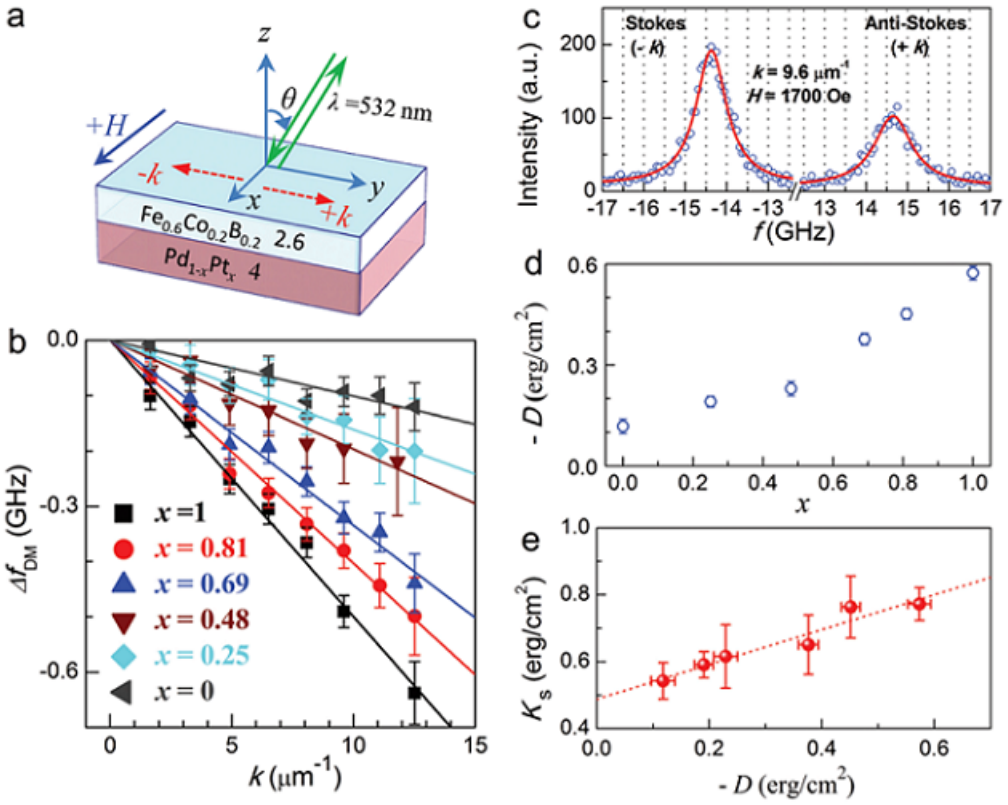

Figure 5.3: a) BLS measurement geometry.b) k dependence of Δf_{DM} c) BLS spectra at k = 9.6 μm^{-1} and H = 1700 Oe (x = 1). d) D versus x e) K_s versus D for $Pd_{1-x}Pt_x(4)/Fe_{0.6}Co_{0.2}B_{0.2}(2.6)$ bilayers with different x. The red solid curves in (c) represent fits to the Lorentzian function; the dashed line in (e)refers to the best linear fit.

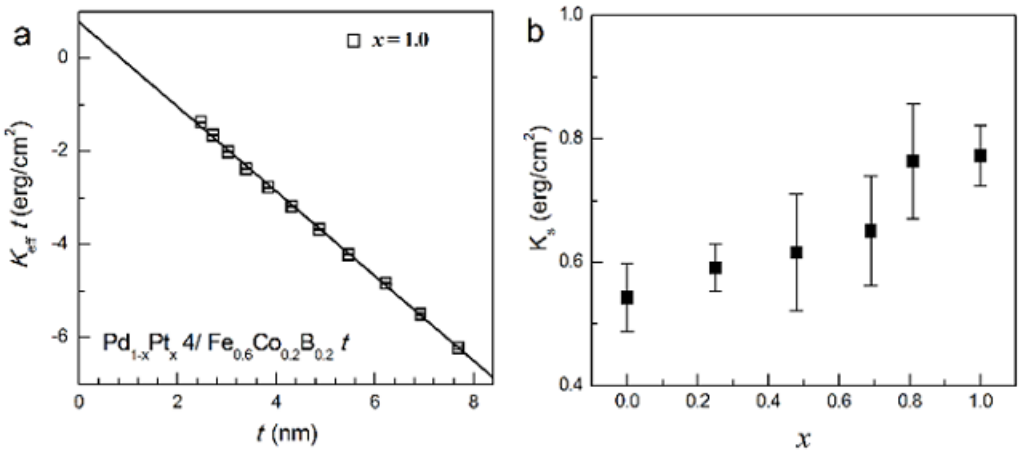

Figure 5.4: Determination of interfacial magnetic anisotropy energy density a) K_{eff}t vs t for $Pt(4)/Fe_{0.6}Co_{0.2}B_{0.2}(t)$ bilayers. Here $K_{eff} = -4\pi M_{eff}M_s/2$ is perpendicular anisotropy energy, and the effective magnetization $-4\pi M_{eff} = -4\pi M_s + 2K_s/t$and saturation magnetization M_s are determined by spin-torque ferromagnetic resonance and VSM, respectively; b) The interfacial magnetic anisotropy energy density K_s determined by the intercept of linear $K_{eff}t$ - t fits following $K_{eff}t = 2\pi M_s^2 t + Ks$.

performance of Skyrmion, chiral domain wall devices and micromagnetics during SOT magnetization switching.

It is important to note the different composition dependence of interfacial DMI strength and the damping like SOT as it further confirms that the physical source of the observed strong SOTs in the $Pd_{1-x}Pt_x$/FM systems is dominated by the bulk SHE rather than the interfacial SOC. The interfacial DMI is mainly determined by the interfacial SOC which is sensitive to short range ordering at the interface[43]. For instance, the interfacial SOC at a Pt/Co interface can be significantly enhance by thermal engineering of the spin-orbit proximity effect[132]. In contrast, the damping-like SOT due to the SHE is given by $\xi_{dl} = T_{int}(2e/\hbar)\sigma_{SH}\rho_{xx}$. Neither σ_{SH} nor ρ_{xx} are directly determined by the interfacial spin orbit coupling strength. T_{int} is set by SBF (related to the spin diffusion length and the spin conductance of the HM and the spin mixing conductance of the interface)[130] and by

SML[132], with the latter being increased by a stronger interfacial SOC. The intrinsic SHE and σ_{SH} are determined by the Berry curvature of the band structure of the HM rather than the SOC strength[118]. For example, Au and Pt have almost the same bulk SOC strength (≈ 0.3 Ry) while Pt has almost a 4 times stronger spin Hall conductivity than Au[118]. ρ_{xx} in nonmagnetic metals is well established to be due to the scattering of electrons by impurities and thermal phonons. Since neither T_{int}, σ_{SH} nor ρ_{xx} are positively correlated to the interfacial SOC, their product ξ_{dl} can certainly behave very differently from interfacial SOC or DMI, for example in their dependence on composition.

5.5 Nonreciprocity Calculations

It is important to not that DMI is not the only magnetic effect which can cause the asymmetric frequency shift measured by BLS. The frequency difference arising from the nonreciprocity of counter-propagating waves could explain the frequency shifts seen in figure 5.4b. Nonreciprocity refers to the fact that Damon-Eschbach waves of opposite k values will propagate on opposite surfaces of a thin film. Given the presence of magnetic anisotropy the effective field acting on spin waves on opposing surfaces may not be equivalent. To estimate the magntiude of the frequency difference that might arise from this effect we model the anisotropy field as being entirely contained at the magnetic interface and equal to $\frac{2K_{\perp}}{M_s}$. Then by assuming the spin waves decay exponentially away from the surface on which they propagate we can estimate the effective field from the anisotropy on each mode:

$$H_k^{eff\pm} = \frac{\int H_k^{int} m^{\pm}(t) dt}{\int m^{\pm} dt} \tag{5.2}$$

The frequency shift is then estimated by finding the frequency of the modes at each different effective field and subtracting. The result can be seen in figure5.5

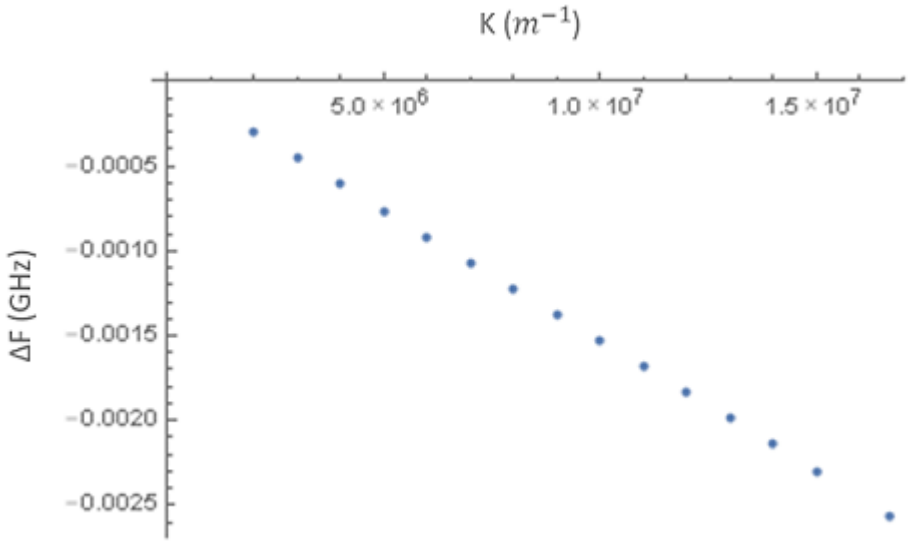

Figure 5.5: Frequency shift caused by nonreciprocity as a function of k

The frequency shift due to nonreciprocity is several orders of magnitude than that seen in figure 5.4b and can therefore be discounted. The example of figure 5.5 is for x = 0 and while the value of the nonriceprocity shift does change from sample to sample the order of magntitude is unchanged. The shifts seen in figure 5.4 can be safely attributed to DMI.

5.6 High energy efficiency in Spin-Torque Applications

Finally we emphasize that the low ρ_{xx} and giant ξ_{dl} make $Pd_{0.25}Pt_{0.75}$ advantageous for SOT research and technological applications with metallic FMs. As a simple example we show in figure 5.6a that a damping like SOT generated by the SHE of 4 nm $Pd_{0.25}Pt_{0.75}$ can switch the magnetization of a Co 0.64 layer (with an effective PMA field of 7.7 kOe and coercivity of 0.44 kOe) with a DC current of $\approx$ 4.8 mA (corresponding to $j_e = 2.2 \times 10^7$ A cm^{-2} in the $Pd_{0.25}Pt_{0.75}$ layer) and a bias field $H_x = \pm 100$ Oe applied along the current direction.

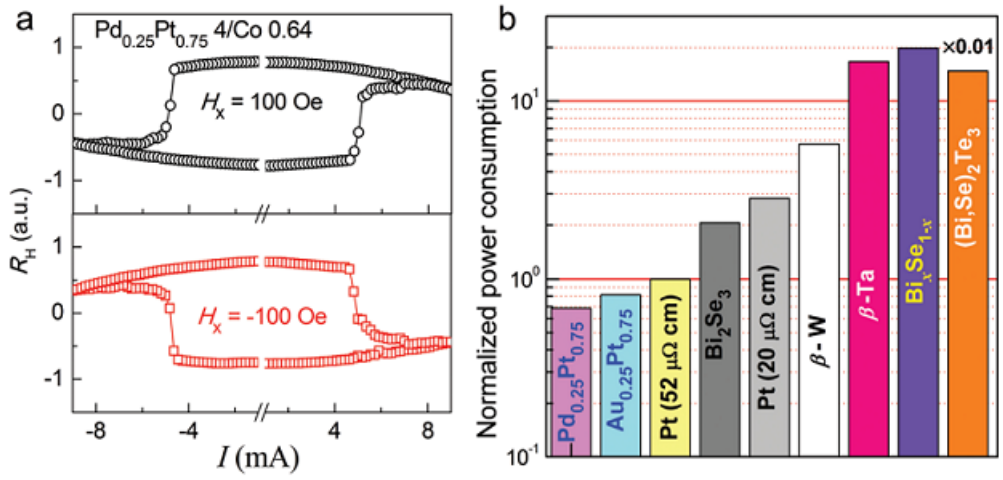

Figure 5.6: a) Deterministic current-induced magnetization switching in a perpendicularly magnetized $Pd_{0.25}Pt_{0.75}$ 4 nm/Co 0.64 nm bilayer (effective PMA field $\approx$ 7.7 kOe, coercivity $\approx$ 0.44 kOe, the width of the Hall bar is $5\mu m$ with a bias field $H_x = \pm 100$ Oe along current direction. b) Comparison of the normalized power consumption of a prototype in-plane magnetized SOT-MRAM device based on the different spin Hall channel materials listed in Table 5.1

To better illustrate the advantages of $Pd_{0.25}Pt_{0.75}$, table 5.1 the parameters most important for SOT applications are compared for various spin Hall materials. Table 5.1 and figure 5.6b also compare the calculated write power consumption (P) for a typical in-plane magnetized SOT-MRAM device, which is currently the most promising in terms of technological application's thanks to its very fast ($\approx$ 200ps), low current density, low error rate and field free switching [110, 133], based on these spin Hall materials by taking into consideration shunting into the CoFeB free layer. Here we used a 600 $\times$ 300 $\times$ 4 nm^3 spin Hall channel, a 190 $\times$ 30 $\times$ 1.8 nm^3 CoFeB free layer (resistivity $\approx$ 130 $\mu\Omega$ cm) and the parallel resistor model for the sample calculation. $Pd_{0.25}Pt_{0.75}$ has the smallest required write power of any of the materials considered. Devices based on $Pd_{0.25}Pt_{0.75}$ are predicted to be more energy efficient even than those based on topological insulator such as Bi_2Si_3, $(Bi,Se)_2Te_3$ and Bi_xSe_{1-x} despite TIs having large damping like SOT efficiencies (ξ_{dl} = 3.5,0.4

and 18.6 respectively)[113, 112, 115], mainly because the colossal resistivity of the topological insulators results in very large shunting of the current into the magnetic layer and giant energy consumption in the channel.

The small resistivity makes $Pd_{0.25}Pt_{0.75}$ more appealing than $Au_{0.25}Pt_{0.75}$ [119] for certain device applications such as cryogenic computing where the transistor circuits require a small write impedance for magnetic memory devices[134]. Moreover, $Pd_{0.25}Pt_{0.75}$ is compatible with both sputtering techniques and the use of Si substrates which are preferable for integration technology. Therefore, the combination of the giant ξ_{dl}, the low ρ_{xx} and the compatibility with microelectrics manufacturing technology makes $Pd_{0.25}Pt_{0.75}$ a particularly attractive spin Hall material for the generation and detection of spin currents in spintronic devices. We note that if in the future the low resistivity strong spin Hall materials can be combined with low M_S free layer materials such as compensated ferrimagnets[135, 136] or synthetic antiferromagnets[137] in a high quality magnetic tunnel junction configuration, the result could be ultra low power magnetic memories.

5.7 Conclusion

In conclusion, we have established via direct SOT measurements a strong internal spin Hall material, $Pd_{0.25}Pt_{0.75}$, which has a giant internal spin Hall ratio of > 0.60 (yielding $\xi_{dl} \approx 0.26$ for bilayers with either Co of CoFeB) spin Hall conductivity of $> 1.1 \times 10^6 \hbar/2e\Omega^{-1}m^{-1}$, spin conductance $1/\lambda_s\rho_{xx}$ of $0.89 \times 10^{15}\Omega^{-1}m^{-1}$ and a relatively low ρ_{xx} of ≈ 57.5 $\mu\Omega$ cm. In particular, the giant SHE and low $\rho_x x$ make $Pd_{0.25}Pt_{0.75}$ more energy efficient for manipulating metallic devices than other HMs (Ta, W, Pt and $Au_{0.25}Pt_{0.75}$) and the topological insulator Bi_xSe_{1-x}, Bi_2Se_3 and $(Bi, Se)_2Te_3$. We also find that the DMI at the $Pd_{0.25}Pt_{0.75}/Fe_{0.6}Co_{0.2}B_{0.2}$ interfaces is very strong and tunable by approximately a factor of 5 by tuning the Pt concentration x. Our findings provide a highly efficient spin Hall material system

that simultaneously combines a giant SHE, low resistivity, and strong and tunable DMI, with excellent processing compatibility for device integration, for developing new efficient SOT-driven magnetic memories and chiral (skyrmion and chiral domain walls) spintronic devices.

Chapter 6

DMI in Epitaxially Grown, Low-Damping CoFe alloys

Low Gilbert damping is a requirement for many spintronic applications. Traditionally, low Gilbert damping materials are insulators such as YIG which are suitable for many applications s[76, 138, 139, 140, 141, 81, 142, 143, 144, 145, 146]. However, they are not suitable for spintronic devices based on charge currents which require metallic FMs[147, 148, 149, 150, 151, 152]. Therefore the discovery of low damping Ferromagnetic layers is very desirable. A CoFe alloy with a 25 % Co concentration has been shown to have suppressed magnetic damping [153] corresponding to a minimum in the density of states of d-electrons at the Fermi energy. Those electrons provide the primary scattering mechanism leading to magnetic damping and so by minimizing the density Gilbert damping is minimized and was shown to have a minimum $\alpha = 2.1 \times 10^{-3}$. The density of d electrons has been previously shown to be key to the Dzyaloshinskii-Moriya interaction[51]. It becomes therefore natural to study DMI in bilayers of this material with a Heavy Metal.

However, the material grown in ref[153] is polycrystalline. It has been shown that epitaxially grown Fe and Fe alloys can have Gilbert damping $\alpha =$

1.9×10^{-3}[154, 155, 156] and so it stands to reason that by epitaxially growing CoFe alloys damping can be further minimized. This was accomplished by Lee et. al. [35] who achieved $\alpha = 1.4 \times 10^{-3}$. Furthermore, DMI in epitaxially grown FMs has been garnering growing interest due to the possibility of easing supporting theoretical calculations[157, 158, 159].

We study the properties of the Dzyaloshinskii-Moriya interactions in CoFe alloys with Pt acting as the Heavy Metal layer in order to better characterize the material for possible chiral spintronic or skyrmionic applications.

6.1 Sample Growth

The growths were done using ultrahigh vacuum, off-axis sputtering. We first grew 10 nm polycrystalline $Co_{25}Fe_{75}$ films on Si at room temperature with a 3 nm Cu seed layer and 5 nm Cr cap, which exhibited a low damping constant similar to that previously reported [153]. Once this procedure was confirmed, the epitaxial films were grown using DC sputtering and $Co_{25}Fe_{75}$ was deposited at a substrate temperature of 300 degrees Celcius directly onto (001) oriented $MgAl_2O_4$ (MAO) substrates chosen for their low lattice mismatch with $Co_{25}Fe_{75}$ (0.4%). Then a Pt capping layer is added. Pt is chosen because it has been shown to be a good HM for DMI purposes[51].

6.2 First DMI measurements

We measure the strength of DMI in $Co_{25}Fe_{75}/Pt$ bilayers using Brillouin Light Scattering (BLS)[48]. BLS measures the frequency difference between counterpropagating Damon-Eschbach waves (F_{DMI}) by finding the frequency difference between the Stokes and Anti-Stokes modes which correspond to the creation and annhilation of magnons respectively. Since the total in-plane momentum must be conserved in a

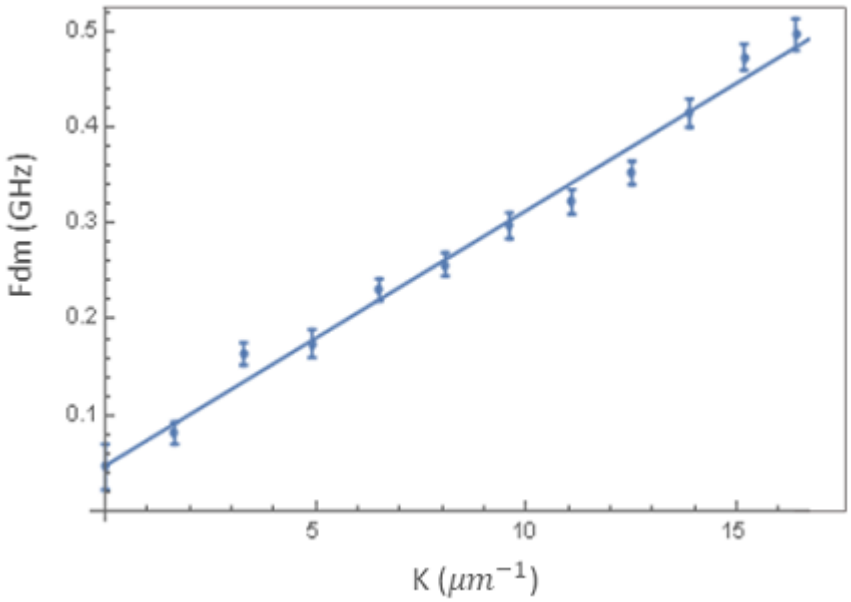

Figure 6.1: F_{dmi} vs k for 3nm Pt on 3nm thick $Co_{25}Fe_{75}$

scattering event the magnons created and annhilated must have equal and opposite momenta. The magnitude of the momenta and therefore the momentum difference is controlled by varying θ the angle of incidence of the 532nm laser light. A Sandercock interferometer[61] is used to measure the frequency difference. The DMI coefficient is found from fitting a linear relation between the frequency difference and k ($f_{DMI} = sgn(M_s)\frac{\gamma}{\pi M_s}Dk$)[48, 55].

An example of such a fitting can be seen in figure 6.1 where f_{DMI} vs k can be seen for 3nm Pt on a 3nm thick $Co_{25}Fe_{75}$ layer.

The strength of DMI was found for several different thicknesses of the CoFe layer and the results are plotted in fig 6.2. The first striking result is that we do not see the 1/t dependence typically expected for an interfacial DMI [44, 45, 46, 47]. Deviations from 1/t have been seen previously and occur when a competing magnetic effect masks the intrinsic 1/t dependence from the interfacial effect [48, 49]. Therefore to look for possible causes of this deviation we investigated other magnetic

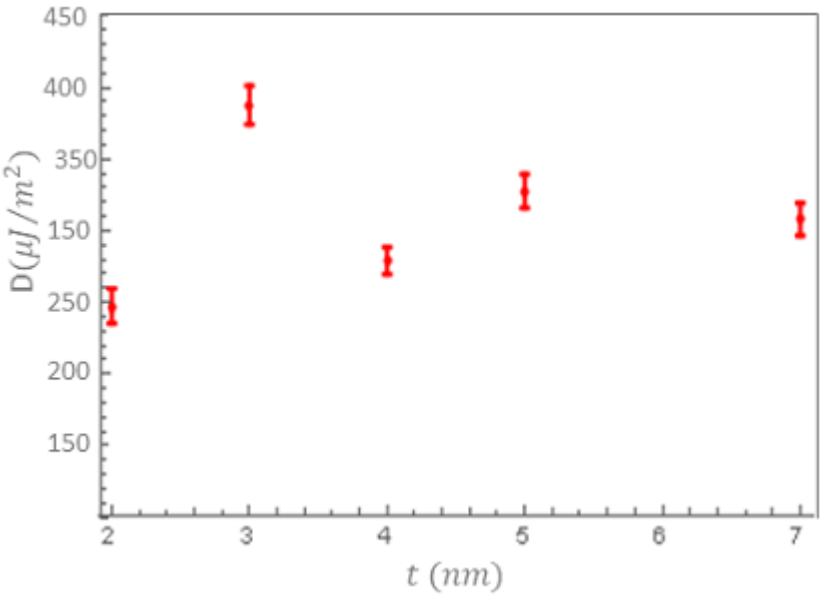

Figure 6.2: D for different thickness of 3nm Pt on $Co_{25}Fe_{75}$

properties of the system.

6.3 Anisotropy and Exchange

The first magnetic property we investigated is magnetic anisotropy. The anisotropy should be thickness dependent since it is shape dependent [19]. In particular, $K_\perp$ and its associated field should be stronger for thinner samples since they are more anisotropic by shape.

We determine the anisotropy field $\frac{2K_\perp}{M_s}$ (with M_s the saturation magnetization) by measuring BLS frequency as a function of magnetic field and fitting to the Kittel equation[18]

$$f = \frac{\gamma}{2\pi}\sqrt{H(H + 4\pi M_{EFF}} \tag{6.1}$$

where γ is the gyromagnetic ration, H is the applied field and M_{EFF} =

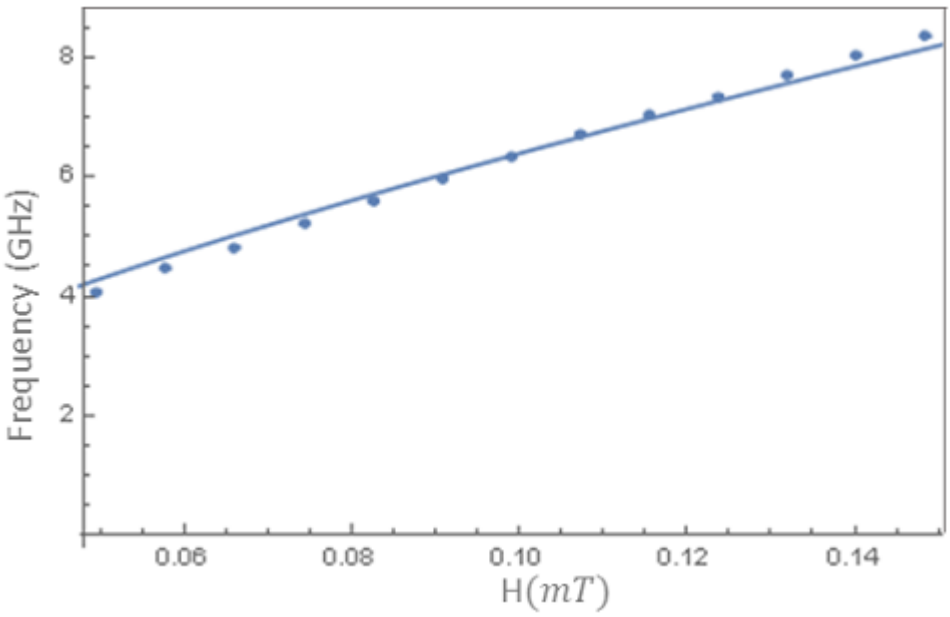

Figure 6.3: f vs H for 3nm Pt on 3nm $Co_{25}Fe_{75}$. Solid line is the fitting to the Kittel equation

$4\pi M_s - \frac{2K_\perp}{M_s}$. An example of this process can be seen in figure 6.3 for 3nm Pt on 2nm $Co_{25}Fe_{75}$.

Anisotropy was then found for each thickness of $Co_{25}Fe_{75}$ and plotted as a function of 1/t in figure 6.4.

The anisotropy field follows a rough 1/t dependence which follows the expected trend for the shape change. Therefore we must look to other magnetic properties for clues as to the unusual behaviour of DMI.

The next property we consider is the exchange stiffness A. To determine the exchange stiffness we look at the symmetric frequency shift as a function of k[55]. f_s = f(k) + f(-k) is given by

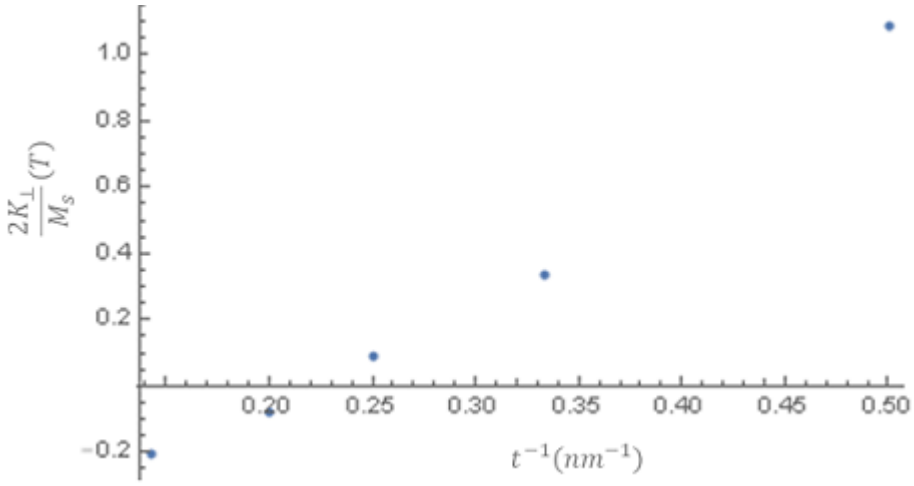

Figure 6.4: $\frac{2K_\perp}{M_s}$ for 3nm Pt on different thickness of $Co_{25}Fe_{75}$

$$\omega_s = \gamma\sqrt{(H_{eff} + \frac{2A}{M_s}k^2 + 4\pi M_s(1-\xi(kL)) - \frac{2K_\perp}{M_s})(H_{eff} + \frac{2A}{M_s}k^2 + 4\pi M_s\xi(kL))} \tag{6.2}$$

Where γ is the gyromagnetic ratio H_{eff} is the applied magnetic field, M_s is the saturation magnetization, $\frac{2K_\perp}{M_s}$ is the anisotropy field determined earlier in this section, A is the exchange stiffness which will be a fitting parameter and $\xi(kL) = 1 - \frac{1-e^{-kL}}{kL}$. An example of the fitting procedure can be seen in figure 6.5 for 3nm Pt on 2nm $Co_{25}Fe_{75}$.

Next we repeat this procedure for all thicknesses of $Co_{25}Fe_{75}$. Our expectation is for the exchange stiffness to be unchanged as it should be an intrinsic magnetic property of the material. Small differences arising from different fabrications can be expected but a priori there should be no trend. We see in figure 6.6 that our expectations are not met. Indeed there seems to be a strong correlation between A and thickness. This unexpected behaviour of exchange stiffness can provide insight into the unusual thickness dependence f DMI in this material.

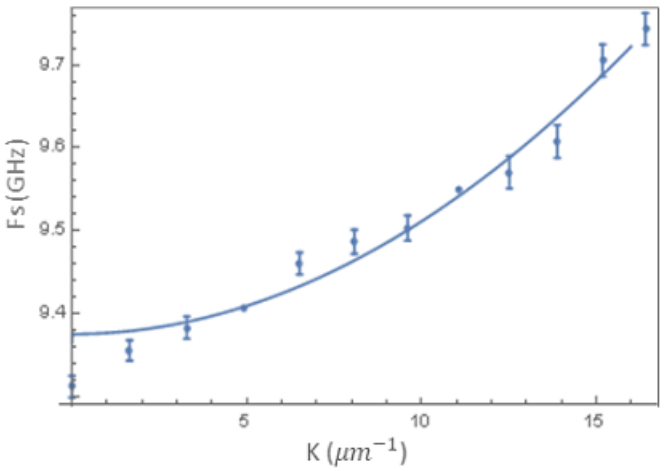

Figure 6.5: f_s vs k for 3nm Pt on 3nm $Co_{25}Fe_{75}$. Solid line is the fitting to equation 6.2

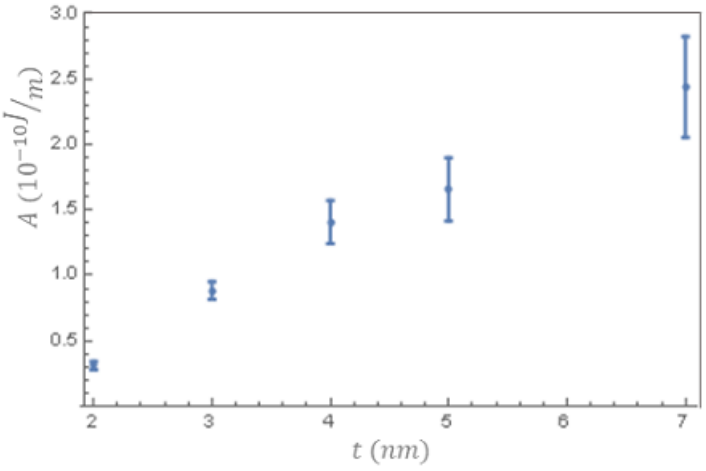

Figure 6.6: Exchange stiffness A for different thickness of 3nm Pt on $Co_{25}Fe_{75}$

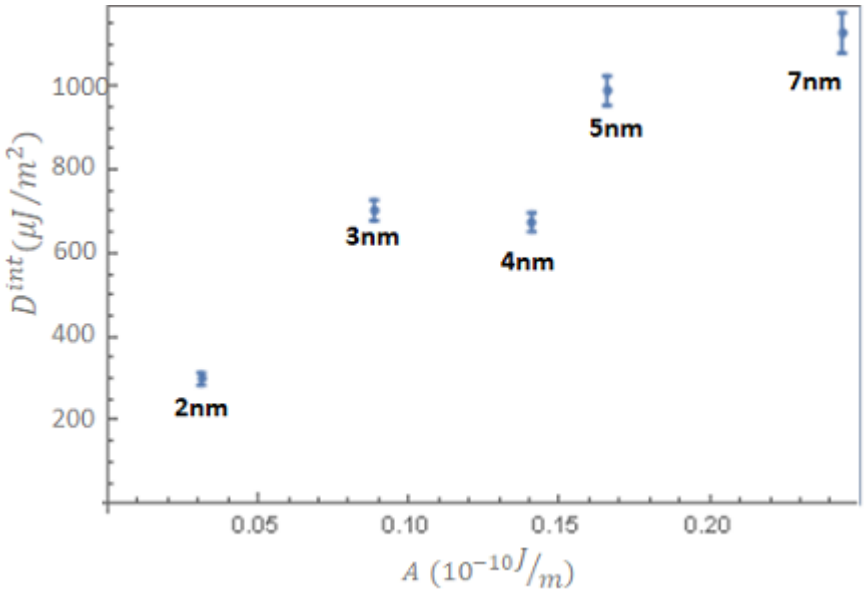

Figure 6.7: Exchange sitffness (A) vs D^{int} for different thickness of $Co_{25}Fe_{75}$ on 3nm Pt

The correlation between exchange and DMI has been previously observed [48]. In that case they were found to be linearly related. To test if this is the case in our material we must extract the interfacial component of the DMI. Since DMI should be interfacial and be proportional to 1/t, we can simply multiply our value by t and then rescale based on the lattice constant which is a natural length scale for the system. This definition follows that of [48] and yield

$$D^{int} = \frac{\sqrt{3}t}{a} \tag{6.3}$$

we can then compare D^{int} and A and look for a possible correlation.

we see in figure 6.7 that there is a strong correlation between D^{int} and A but that the relation is not quite linear. We can propose that the unusual thickness dependence of D can be explained by these changes in exchange stiffness. However, the behaviour of exchange stiffness itself is not yet explained. To look for a possible

explanation we begin to characterize different compositions of CoFe to see if this behaviour is replicated across different alloys or if it is specific to $Co_{25}Fe_{75}$.

6.4 Different Alloy

The first alternate alloy we looked at was $C0_{50}Fe_{50}$. According to ref. [153] the magnetic damping for this composition should be a factor of 4 worse than the alloy previously studied. We require a low damping to be able to perform BLS measurements, since we are attempting to measure small frequency differences between the Stokes and Anti-Stokes peaks. A large linewidth from a large damping will make precise determination of frequency impossible. Still, even with 4 times more damping a measurement should be feasible thanks to the ultra-low magnetic damping in the ideal alloy.

Unfortunately the reality for the epitaxial samples we study is different. The difference in damping as determined by FMR measurements is closer to an order of magnitude. The consequences for this on BLS measurements are twofold, not only does the linewidth increase making precise frequency determination a challenge, but it becomes difficult to maintain a good signal to noise ratio. Figure 6.8 compares two raw spectra, one for a 25/75 alloy and one from a 50/50 alloy.

Not only is the increase in linewidth apparent, but the signal-to-noise ratio is 3:1 for 50/50 versus 30:1 for 25/75, despite integrating for 6 times as long in the low damping case. Despite the difficulty presented by this composition an attempt was made at determining DMI in $Co_{50}Fe_{50}$ samples. An angular dependent measurement was made where each data point is the average of three 45 minute scans. Longer data taking time becomes impractical not only due to the demands on the experimental setup, but because of thermal drift affecting cavity alignment. The result can be seen in figure 6.9. Unfortunately the error is simply too large to make any statement on the nature of DMI in the system.

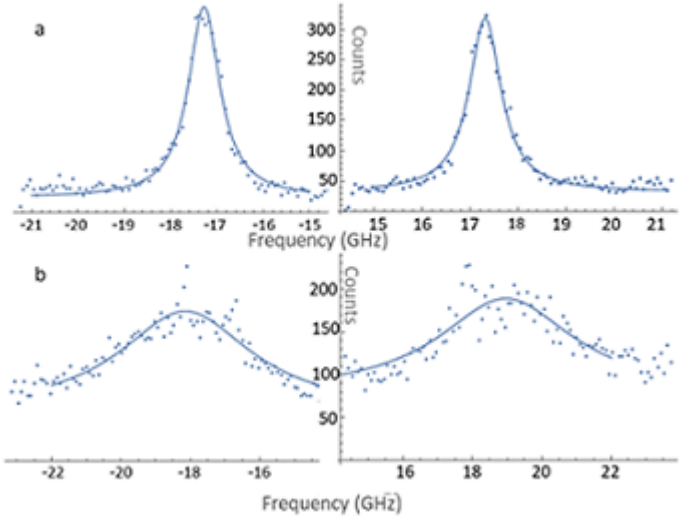

Figure 6.8: Raw Spectra comparison for 5nm 25/75 and 50/50 CoFe a) Spectrum for 25/75 CoFe at k = 0, 5 minute integration time. b) Spectrum for 50/50 CoFe at k 0, 30 minute integration time

Without information on DMI, and with such weak magnetic signal, we cannot make measurements of anisotropy or exchange to pursue our inquiry into the magnetic properties of CoFe alloys. The natural progression is to look at alloys closer to 25/75 in composition, which are predicted to have lower magnetic damping and therefore should be experimentally more viable. At time of publication however, these samples have not yet been fabricated due to challenges in designing custom targets.

6.5 Conclusions and Outlook

In conclusion, we have measured DMI for a series of epitaxially grown, low damping $Co_{25}Fe75/Pt$ samples varying the thickness of the ferromagnetic layer. We have seen an unexpected dependence on the thickness of the CoFe layer defying the 1/t dependence expected for an interfacial effect. In order to better understand this

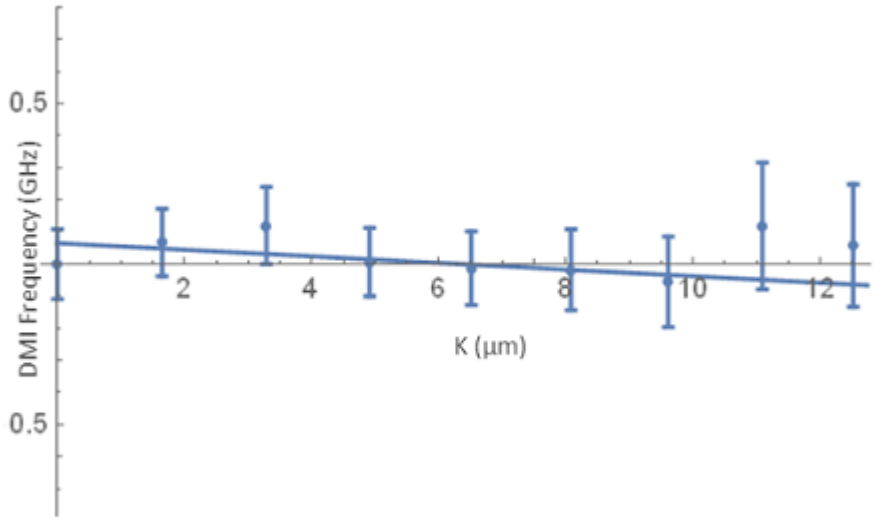

Figure 6.9: f_{DMI} vs k for 5nm thick $Co_{50}Fe_{50}$ on 4nm thick Pt

behaviour we have found anisotropy and exchange stiffness for all the samples. The unusual thickness dependence was found to originate in a change in exchange stiffness as the magnetic layer changes thickness. To elucidate this latter phenomenon samples with a changed CoFe composition were studied. Unfortunately, the magnetic damping proved too large in these new samples and no meaningful conclusions could be arrived at.

Nevetheless, these samples show strong DMI and low magnetic damping as well as some unusual physics. Therefore more study is required in order to better elucidate the underlying magnetic phenomena and to make the material suitable for applications in chiral spintronics.

Chapter 7

Conclusions

7.1 Summary of Work Completed

The research presented in this document seeks to better understand the properties of Ferromagnet/Heavy Metal bilayers to explore their use as possible building blocks for new computational techniques such as chiral spintronics or neuromorphic computing.

We first seek to explore the properties and uses of nanowire based Spin Torque Oscillators (STOs). We show that it is possible to make insulator based nanowire STOs by characterizing YIG wires grown directly on platinum. These wires not only were able to undergo auto-oscillations but also showed evidence of the Spin Seebeck effect reducing the required onset current. We see that these wires have larger magnetic damping than wires where the YIG is grown directly on GGG but that this increase in damping is compensated by an increased efficiency of the Spin Hall Effect. We then explored more detailed properties of nanowires with a metallic FM layer. In particular we showed that there exist two distinct oscillatory modes with very different behaviours. The modes are characterized by their physical location in the nanowire, being either on the edges or in the bulk of the wire. These edge and bulk modes were shown to have different onset currents

and different frequency behaviour as current is varied. The existence of distinct modes with differences in onset and tunable frequency difference is very promising for neuromorphic computing applications which require more complex behaviours from the devices.

Another requirement for the development of devices with more complex or more efficient computing capabilities is the discovery of new materials. Finding and characterizing materials with new or optimized properties is crucial to the advancement of computing technology. We present characterization of two new materials with potential for both Spin Torque applications and chiral structure based devices.

First we present a promising magnetic alloy $Pd_{25}Pt_{75}$ which combines a strong damping-like spin Orbit torque efficiency ($\xi_{dl} = 0.26$) with a low resistance ($\rho_{xx} = 57.5\mu\Omega cm$) and a tunable strength of the Dzyaloshinskii-Moriya interaction [34]. We show that this material is promising for energy efficient switching operations while having DMI strength tunable by a factor of 5 as composition of Pd_xPt_{1-x} is varied from x = 0 to x = 1. The tunable DMI strength enables the possibility of devices using this material for Skyrmionic or chiral domain wall applications.

Next we present an epitaxally grown, low damping material with significant DMI strength $Co_{25}Fe_{75}$. The low intrinsic damping makes the material promising for STO type applications and the strong DMI makes it promising for Skyrmionic applications and the epitaxial growth allows for the possibility of theoretical support and even lower damping. We note the unusual thickness dependence of DMI and begin exploring closely related alloys to better understand the magnetic properties of this material. So far only one other composition has been studied and it proved too difficult to extract much useful information from. However, by studying more alloys the unusual magnetic properties of this class of materials can be better understood and the possible applications can become clearer.

7.2 Works Published or Presented

The following is a list of works published or presented

- **K. Sobotkiewich**, A. Smith, K. Olsson, K. An, I. Krivorotov, X. Li, "Multiple Modes in a Nanowire Spin Torque Oscillator" (work ready for submission pending proofreading)

- H. Wu, J. Nance, S. Razavi, D. Lujan, B. Dai, Y. Liu, H. He, B. Cui, D. Wu, K. Wong, **K. Sobotkiewich**, X. Li, G. Carman (Submitted to Nature Electronics)

- L. Zhu, **K. Sobotkiewich**, X. Ma, X. Li, D. Ralph, R. Buhrman, "Strong Damping-Like Spin-Orbit Torque and Tunable DzyaloshinskiiMoriya Interaction Generated by Low-Resistivity Pd 1x Pt x Alloys", Advanced Functional Materials. **29**. 16 (2019)

- M. Evelt, C. Safranski, M. Aldosary, V.E Demidov, I. Barsukov, A.P Nosov, A.B Rinkevich, **K. Sobotkiewich**, X. Li, J. Shi, I. Krivorotov, S.O Demokritov, "Spin Hall-induced auto-oscillations in ultrathin YIG grown on Pt" Scientific Reports, **8**, 1 (2018)

- **K. Sobotkiewich**, A. Lee, X. Ma, K. Olsson, D. Lujan, A. Ahmed, F. Yang, X. Li, "Interfacial Dzyaloshinskii-Moriya interaction at an epitaxially grown ferromagnetic and heavy metal interface", Presented at the APS March Meeting, Boston, March 8 2019

- **K. Sobotkiewich**, A. Smith, K. An, X. Ma, K. Olsson, E. Montoya, I. Krivorotov, X. Li, "Nanowire spin Hall oscillators: width dependence and spatial mapping", Presented at the APS March Meeting, New Orleans, March 17, 2017

Bibliography

[1] G. Binasch, P. Grünberg, F. Saurenbach, and W. Zinn, "Enhanced magnetoresistance in layered magnetic structures with antiferromagnetic interlayer exchange," *Physical Review B*, vol. 39, pp. 4828–4830, 3 1989.

[2] M. N. Baibich, J. M. Broto, A. Fert, F. N. Van Dau, F. Petroff, P. Etienne, G. Creuzet, A. Friederich, and J. Chazelas, "Giant Magnetoresistance of (001)Fe/(001)Cr Magnetic Superlattices," *Physical Review Letters*, vol. 61, pp. 2472–2475, 11 1988.

[3] J. C. Slonczewski, "Current-driven excitation of magnetic multilayers," *Journal of Magnetism and Magnetic Materials*, vol. 159, no. 1, pp. L1–L7, 1996.

[4] M. Tsoi, A. G. M. Jansen, J. Bass, W.-C. Chiang, M. Seck, V. Tsoi, and P. Wyder, "Excitation of a Magnetic Multilayer by an Electric Current," *Physical Review Letters*, vol. 80, pp. 4281–4284, 5 1998.

[5] V. E. Demidov, S. Urazhdin, H. Ulrichs, V. Tiberkevich, A. Slavin, D. Baither, G. Schmitz, and S. O. Demokritov, "Magnetic nano-oscillator driven by pure spin current," *Nature Materials*, vol. 11, no. 12, pp. 1028–1031, 2012.

[6] T. Chen, R. K. Dumas, A. Eklund, P. K. Muduli, A. Houshang, A. A. Awad, P. Dürrenfeld, B. G. Malm, A. Rusu, and J. Akerman, "Spin-Torque and Spin-

Hall Nano-Oscillators," *Proceedings of the IEEE*, vol. 104, no. 10, pp. 1919–1945, 2016.

[7] V. E. Demidov, S. Urazhdin, G. de Loubens, O. Klein, V. Cros, A. Anane, and S. O. Demokritov, "Magnetization oscillations and waves driven by pure spin currents," *Physics Reports*, vol. 673, pp. 1–31, 2017.

[8] J. Torrejon, M. Riou, F. A. Araujo, S. Tsunegi, G. Khalsa, D. Querlioz, P. Bortolotti, V. Cros, K. Yakushiji, A. Fukushima, H. Kubota, S. Yuasa, M. D. Stiles, and J. Grollier, "Neuromorphic computing with nanoscale spintronic oscillators," *Nature*, vol. 547, p. 428, 7 2017.

[9] K. Uchida, S. Takahashi, K. Harii, J. Ieda, W. Koshibae, K. Ando, S. Maekawa, and E. Saitoh, "Observation of the spin Seebeck effect," *Nature*, vol. 455, pp. 778–781, 10 2008.

[10] H. Adachi, K. I. Uchida, E. Saitoh, and S. Maekawa, "Theory of the spin Seebeck effect," *Reports on Progress in Physics*, vol. 76, 3 2013.

[11] S. Emori, U. Bauer, S.-M. Ahn, E. Martinez, and G. S. D. Beach, "Current-driven dynamics of chiral ferromagnetic domain walls," *Nature Materials*, vol. 12, p. 611, 6 2013.

[12] S. Emori and G. S. D. Beach, "Enhanced current-induced domain wall motion by tuning perpendicular magnetic anisotropy," *Applied Physics Letters*, vol. 98, p. 132508, 3 2011.

[13] J. Torrejon and M. Hayashi, "10 - Spin Hall torquedriven chiral domain walls in magnetic heterostructures," in *Woodhead Publishing Series in Electronic and Optical Materials* (M. B. T. M. N. Vázquez and Microwires, eds.), pp. 313–331, Woodhead Publishing, 2015.

[14] G. Chen, S. P. Kang, C. Ophus, A. T. NDiaye, H. Y. Kwon, R. T. Qiu, C. Won, K. Liu, Y. Wu, and A. K. Schmid, "Out-of-plane chiral domain wall spin-structures in ultrathin in-plane magnets," *Nature Communications*, vol. 8, p. 15302, 5 2017.

[15] P. C. Filippou, J. Jeong, Y. Ferrante, S.-H. Yang, T. Topuria, M. G. Samant, and S. S. P. Parkin, "Chiral domain wall motion in unit-cell thick perpendicularly magnetized Heusler films prepared by chemical templating," *Nature Communications*, vol. 9, no. 1, p. 4653, 2018.

[16] A. Fert, N. Reyren, and V. Cros, "Magnetic skyrmions: Advances in physics and potential applications," *Nature Reviews Materials*, vol. 2, p. 17031, 2017.

[17] F. Büttner, I. Lemesh, and G. S. Beach, "Theory of isolated magnetic skyrmions: From fundamentals to room temperature applications," *Scientific Reports*, vol. 8, no. 1, p. 4464, 2018.

[18] D. D. Stancil and A. Prabhakar, *Spin Waves: Theory and Applications*. New York: Springer, 2009.

[19] R. C. O'Handley, *Modern Magnetic Materials: Principles and Applications*. New York: John Wiley.

[20] S. Foner, "Versatile and Sensitive VibratingSample Magnetometer," *Review of Scientific Instruments*, vol. 30, pp. 548–557, 7 1959.

[21] R. C. Jaklevic, J. Lambe, A. H. Silver, and J. E. Mercereau, "Quantum Interference Effects in Josephson Tunneling," *Physical Review Letters*, vol. 12, pp. 159–160, 2 1964.

[22] P. W. Anderson and J. M. Rowell, "Probable Observation of the Josephson Superconducting Tunneling Effect," *Physical Review Letters*, vol. 10, pp. 230–232, 3 1963.

[23] J. D. Jackson 1925-2016, *Classical electrodynamics*. Third edition. New York : Wiley, [1999] ©1999.

[24] J. E. Hirsch, "Spin hall effect," *Physical Review Letters*, vol. 83, no. 9, pp. 1834–1837, 1999.

[25] Y. K. Kato, R. C. Myers, A. C. Gossard, and D. D. Awschalom, "Observation of the Spin Hall," *Science*, vol. 306, no. December, pp. 1910–1913, 2004.

[26] J. Sinova, S. O. Valenzuela, J. Wunderlich, C. H. Back, and T. Jungwirth, "Spin Hall effects," *Reviews of Modern Physics*, vol. 87, no. 4, pp. 1213–1260, 2015.

[27] Y. Kajiwara, K. Harii, S. Takahashi, J. Ohe, K. Uchida, M. Mizuguchi, H. Umezawa, H. Kawai, K. Ando, K. Takanashi, S. Maekawa, and E. Saitoh, "No Title," *Nature*, vol. 464, p. 262, 2010.

[28] A. A. Awad, P. Dürrenfeld, A. Houshang, M. Dvornik, E. Iacocca, R. K. Dumas, and J. Åkerman, "Long-range mutual synchronization of spin Hall nano-oscillators," *Nature Physics*, vol. 13, no. 3, pp. 292–299, 2017.

[29] H.-H. Chen, C.-M. Lee, J.-C. Wu, L. Horng, C.-R. Chang, and J.-H. Chang, "Synchronization of spin torque nano-oscillators through dipolar interactions," *Journal of Applied Physics*, vol. 115, p. 134306, 4 2014.

[30] S. Tsunegi, T. Taniguchi, R. Lebrun, K. Yakushiji, V. Cros, J. Grollier, A. Fukushima, S. Yuasa, and H. Kubota, "Scaling up electrically synchronized spin torque oscillator networks," *Scientific Reports*, vol. 8, no. 1, p. 13475, 2018.

[31] R. Lebrun, S. Tsunegi, P. Bortolotti, H. Kubota, A. S. Jenkins, M. Romera, K. Yakushiji, A. Fukushima, J. Grollier, S. Yuasa, and V. Cros, "Mutual syn-

chronization of spin torque nano-oscillators through a long-range and tunable electrical coupling scheme," *Nature Communications*, vol. 8, p. 15825, 6 2017.

[32] H. Singh, S. Bhuktare, A. Bose, A. Fukushima, K. Yakushiji, S. Yuasa, H. Kubota, and A. A. Tulapurkar, "Mutual Synchronization of Spin-Torque Nano-Oscillators Via Oersted Magnetic Fields Created by Waveguides," *Physical Review Applied*, vol. 11, p. 54028, 5 2019.

[33] T. Taniguchi, "Synchronization of spin-torque oscillators via spin pumping," *AIP Advances*, vol. 9, p. 35310, 3 2019.

[34] L. Zhu, K. Sobotkiewich, X. Ma, X. Li, D. C. Ralph, and R. A. Buhrman, "Strong Damping-Like Spin-Orbit Torque and Tunable DzyaloshinskiiMoriya Interaction Generated by Low-Resistivity Pd 1x Pt x Alloys," *Advanced Functional Materials*, vol. 29, 4 2019.

[35] A. J. Lee, J. T. Brangham, Y. Cheng, S. P. White, W. T. Ruane, B. D. Esser, D. W. McComb, P. C. Hammel, and F. Yang, "Metallic ferromagnetic films with magnetic damping under 1.4103," *Nature Communications*, vol. 8, no. 1, p. 234, 2017.

[36] C. Safranski, I. Barsukov, H. K. Lee, T. Schneider, A. A. Jara, A. Smith, H. Chang, K. Lenz, J. Lindner, Y. Tserkovnyak, M. Wu, and I. N. Krivorotov, "Spin caloritronic nano-oscillator," *Nature Communications*, vol. 8, no. 1, p. 117, 2017.

[37] M. Evelt, C. Safranski, M. Aldosary, V. E. Demidov, I. Barsukov, A. P. Nosov, A. B. Rinkevich, K. Sobotkiewich, X. Li, J. Shi, I. N. Krivorotov, and S. O. Demokritov, "Spin Hall-induced auto-oscillations in ultrathin YIG grown on Pt," *Scientific Reports*, vol. 8, no. 1, p. 1269, 2018.

[38] G. Buzsaki, *Rythms of the Brain*. USA: Oxford University Press, 2006.

[39] I. E. Dzyaloshinsky, "Thermodynamic Theory of "Weak" Ferromagnetism In Antiferromagnetic Substances," *Soviet Physics JETP*, vol. 5, no. 6, pp. 1259–1272, 1957.

[40] T. Moriya, "Critical Fields of Superconducting Sn, In, and Ta," *Physical Review*, vol. 120, no. 1, pp. 91–98, 1960.

[41] A. Fert and P. M. Levy, "Role of Anisotropic Exchange Interactions in Determining the Properties of Spin-Glasses," *Physical Review Letters*, vol. 44, no. 23, p. 1538, 1980.

[42] A. Crépieux and C. Lacroix, "Dzyaloshinsky-Moriya interactions induced by symmetry breaking at a surface," *Journal of Magnetism and Magnetic Materials*, vol. 182, pp. 341–349, 3 1998.

[43] H. Yang, A. Thiaville, S. Rohart, A. Fert, and M. Chshiev, "Anatomy of Dzyaloshinskii-Moriya Interaction at Co/Pt Interfaces," *Physical Review Letters*, vol. 115, no. 26, p. 267210, 2015.

[44] J. Cho, N.-H. Kim, S. Lee, J.-S. Kim, R. Lavrijsen, A. Solignac, Y. Yin, D.-S. Han, N. J. J. van Hoof, H. J. M. Swagten, B. Koopmans, and C.-Y. You, "Thickness dependence of the interfacial DzyaloshinskiiMoriya interaction in inversion symmetry broken systems," *Nature Communications*, vol. 6, p. 7635, 7 2015.

[45] A. K. Chaurasiya, A. Kumar, R. Gupta, S. Chaudhary, P. K. Muduli, and A. Barman, "Direct observation of unusual interfacial Dzyaloshinskii-Moriya interaction in graphene/NiFe/Ta heterostructures," *Physical Review B*, vol. 99, p. 35402, 1 2019.

[46] X. Ma, G. Yu, X. Li, T. Wang, D. Wu, K. S. Olsson, Z. Chu, K. An, J. Q. Xiao, K. L. Wang, and X. Li, "Interfacial control of Dzyaloshinskii-Moriya

interaction in heavy metal/ferromagnetic metal thin film heterostructures," *Physical Review B*, vol. 94, no. 18, p. 180408(R), 2016.

[47] X. Ma, G. Yu, S. A. Razavi, S. S. Sasaki, X. Li, K. Hao, S. H. Tolbert, K. L. Wang, and X. Li, "Dzyaloshinskii-Moriya Interaction across an Antiferromagnet-Ferromagnet Interface," *Physical Review Letters*, vol. 119, no. 2, p. 027202, 2017.

[48] H. T. Nembach, J. M. Shaw, M. Weiler, E. Jué, and T. J. Silva, "Linear relation between Heisenberg exchange and interfacial Dzyaloshinskii-Moriya interaction in metal films," *Nature Physics*, vol. 11, no. 10, pp. 825–829, 2015.

[49] M. Belmeguenai, Y. Roussigné, H. Bouloussa, S. Chérif, A. Stashkevich, M. Nasui, M. Gabor, A. Mora-Hernández, B. Nicholson, O.-O. Inyang, A. Hindmarch, and L. Bouchenoire, "Thickness Dependence of the Dzyaloshinskii-Moriya Interaction in ${\mathrm{Co}}_{2}\mathrm{FeAl}$ Ultrathin Films: Effects of Annealing Temperature and Heavy-Metal Material," *Physical Review Applied*, vol. 9, p. 44044, 4 2018.

[50] S. Tacchi, R. E. Troncoso, M. Ahlberg, G. Gubbiotti, M. Madami, J. Åkerman, and P. Landeros, "Interfacial Dzyaloshinskii-Moriya Interaction in Pt/CoFeB Films: Effect of the Heavy-Metal Thickness," *Physical Review Letters*, vol. 118, no. 14, p. 147201, 2017.

[51] X. Ma, G. Yu, C. Tang, X. Li, C. He, J. Shi, K. L. Wang, and X. Li, "Interfacial Dzyaloshinskii-Moriya Interaction: Effect of 5d Band Filling and Correlation with Spin Mixing Conductance," *Physical Review Letters*, vol. 120, no. 15, p. 157204, 2018.

[52] G. Bihlmayer, O. Rader, and R. Winkler, "Focus on the Rashba effect," *New Journal of Physics*, vol. 17, no. 5, 2015.

[53] A. Kundu and S. Zhang, "Dzyaloshinskii-Moriya interaction mediated by spin-polarized band with Rashba spin-orbit coupling," *Physical Review B - Condensed Matter and Materials Physics*, vol. 92, no. 9, p. 094434, 2015.

[54] H. Yang, G. Chen, A. A. Cotta, A. T. N'DIaye, S. A. Nikolaev, E. A. Soares, W. A. MacEdo, K. Liu, A. K. Schmid, A. Fert, and M. Chshiev, "Significant Dzyaloshinskii-Moriya interaction at graphene-ferromagnet interfaces due to the Rashba effect," *Nature Materials*, vol. 17, no. 7, pp. 605–609, 2018.

[55] J. H. Moon, S. M. Seo, K. J. Lee, K. W. Kim, J. Ryu, H. W. Lee, R. D. McMichael, and M. D. Stiles, "Spin-wave propagation in the presence of interfacial Dzyaloshinskii-Moriya interaction," *Physical Review B - Condensed Matter and Materials Physics*, vol. 88, no. 18, p. 184404, 2013.

[56] W. Jiang, P. Upadhyaya, W. Zhang, G. Yu, M. B. Jungfleisch, F. Y. Fradin, J. E. Pearson, Y. Tserkovnyak, K. L. Wang, O. Heinonen, S. G. E. Te Velthuis, and A. Hoffmann, "Blowing magnetic skyrmion bubbles Downloaded from," *Science*, vol. 349, no. 6245, pp. 283–286, 2015.

[57] G. Yu, P. Upadhyaya, X. Li, W. Li, S. K. Kim, Y. Fan, K. L. Wong, Y. Tserkovnyak, P. K. Amiri, and K. L. Wang, "Room-Temperature Creation and Spin-Orbit Torque Manipulation of Skyrmions in Thin Films with Engineered Asymmetry," *Nano Letters*, vol. 16, no. 3, pp. 1981–1988, 2016.

[58] J. Sampaio, V. Cros, S. Rohart, A. Thiaville, and A. Fert, "Nucleation, stability and current-induced motion of isolated magnetic skyrmions in nanostructures," *Nature Nanotechnology*, vol. 8, no. 11, pp. 839–844, 2013.

[59] F. Jonietz, S. Mühlbauer, C. Pfleiderer, A. Neubauer, W. Münzer, A. Bauer, T. Adams, R. Georgii, P. Böni, R. A. Duine, K. Everschor, M. Garst, and

A. Rosch, "Spin Transfer Torques in MnSi," *Science*, vol. 330, no. September, p. 1684, 2011.

[60] X. Z. Yu, N. Kanazawa, W. Z. Zhang, T. Nagai, T. Hara, K. Kimoto, Y. Matsui, Y. Onose, and Y. Tokura, "Skyrmion flow near room temperature in an ultralow current density," *Nature Communications*, vol. 3, p. 988, 8 2012.

[61] J. R. Sandercock, "Trends in brillouin scattering: Studies of opaque materials, supported films, and central modes," *Light Scattering in Solids III*, vol. 51, pp. 173–206, 1982.

[62] K. Shahbazi, J. V. Kim, H. T. Nembach, J. M. Shaw, A. Bischof, M. D. Rossell, V. Jeudy, T. A. Moore, and C. H. Marrows, "Domain-wall motion and interfacial Dzyaloshinskii-Moriya interactions in Pt/Co/Ir(tIr)/Ta multilayers," *Physical Review B*, vol. 99, no. 9, p. 094409, 2019.

[63] D. H. Kim, S. C. Yoo, D. Y. Kim, B. C. Min, and S. B. Choe, "Wide-Range Probing of Dzyaloshinskii-Moriya Interaction," *Scientific Reports*, vol. 7, p. 45498, 2017.

[64] H. S. Körner, J. Stigloher, H. G. Bauer, H. Hata, T. Taniguchi, T. Moriyama, T. Ono, and C. H. Back, "Interfacial Dzyaloshinskii-Moriya interaction studied by time-resolved scanning Kerr microscopy," *Physical Review B - Condensed Matter and Materials Physics*, vol. 92, no. 22, p. 220413(R), 2015.

[65] I. Gross, L. J. Martínez, J. P. Tetienne, T. Hingant, J. F. Roch, K. Garcia, R. Soucaille, J. P. Adam, J. V. Kim, S. Rohart, A. Thiaville, J. Torrejon, M. Hayashi, and V. Jacques, "Direct measurement of interfacial Dzyaloshinskii-Moriya interaction in X—CoFeB—MgO heterostructures with a scanning NV magnetometer (X=Ta,TaN, and W) DIRECT MEASURE-

MENT of INTERFACIAL ... I. GROSS et al.," *Physical Review B*, vol. 94, no. 6, p. 064413, 2016.

[66] W. Jiang, S. Zhang, X. Wang, C. Phatak, Q. Wang, W. Zhang, M. B. Jungfleisch, J. E. Pearson, Y. Liu, J. Zang, X. Cheng, A. Petford-Long, A. Hoffmann, and S. G. Te Velthuis, "Quantifying chiral exchange interaction for Néel-type skyrmions via Lorentz transmission electron microscopy," *Physical Review B*, vol. 99, no. 10, p. 104402, 2019.

[67] D. S. Han, N. H. Kim, J. S. Kim, Y. Yin, J. W. Koo, J. Cho, S. Lee, M. Kläui, H. J. Swagten, B. Koopmans, and C. Y. You, "Asymmetric hysteresis for probing Dzyaloshinskii-Moriya interaction," *Nano Letters*, vol. 16, no. 7, pp. 4438–4446, 2016.

[68] L. Liu, C. F. Pai, D. C. Ralph, and R. A. Buhrman, "Magnetic oscillations driven by the spin hall effect in 3-terminal magnetic tunnel junction devices," *Physical Review Letters*, vol. 109, no. 18, p. 186602, 2012.

[69] R. H. Liu, W. L. Lim, and S. Urazhdin, "Spectral characteristics of the microwave emission by the spin hall nano-oscillator," *Physical Review Letters*, vol. 110, no. 14, p. 147601, 2013.

[70] V. E. Demidov, S. Urazhdin, A. Zholud, A. Sadovnikov, and S. O. Demokritov, "Nanoconstriction-based spin-Hall oscillators," *Appl. Phys. Lett.*, vol. 105, no. 17, p. 172410, 2014.

[71] Z. Duan, A. Smith, L. Yang, B. Youngblood, J. Lindner, V. E. Demidov, S. O. Demokritov, and I. N. Krivorotov, "Nanowire spin torque oscillator driven by spin orbit torques," *Nature Communications*, vol. 5, p. 5616, 2014.

[72] V. E. Demidov, S. Urazhdin, A. Zholud, A. V. Sadovnikov, A. N. Slavin,

and S. O. Demokritov, "Spin-current nano-oscillator based on nonlocal spin injection," *Scientific Reports*, vol. 5, p. 8578, 2 2015.

[73] V. E. Demidov, S. Urazhdin, R. Liu, B. Divinskiy, A. Telegin, and S. O. Demokritov, "Excitation of coherent propagating spin waves by pure spin currents," *Nature Communications*, vol. 7, p. 10446, 1 2016.

[74] M. Collet, X. De Milly, O. D'Allivy Kelly, V. V. Naletov, R. Bernard, P. Bortolotti, J. Ben Youssef, V. E. Demidov, S. O. Demokritov, J. L. Prieto, M. Muñoz, V. Cros, A. Anane, G. De Loubens, and O. Klein, "Generation of coherent spin-wave modes in yttrium iron garnet microdiscs by spin-orbit torque," *Nature Communications*, vol. 7, p. 10377, 2016.

[75] V. E. Demidov, M. Evelt, V. Bessonov, S. O. Demokritov, J. L. Prieto, M. Muñoz, J. Ben Youssef, V. V. Naletov, G. de Loubens, O. Klein, M. Collet, P. Bortolotti, V. Cros, and A. Anane, "Direct observation of dynamic modes excited in a magnetic insulator by pure spin current," *Scientific Reports*, vol. 6, p. 32781, 9 2016.

[76] Y. Sun, Y.-Y. Song, H. Chang, M. Kabatek, M. Jantz, W. Schneider, M. Wu, H. Schultheiss, and A. Hoffmann, "Growth and ferromagnetic resonance properties of nanometer-thick yttrium iron garnet films," *Applied Physics Letters*, vol. 101, p. 152405, 10 2012.

[77] C. Hahn, G. de Loubens, O. Klein, M. Viret, V. V. Naletov, and J. Ben Youssef, "Comparative measurements of inverse spin Hall effects and magnetoresistance in YIG/Pt and YIG/Ta," *Phys. Rev. B*, vol. 87, p. 174417, 5 2013.

[78] C. Tang, P. Sellappan, Y. Liu, Y. Xu, J. E. Garay, and J. Shi, "No Title," *Phys. Rev. B*, vol. 94, p. 140403(R), 2016.

[79] C. Hauser, T. Richter, N. Homonnay, C. Eisenschmidt, M. Qaid, H. Deniz, D. Hesse, M. Sawicki, S. G. Ebbinghaus, and G. Schmidt, "Yttrium Iron Garnet Thin Films with Very Low Damping Obtained by Recrystallization of Amorphous Material," *Scientific Reports*, vol. 6, p. 20827, 2 2016.

[80] M. Aldosary, J. Li, C. Tang, Y. Xu, J.-G. Zheng, K. N. Bozhilov, and J. Shi, "Platinum/yttrium iron garnet inverted structures for spin current transport," *Applied Physics Letters*, vol. 108, no. 24, p. 242401, 2016.

[81] O. d'Allivy Kelly, A. Anane, R. Bernard, J. Ben Youssef, C. Hahn, A. H. Molpeceres, C. Carrétéro, E. Jacquet, C. Deranlot, P. Bortolotti, R. Lebourgeois, J.-C. Mage, G. de Loubens, O. Klein, V. Cros, and A. Fert, "Inverse spin Hall effect in nanometer-thick yttrium iron garnet/Pt system," *Applied Physics Letters*, vol. 103, p. 82408, 8 2013.

[82] P. Che, Y. Zhang, C. Liu, S. Tu, Z. Liao, D. Yu, F. A. Vetro, J. Ansermet, W. Zhao, L. Bi, and H. Yu, "Short-Wavelength Spin Waves in Yttrium Iron Garnet Micro-Channels on Silicon," *IEEE Magnetics Letters*, vol. 7, pp. 1–4, 2016.

[83] M. Dyakonov and V. I. Perel, *Possibility of Orienting Electron Spins with Current*, vol. 13. 5 1971.

[84] J. Li, Y. Xu, M. Aldosary, C. Tang, Z. Lin, S. Zhang, R. Lake, and J. Shi, "Observation of magnon-mediated current drag in Pt/yttrium iron garnet/Pt(Ta) trilayers," *Nature Communications*, vol. 7, p. 10858, 3 2016.

[85] L. Berger, "Emission of spin waves by a magnetic multilayer traversed by a current," *Phys. Rev. B*, vol. 54, no. 13, pp. 9353–9358, 1996.

[86] K. Ando, S. Takahashi, K. Harii, K. Sasage, J. Ieda, S. Maekawa, and

E. Saitoh, "Electric Manipulation of Spin Relaxation Using the Spin Hall Effect," *Phys. Rev. Lett.*, vol. 101, p. 36601, 7 2008.

[87] V. E. Demidov, S. Urazhdin, E. R. J. Edwards, and S. O. Demokritov, "Wide-range control of ferromagnetic resonance by spin Hall effect," *Applied Physics Letters*, vol. 99, p. 172501, 10 2011.

[88] A. Slavin and V. Tiberkevich, "Nonlinear auto-oscillator theory of microwave generation by spin-polarized current," *IEEE Transactions on Magnetics*, vol. 45, no. 4, pp. 1875–1918, 2009.

[89] N. Locatelli, V. Cros, and J. Grollier, "Spin-torque building blocks," *Nature Materials*, vol. 13, pp. 11–20, 2014.

[90] R. Sharma, N. Sisodia, E. Iacocca, A. A. Awad, J. Åkerman, and P. K. Muduli, "A high-speed single sideband generator using a magnetic tunnel junction spin torque nano-oscillator," *Scientific Reports*, vol. 7, no. 1, p. 13422, 2017.

[91] S. Miwa, S. Ishibashi, H. Tomita, T. Nozaki, E. Tamura, K. Ando, N. Mizuochi, T. Saruya, H. Kubota, K. Yakushiji, T. Taniguchi, H. Imamura, A. Fukushima, S. Yuasa, and Y. Suzuki, "Highly sensitive nanoscale spin-torque diode," *Nature Materials*, vol. 13, no. 1, pp. 50–56, 2014.

[92] A. Haldar, C. Tian, and A. O. Adeyeye, "Isotropic transmission of magnon spin information without a magnetic field," *Science Advances*, vol. 3, no. 7, p. e1700638, 2017.

[93] J. C. Slonczewski, "Current-driven excitation of magnetic multilayers," *Journal of Magnetism and Magnetic Materials*, vol. 159, no. 1, pp. L1–L7, 1996.

[94] M. Collet, O. Gladii, M. Evelt, V. Bessonov, L. Soumah, P. Bortolotti, S. O. Demokritov, Y. Henry, V. Cros, M. Bailleul, V. E. Demidov, and A. Anane,

"Spin-wave propagation in ultra-thin YIG based waveguides," *Applied Physics Letters*, vol. 110, no. 9, p. 92408, 2017.

[95] D. C. Ralph and M. D. Stiles, "Spin transfer torques," *Journal of Magnetism and Magnetic Materials*, vol. 320, no. 7, pp. 1190–1216, 2008.

[96] S. Urazhdin, V. E. Demidov, H. Ulrichs, T. Kendziorczyk, T. Kuhn, J. Leuthold, G. Wilde, and S. O. Demokritov, "Nanomagnonic devices based on the spin-transfer torque," *Nature Nanotechnology*, vol. 9, no. 7, pp. 509–513, 2014.

[97] A. Slavin, "Microwave sources: Spin-torque oscillators get in phase," *Nature Nanotechnology*, vol. 4, no. 8, pp. 479–480, 2009.

[98] M. Ranjbar, P. Dürrenfeld, M. Haidar, E. Iacocca, M. Balinskiy, T. Q. Le, M. Fazlali, A. Houshang, A. A. Awad, R. K. Dumas, and J. Åkerman, "CoFeB-based spin Hall nano-oscillators," *IEEE Magnetics Letters*, vol. 5, pp. 1–4, 2014.

[99] S. Langenfeld, V. Tshitoyan, Z. Fang, A. Wells, T. A. Moore, and A. J. Ferguson, "Exchange magnon induced resistance asymmetry in permalloy spin-Hall oscillators," *Applied Physics Letters*, vol. 108, no. 19, p. 192402, 2016.

[100] T. Kendziorczyk and T. Kuhn, "Mutual synchronization of nanoconstriction-based spin Hall nano-oscillators through evanescent and propagating spin waves," *Physical Review B*, vol. 93, no. 13, p. 134413, 2016.

[101] W. H. Rippard, M. R. Pufall, S. Kaka, S. E. Russek, and T. J. Silva, "Direct-Current Induced Dynamics in Co(90)Fe(10)/Ni(80)Fe(20) Point Contacts," *Physical Review Letters*, vol. 92, no. 2, p. 027201, 2004.

[102] T. J. Silva and W. H. Rippard, "Developments in nano-oscillators based upon

spin-transfer point-contact devices," *Journal of Magnetism and Magnetic Materials*, vol. 320, no. 7, pp. 1260–1271, 2008.

[103] K. Wagner, A. Smith, T. Hache, J.-R. Chen, L. Yang, E. Montoya, K. Schultheiss, J. Lindner, J. Fassbender, I. Krivorotov, and H. Schultheiss, "Injection locking of multiple auto-oscillation modes in a tapered nanowire spin Hall oscillator," *Nat. Nanotechnol.*, vol. 11, p. 432, 2018.

[104] K. Song and K.-J. Lee, "Spin-transfer-torque efficiency enhanced by edge-damage of perpendicular magnetic random access memories," *Journal of Applied Physics*, vol. 118, p. 53912, 8 2015.

[105] A. Slavin and V. Tiberkevich, "Nonlinear Auto-Oscillator Theory of Microwave Generation by Spin-Polarized Current," *IEEE Transactions on Magnetics*, vol. 45, no. 4, pp. 1875–1918, 2009.

[106] M. Dvornik and J. Åkerman, "Anomalous nonlinearity of the magnonic edge mode," *arxiv*, vol. 1804.01585, 2018.

[107] Y. Wu, M. Elyasi, X. Qiu, M. Chen, Y. Liu, L. Ke, and H. Yang, "High-Performance THz Emitters Based on Ferromagnetic/Nonmagnetic Heterostructures," *Advanced Materials*, vol. 29, p. 1603031, 1 2017.

[108] P. P. J. Haazen, E. Murè, J. H. Franken, R. Lavrijsen, H. J. M. Swagten, and B. Koopmans, "Domain wall depinning governed by the spinHalleffect," *Nature Materials*, vol. 12, p. 299, 2 2013.

[109] O. J. Lee, L. Q. Liu, C. F. Pai, Y. Li, H. W. Tseng, P. G. Gowtham, J. P. Park, D. C. Ralph, and R. A. Buhrman, "Central role of domain wall depinning for perpendicular magnetization switching driven by spin torque from the spin Hall effect," *Phys. Rev. B*, vol. 89, p. 24418, 1 2014.

[110] S. Shi, Y. Ou, S. V. Aradhya, D. C. Ralph, and R. A. Buhrman, "Fast Low-Current Spin-Orbit-Torque Switching of Magnetic Tunnel Junctions through Atomic Modifications of the Free-Layer Interfaces," *Phys. Rev. Applied*, vol. 9, p. 11002, 1 2018.

[111] C.-F. Pai, L. Liu, Y. Li, H. W. Tseng, D. C. Ralph, and R. A. Buhrman, "Spin transfer torque devices utilizing the giant spin Hall effect of tungsten," *Applied Physics Letters*, vol. 101, p. 122404, 9 2012.

[112] J. Han, A. Richardella, S. A. Siddiqui, J. Finley, N. Samarth, and L. Liu, "Room-Temperature Spin-Orbit Torque Switching Induced by a Topological Insulator," *Phys. Rev. Lett.*, vol. 119, p. 77702, 8 2017.

[113] A. R. Mellnik, J. S. Lee, A. Richardella, J. L. Grab, P. J. Mintun, M. H. Fischer, A. Vaezi, A. Manchon, E.-A. Kim, N. Samarth, and D. C. Ralph, "Spin-transfer torque generated by a topological insulator," *Nature*, vol. 511, p. 449, 7 2014.

[114] L. Liu, T. Moriyama, D. C. Ralph, and R. A. Buhrman, "Spin-Torque Ferromagnetic Resonance Induced by the Spin Hall Effect," *Physical Review Letters*, vol. 106, p. 36601, 1 2011.

[115] M. DC, R. Grassi, J.-Y. Chen, M. Jamali, D. Reifsnyder Hickey, D. Zhang, Z. Zhao, H. Li, P. Quarterman, Y. Lv, M. Li, A. Manchon, K. A. Mkhoyan, T. Low, and J.-P. Wang, "Room-temperature high spinorbit torque due to quantum confinement in sputtered BixSe(1x) films," *Nature Materials*, vol. 17, no. 9, pp. 800–807, 2018.

[116] G. E. Rowlands, S. V. Aradhya, S. Shi, E. H. Yandel, J. Oh, D. C. Ralph, and R. A. Buhrman, "Nanosecond magnetization dynamics during spin Hall

switching of in-plane magnetic tunnel junctions," *Applied Physics Letters*, vol. 110, p. 122402, 3 2017.

[117] M. Cubukcu, J. Sampaio, K. Bouzehouane, D. Apalkov, A. V. Khvalkovskiy, V. Cros, and N. Reyren, "Dzyaloshinskii-Moriya anisotropy in nanomagnets with in-plane magnetization," *Phys. Rev. B*, vol. 93, p. 20401, 1 2016.

[118] E. Sagasta, Y. Omori, M. Isasa, M. Gradhand, L. E. Hueso, Y. Niimi, Y. Otani, and F. Casanova, "Tuning the spin Hall effect of Pt from the moderately dirty to the superclean regime," *Phys. Rev. B*, vol. 94, p. 60412, 8 2016.

[119] L. Zhu, D. C. Ralph, and R. A. Buhrman, "Highly Efficient Spin-Current Generation by the Spin Hall Effect in ${\mathrm{Au}}_{1\ensuremath{-}x}{\mathrm{Pt}}_{x}$," *Phys. Rev. Applied*, vol. 10, p. 31001, 9 2018.

[120] C.-F. Pai, Y. Ou, L. H. Vilela-Leão, D. C. Ralph, and R. A. Buhrman, "Dependence of the efficiency of spin Hall torque on the transparency of Pt/ferromagnetic layer interfaces," *Phys. Rev. B*, vol. 92, p. 64426, 8 2015.

[121] M.-H. Nguyen, M. Zhao, D. C. Ralph, and R. A. Buhrman, "Enhanced spin Hall torque efficiency in Pt100xAlx and Pt100xHfx alloys arising from the intrinsic spin Hall effect," *Applied Physics Letters*, vol. 108, p. 242407, 6 2016.

[122] J. W. Lee, Y.-W. Oh, S.-Y. Park, A. I. Figueroa, G. van der Laan, G. Go, K.-J. Lee, and B.-G. Park, "Enhanced spin-orbit torque by engineering Pt resistivity in $\mathrm{Pt}/\mathrm{Co}/\mathrm{Al}{\mathrm{O}}_{x}$ structures," *Phys. Rev. B*, vol. 96, p. 64405, 8 2017.

[123] C. L. Canedy, X. W. Li, and G. Xiao, "Large magnetic moment enhancement and extraordinary Hall effect in Co/Pt superlattices," *Phys. Rev. B*, vol. 62, pp. 508–519, 7 2000.

[124] T. A. Peterson, A. P. McFadden, C. J. Palmstr\om, and P. A. Crowell, "Influence of the magnetic proximity effect on spin-orbit torque efficiencies in ferromagnet/platinum bilayers," *Phys. Rev. B*, vol. 97, p. 20403, 1 2018.

[125] L. J. Zhu, D. C. Ralph, and R. A. Buhrman, "Irrelevance of magnetic proximity effect to spin-orbit torques in heavy-metal/ferromagnet bilayers," *Phys. Rev. B*, vol. 98, p. 134406, 10 2018.

[126] M. Hayashi, J. Kim, M. Yamanouchi, and H. Ohno, "Quantitative characterization of the spin-orbit torque using harmonic Hall voltage measurements," *Phys. Rev. B*, vol. 89, p. 144425, 4 2014.

[127] C. O. Avci, K. Garello, M. Gabureac, A. Ghosh, A. Fuhrer, S. F. Alvarado, and P. Gambardella, "Interplay of spin-orbit torque and thermoelectric effects in ferromagnet/normal-metal bilayers," *Phys. Rev. B*, vol. 90, p. 224427, 12 2014.

[128] L. Ma, H.-A. Zhou, L. Wang, X.-L. Fan, W.-J. Fan, D.-S. Xue, K. Xia, Z. Wang, R.-Q. Wu, G.-Y. Guo, L. Sun, X. Wang, X.-M. Cheng, and S. Zhou, "Spin Orbit Coupling Controlled Spin Pumping and Spin Hall Magnetoresistance Effects," *Advanced Electronic Materials*, p. 1600112, 8 2016.

[129] J.-C. Rojas-Sánchez, N. Reyren, P. Laczkowski, W. Savero, J.-P. Attané, C. Deranlot, M. Jamet, J.-M. George, L. Vila, and H. Jaffrès, "Spin Pumping and Inverse Spin Hall Effect in Platinum: The Essential Role of Spin-Memory Loss at Metallic Interfaces," *Phys. Rev. Lett.*, vol. 112, p. 106602, 3 2014.

[130] M.-H. Nguyen, D. C. Ralph, and R. A. Buhrman, "Spin Torque Study of the Spin Hall Conductivity and Spin Diffusion Length in Platinum Thin Films with Varying Resistivity," *Phys. Rev. Lett.*, vol. 116, p. 126601, 3 2016.

[131] P. M. Haney, H.-W. Lee, K.-J. Lee, A. Manchon, and M. D. Stiles, "Current induced torques and interfacial spin-orbit coupling: Semiclassical modeling," *Phys. Rev. B*, vol. 87, p. 174411, 5 2013.

[132] L. Zhu, D. C. Ralph, and R. A. Buhrman, "Spin-Orbit Torques in Heavy-Metal–Ferromagnet Bilayers with Varying Strengths of Interfacial Spin-Orbit Coupling," *Phys. Rev. Lett.*, vol. 122, p. 77201, 2 2019.

[133] S. Fukami, T. Anekawa, C. Zhang, and H. Ohno, "A spinorbit torque switching scheme with collinear magnetic easy axis and current configuration," *Nature Nanotechnology*, vol. 11, p. 621, 3 2016.

[134] D. S. Holmes, A. L. Ripple, and M. A. Manheimer, "Energy-Efficient Superconducting ComputingPower Budgets and Requirements," *IEEE Transactions on Applied Superconductivity*, vol. 23, no. 3, p. 1701610, 2013.

[135] J. Finley and L. Liu, "Spin-Orbit-Torque Efficiency in Compensated Ferrimagnetic Cobalt-Terbium Alloys," *Phys. Rev. Applied*, vol. 6, p. 54001, 11 2016.

[136] R. Mishra, J. Yu, X. Qiu, M. Motapothula, T. Venkatesan, and H. Yang, "Anomalous Current-Induced Spin Torques in Ferrimagnets near Compensation," *Phys. Rev. Lett.*, vol. 118, p. 167201, 4 2017.

[137] P. X. Zhang, L. Y. Liao, G. Y. Shi, R. Q. Zhang, H. Q. Wu, Y. Y. Wang, F. Pan, and C. Song, "Spin-orbit torque in a completely compensated synthetic antiferromagnet," *Phys. Rev. B*, vol. 97, p. 214403, 6 2018.

[138] Y. Sun, H. Chang, M. Kabatek, Y.-Y. Song, Z. Wang, M. Jantz, W. Schneider, M. Wu, E. Montoya, B. Kardasz, B. Heinrich, S. G. E. te Velthuis, H. Schultheiss, and A. Hoffmann, "Damping in Yttrium Iron Garnet Nanoscale

Films Capped by Platinum," *Physical Review Letters*, vol. 111, p. 106601, 9 2013.

[139] A. A. Serga, A. V. Chumak, and B. Hillebrands, "YIG magnonics," *Journal of Physics D: Applied Physics*, vol. 43, no. 26, p. 264002, 2010.

[140] D. Qu, S. Y. Huang, J. Hu, R. Wu, and C. L. Chien, "Intrinsic Spin Seebeck Effect in Au/YIG," *Physical Review Letters*, vol. 110, p. 67206, 2 2013.

[141] T. Lin, C. Tang, and J. Shi, "Induced magneto-transport properties at palladium/yttrium iron garnet interface," *Applied Physics Letters*, vol. 103, p. 132407, 9 2013.

[142] J. T. Brangham, K.-Y. Meng, A. S. Yang, J. C. Gallagher, B. D. Esser, S. P. White, S. Yu, D. W. McComb, P. C. Hammel, and F. Yang, "Thickness dependence of spin Hall angle of Au grown on ${\mathrm{Y}}_{3}\mathrm{F}{\mathrm{e}}_{5}{\mathrm{O}}_{12}$ epitaxial films," *Physical Review B*, vol. 94, p. 54418, 8 2016.

[143] H. L. Wang, C. H. Du, Y. Pu, R. Adur, P. C. Hammel, and F. Y. Yang, "Large spin pumping from epitaxial Y${}_{3}$Fe${}_{5}$O${}_{12}$ thin films to Pt and W layers," *Physical Review B*, vol. 88, p. 100406, 9 2013.

[144] B. Heinrich, C. Burrowes, E. Montoya, B. Kardasz, E. Girt, Y.-Y. Song, Y. Sun, and M. Wu, "Spin Pumping at the Magnetic Insulator (YIG)/Normal Metal (Au) Interfaces," *Physical Review Letters*, vol. 107, p. 66604, 8 2011.

[145] D. Meier, D. Reinhardt, M. van Straaten, C. Klewe, M. Althammer, M. Schreier, S. T. B. Goennenwein, A. Gupta, M. Schmid, C. H. Back, J.-M. Schmalhorst, T. Kuschel, and G. Reiss, "Longitudinal spin Seebeck effect

contribution in transverse spin Seebeck effect experiments in Pt/YIG and Pt/NFO," *Nature Communications*, vol. 6, p. 8211, 9 2015.

[146] A. Prakash, J. Brangham, F. Yang, and J. P. Heremans, "Spin Seebeck effect through antiferromagnetic NiO," *Phys. Rev. B*, vol. 94, p. 14427, 7 2016.

[147] M. V. Costache, M. Sladkov, S. M. Watts, C. H. van der Wal, and B. J. van Wees, "Electrical Detection of Spin Pumping due to the Precessing Magnetization of a Single Ferromagnet," *Physical Review Letters*, vol. 97, p. 216603, 11 2006.

[148] E. Saitoh, M. Ueda, H. Miyajima, and G. Tatara, "Conversion of spin current into charge current at room temperature: Inverse spin-Hall effect," *Applied Physics Letters*, vol. 88, p. 182509, 5 2006.

[149] E. Shikoh, K. Ando, K. Kubo, E. Saitoh, T. Shinjo, and M. Shiraishi, "Spin-Pump-Induced Spin Transport in p-Type Si at Room Temperature," *Physical Review Letters*, vol. 110, p. 127201, 3 2013.

[150] M. Farle, "Ferromagnetic resonance of ultrathin metallic layers," *Reports on Progress in Physics*, vol. 61, no. 7, pp. 755–826, 1998.

[151] X. Liu, W. Zhang, M. J. Carter, and G. Xiao, "Ferromagnetic resonance and damping properties of CoFeB thin films as free layers in MgO-based magnetic tunnel junctions," *Journal of Applied Physics*, vol. 110, p. 33910, 8 2011.

[152] O. Mosendz, V. Vlaminck, J. E. Pearson, F. Y. Fradin, G. E. W. Bauer, S. D. Bader, and A. Hoffmann, "Detection and quantification of inverse spin Hall effect from spin pumping in permalloy/normal metal bilayers," *Physical Review B*, vol. 82, p. 214403, 12 2010.

[153] M. A. W. Schoen, D. Thonig, M. L. Schneider, T. J. Silva, H. T. Nembach,

O. Eriksson, O. Karis, and J. M. Shaw, "Ultra-low magnetic damping of a metallicferromagnet," *Nature Physics*, vol. 12, p. 839, 5 2016.

[154] F. Schreiber, J. Pflaum, Z. Frait, T. Mühge, and J. Pelzl, "Gilbert damping and g-factor in FexCo1x alloy films," *Solid State Communications*, vol. 93, no. 12, pp. 965–968, 1995.

[155] C. Scheck, L. Cheng, and W. E. Bailey, "Low damping in epitaxial sputtered iron films," *Applied Physics Letters*, vol. 88, p. 252510, 6 2006.

[156] C. Scheck, L. Cheng, I. Barsukov, Z. Frait, and W. E. Bailey, "Low Relaxation Rate in Epitaxial Vanadium-Doped Ultrathin Iron Films," *Physical Review Letters*, vol. 98, p. 117601, 3 2007.

[157] L. Camosi, S. Rohart, O. Fruchart, S. Pizzini, M. Belmeguenai, Y. Roussigné, A. Stashkevich, S. M. Cherif, L. Ranno, M. de Santis, and J. Vogel, "Anisotropic Dzyaloshinskii-Moriya interaction in ultrathin epitaxial Au/Co/W(110)," *Physical Review B*, vol. 95, p. 214422, 6 2017.

[158] A. V. Davydenko, A. G. Kozlov, A. G. Kolesnikov, M. E. Stebliy, G. S. Suslin, Y. E. Vekovshinin, A. V. Sadovnikov, and S. A. Nikitov, "Dzyaloshinskii-Moriya interaction in symmetric epitaxial Co/Pd(111) superlattices with different numbers of Co/Pd bilayers," *Physical Review B*, vol. 99, p. 14433, 1 2019.

[159] M. Perini, S. Meyer, B. Dupé, S. von Malottki, A. Kubetzka, K. von Bergmann, R. Wiesendanger, and S. Heinze, "Domain walls and Dzyaloshinskii-Moriya interaction in epitaxial Co/Ir(111) and Pt/Co/Ir(111)," *Physical Review B*, vol. 97, p. 184425, 5 2018.

Vita

Kemal attended l'École d'Éducation Internationale de Laval from 2004-2009. From there he attended Marianopolis College from 2009-2011 having been awarded an entrance scholarship and graduating as a Marianopolis Scholar. Then he attended McGill University from 2011-2014 obtaining a B.S. in physics and graduating with First Class Honours. While there he worked with Prof. Walter Reisner having earned an NSERC fellowship for the summer of 2013, working on the confinement of DNA. In 2014 he entered the graduate physics department of the University of Texas at Austin and began working with Professor Elaine Li on the projects discussed in this dissertation. He is happily married to his beautiful wife since just before the start of his graduate career. Together they have a four month old son.

Permanent email Address: kemal.sobotkiewich@utexas.edu

This dissertation was typeset with LaTeX 2_ε[1] by the author and Mendeley was used as the reference manager

[1] LaTeX 2_ε is an extension of LaTeX. LaTeX is a collection of macros for TeX. TeX is a trademark of the American Mathematical Society. The macros used in formatting this dissertation were written by Dinesh Das, Department of Computer Sciences, The University of Texas at Austin, and extended by Bert Kay, James A. Bednar, and Ayman El-Khashab.